GEOPHYSICAL PROCESSING AND INTERPRETATION WITH GEOLOGIC CONTROLS

GEOPHYSICAL PROCESSING AND INTERPRETATION WITH GEOLOGIC CONTROLS: EXAMPLES FROM THE BATHURST MINING CAMP

By Peter Albert Tschirhart, B.Sc

A Thesis

Submitted to the School of Graduate Studies

In Partial Fulfilment of the Requirements

for the Degree

Master of Science

MASTER OF SCIENCE (2013) McMaster University

(Earth and Environmental Sciences) Hamilton, Ontario

TITLE:	Geophysical processing and interpretation with geologic controls: examples from the Bathurst Mining Camp.
AUTHOR:	Peter Albert Tschirhart, B.Sc (McMaster University)
SUPERVISOR:	Dr. Bill Morris
NUMBER OF PAGES:	xiii, 129

Abstract

With an ever-increasing consumption of natural resources new prospecting techniques are required to satisfy the demand. Geophysical methods are one tool commonly relied upon. New acquisition platforms or survey methodologies provide one way to expand the geophysical capabilities, but are expensive and slow to develop. New processing and interpretation techniques on the other hand provide a rapid means to reinterpret existing datasets with the goal of improving our geologic understanding of a project area. This thesis presents four new ways to extract additional geologic insights from a variety of geophysical datasets. All of the studies are based within the Bathurst Mining Camp, NB.

A physical rock property database for the Bathurst Mining Camp is constructed and statistically analyzed in chapter two. Descriptive statistics include mean, standard deviation; first, second and third quartiles are calculated for density and magnetic susceptibility measurements and provided in tables for reference. Bivariate plots are then used to identify trends in the density-magnetic susceptibility relationship. We relate some of our findings to processes involved in the depositional and alteration history of the various lithologies. Comprehensive rock property databases provide valuable constraints for geophysical data processing and are essential for any subsequent geophysical modeling. This is demonstrated with two examples. A joint gravity-magnetic profile model is completed across the geologically complex Nine Mile Synform. The profile reveals deep structure in the Camp down to 5 km depth. A geologically constrained geophysical inversion model of the magnetic anomaly associated with the Armstrong B mineral deposit reveals this anomaly contains a strong magnetic remanence contribution. The influence of remanence is often ignored in magnetic interpretation and modeling, but vital to achieve a geologically correct solution. In this instance comparison of the calculated remanence direction with the expected Apparent Polar Wander Path defined direction suggests an age of mineralization that is compatible with geological evidence.

A new approach to determine the optimum near surface residual magnetic signal is presented in chapter three. Additionally, a new way of locating remanently magnetized bodies is also introduced. This technique inverts frequency domain helicopter-borne electromagnetic data to yield apparent magnetic susceptibility. To locate those zones where the magnetic signal is dominated by remanence the inverted HFEM susceptibility is cross plot against the results of a traditional apparent susceptibility filter. The inverted HFEM susceptibility is independent of remanence while the apparent susceptibility assumes no remanence. Where remanence is present the TMI derived apparent susceptibility does not correlate with the HFEM. These differences are readily evident in a cross plot of the two susceptibilities. To determine a magnetic residual the inverted susceptibility is forward modeled as a series of vertical prisms

with homogeneous susceptibility equal to the inverted susceptibility. This HFEM magnetic model is then used to reference the results of traditional wavelength separation methods. By design the HFEM information is restricted the near surface whereas all traditional regional / residual separation methods operate under wavelength assumptions. A case study using this methodology is presented on the western side of the Tetagouche Antiform.

The use of a spatially variable density correction applied to ground gravity and gravity gradiometry in the BMC is examined in the fourth chapter. The influence of topography on gravity and gravity gradiometry measurements is profound and must be removed prior to interpretation. In geologic environments where there is a structural and/or stratigraphic control on the near surface mass distribution, using a single density value may introduce error into the reduced data. A regionally variable density correction is a means to compensate for this effect. Spectral information between the ground gravity and airborne gravity gradiometry is also compared in this chapter. Both systems are fundamentally recording the same geologic mass distribution albeit by different means. Where differences exist one system must be in error.

The final chapter demonstrates a quantitative interpretative technique for geophysical data. Often interpretation of the geophysical data in a geological context is done qualitatively using total field and derivative maps. With this approach the resulting map product may reflect the interpreter's bias. Source edge detection provides a quantitative means to map lateral physical property changes in potential and non-potential field data, but the field data must be transformed prior to SED computation. There are numerous transformation algorithms, all of which operate slightly differently. We demonstrate that by combining the output of several different SED computations through data stacking, the interpretable product of SED is improved. In two examples, a synthetic example and real world example from the Bathurst Mining Camp, a number of transformation algorithms are applied to gridded geophysical datasets and the resulting SED solutions combined. Edge stacking combines the benefits and nuances of each SED algorithm; coincident, or overlapping solutions are considered more indicative of a true edge, while isolated points are taken as being indicative of random noise or false solutions.

Co-Authorship Statement

This thesis contains four independent manuscripts which address separate topics linked by study area location: the Bathurst Mining Camp. All content within is principally my own. Bill Morris provided guidance and critical reviews to all chapters.

Chapter Two: Bivariate Analysis of Rocks from the Bathurst Mining Camp: Constraints to Geophysical Modelling

Intent to submit to: Journal of Exploration and Mining Geology

Physical property measurements for approximately three quarters of the samples were taken by Victoria Tschirhart and myself. Hernan Ugalde supplied the additional physical property information acquired during previous TGI work. All statistical analysis and geophysical modelling was preformed by myself. Neil Rogers of the Geologic Survey of Canada provided insight on the geologic structure of the Nine Mile Synform. Bill Morris is responsible for Figure 2-11 and edits to the original manuscript.

Chapter Three: A new regional-residual separation for magnetic datasets using susceptibility from frequency domain electromagnetic data

Accepted to Geophysics after major revision. Revisions have been made and resubmitted on May, 8th, 2013.

Electromagnetic susceptibility inversion code and tutorials were delivered by Greg Hodges of Fugro Airborne Surveys. Pitney Bowes supplied a preliminary release of Modelvision 12 to allow forward modeling. Data was provided by NRCan through the Data Access Portal (DAP). All susceptibility inversions and forward modelling was done by myself. Bill Morris and Greg Hodges provided edits to the manuscript. Jeffry McQueen, Marc Valleau, and anonymous reviewer provided critical reviews on the original Geophysics manuscript.

Chapter Four: Applying laterally varying density corrections for ground gravity and airborne gradiometry data and comparison of frequency content. A case study from the Bathurst Mining Camp

Intent to submit to: Geophysical Prospecting

The majority of the raw ground gravity data was accessed through the NRCan DAP server. Additional raw data was supplied by Hernan Ugalde and collected by Victoria Tschirhart, Beth Hooper and myself in the summer of 2012. All processing of ground gravity data was done by myself. Airborne gravity gradiometry data was supplied by Bell Geospace and the New Brunswick Department of Natural Resources. The variable density grids for AGG terrain correction were created by myself. AGG data reduction was preformed by Catherine Cox and Dean Selman of Bell Geospace. Bill Morris and John Mims of Bell Geopsapce provided reviews and edits to the original manuscript.

Chapter Five: Improved edge detection mapping through stacking and integration: A case study in the Bathurst Mining Camp

Intent to submit to: Geophysical Prospecting

Data for this chapter was accessed through NRCan's DAP server. The synthetic model was created by myself. All edge computations and summations were performed by myself. Bill Morris provided is responsible for figure 5-6. He also provided guidance to the project and reviews to the original manuscript.

Acknowledgements

This document could not have been possible with out help from a number of people.

First and foremost I would like to thank my supervisor, Bill Morris, for support and guidance throughout. Whether it was helping to understand a concept, bounce ideas off, or any non-geophysics related discussion, I greatly appreciate your time and input.

I would also like to thank my fellow MAGGICian Vicki Tschirhart for field and office help. I also appreciate help and discussion from past MAGGICians Madeline Lee, Saralise Underhay, Hernan Ugalde and Bill Spicer.

Input from Greg Hodges of FAS for the HFEM susceptibility work was greatly appreciated. Without his help and guidance this chapter would not have been possible.

Neil Rogers, Jan Peters, and Cess van Staal of the GSC are thanked for their help in providing explanations and insights into the BMC geology.

I am indebt to Diane Jobin and Carey Gagnon of the Geodetic Survey of Canada for preparing and providing Lacoste and Romberg ground gravity meters for gravity surveying in the summer of 2012. Post survey quality control is also greatly appreciated from Diane.

Jim Walker and Reg Wilson of the New Brunswick Department of Natural Resources are thanked for their part in providing access to the Madran core shack, map deliverables, and logistical support during field work around Bathurst New Brunswick.

Discussion and processing of AGG data is greatly appreciated from Catherine Cox, Dean Selman, and John Mims of Bell Geospace. Catherine is also thanked for her review of an extended abstract submitted to SEG Las Vegas 2012 and John for his review of the original variable density manuscript.

The NRCan – TGI4 program provided funding for this project. Without this grant fieldwork for this project would not have been possible.

Last but certainly not least I would like to thank Beth Hooper for not only her help in the field but also support throughout this project.

Table of Contents

List of Figures

Chapter Two

Chapter Three

Chapter 4

Chapter Five

List of Tables

Chapter Two

Chapter Four

Chapter Five

Chapter One – Introduction

Geophysical surveys including gravity, magnetic, and electromagnetics are quintessential components of any geological interpretation exercise. Such survey systems provide continuous spatial coverage by mapping lateral variations in a sensor specific physical property. The acquisition of any new geophysical data set generally leads to improved geologic knowledge of the project area and can often spur increases in local exploration during regional surveys, or identify potential drill targets at a deposit scale. Once the survey has been completed the information acquired is commonly stored in a digital format that is permanently accessible and may be revisited at any time. The development of new processing techniques and interpretation tools can use this existing data and manipulate it such that new geologic insights may be gained in a cost effective manner. This document presents a number of new data processing protocols which result in improved geologic interpretations.

The Bathurst Mining Camp

The Bathurst Mining Camp (BMC) encompasses a semi-circular area of approximately 70 km in diameter in the Miramichi Highlands of northern New Brunswick. Part of the larger Brunswick subduction complex (BSC), the BMC records the Late Ordovician – Silurian development, closure, and subduction of the Tetagouche-Exploits back-arc basin. The BMC is composed of several distinct tectonic blocks and slivers characterized by unique volcanic stratigraphies deposited in separate ensialic to ensimatic sub-basins. These blocks developed diachronously along the Laurentia coast during the Early to Middle Ordovician in response to rifting of the Popelogan arc. Subsequent closure of the Tetagouche-Exploits back-arc basin and incorporation in the BSC in the Late Ordovician to Early Silurian resulted in juxtaposition and imbrication of the tectonic blocks into a series of large nappes. Deformation was polyphase, complex and long lived creating the complex structures and tectono-stratigraphic relationships present in the BMC.

The BMC is host to 46 volcanogenic massive sulphide (VMS) deposits, including the supergiant 229 Mt Brunswick No. 12 Mine, and over 141 massive sulphide occurrences. In 2001 the BMC produced 30% of Canada's Zn, 53% of Pb, and 17% of Ag. Current production rates are falling due to decreasing grade, deeper targets, higher risk and increasing production costs. Standard geological mapping across the BMC is limited by the less than 1% outcrop and as such, geophysical exploration techniques have played an important role in the discovery of all the major deposits. Many of the original deposits were found by electromagnetic surveys which located mineralization by the resistivity contrast between the conductive sulphides and the resistive host rock. However, direct detection by EM is limited to depths of a few hundred meters. Finding new reserves will require new procedures which are capable of outlining vectors towards blind deposits located below the near surface threshold; a new exploration paradigm is needed. The primary goal of this thesis is to develop new knowledge and techniques that will better model and detect exploration targets. Four case studies have been presented regarding such goals in this work:

1) Construction and analysis of a physical rock property database from rock samples collected throughout the BMC. The usefulness of these constraints is demonstrated with a joint gravity-magnetic profile model across the Nine Mile Synform and constraining the magnetic remanence vector of the Armstrong B deposit.
2) Development of a new technique for regional residual separation for magnetic data and detection of remanently magnetized bodies.
3) Implementation of a spatially variable density correction to both gravity and gravity gradiometry data to reduce the influence of terrain.
4) Development of a stacking procedure to improve standard source edge detection results by combining the solutions of multiple data transforms.

Chapter 2 of this thesis integrates new density and magnetic susceptibility information into a comprehensive physical rock property database for the BMC. A variety of descriptive statistics are applied to the data which are available for future reference. Bivariate plots are also used to visualize trends in the density-MS relationship for a variety of lithologies. A probabilistic bivariate representation (PBR) of the relationship between density and magnetic property variations is presented to help improve the effectiveness of gravity and magnetic exploration. Rock property information is a critical component of any geophysical modeling exercise and its usefulness is demonstrated with two constrained models. A joint gravity - magnetic profile model is created across the poorly understood Nine Mile Synform using the petrophysical constraints alongside surficial structural measurements and stratigraphic contacts. The second model uses the petrophysical information alongside drill-hole intercepts to remotely determine the remanence vector of the Armstrong B deposit.

Chapter 3 of this thesis examines the use of forward modeling a local magnetic field computed from magnetic susceptibility information inverted from frequency domain electromagnetic data. The resulting field solution is then examined for its use in constraining the possible depths of magnetic source bodies with application for regional residual separation methods. The inverted susceptibility information is also shown to provide a means of mapping the spatial extent of strata whose magnetic signature is primarily controlled by remanent magnetization. Magnetic susceptibility is inverted for from multi-frequency HFEM data for the entire Bathurst mining Camp, but only where conductivity is low are reasonable results achieved. A small subsection of the Tetagouche Antiform is chosen as a test site where the geology is well understood and the effects of conductivity limited. Both the regional – residual anomaly separation and the remanence detection methods are novel in their approach being independent of wavelength assumptions, magnetic latitude, and fundamentally restricted to the near surface.

In Chapter 4 of this thesis the use of a spatially variable density correction, applied to both ground gravity and airborne gravity gradiometry data, is considered to better correct terrain effects and enhance contact information. The concept of applying variable density corrections to ground gravity data has been around for over half a century yet it there is little use of it within the literature. In areas where structure or local lithology controls the immediate near surface density distribution, average regional densities will introduce errors into the final solution. This is especially important for airborne gravity gradiometry data where the largest return signal is from the near surface. The resultant wavelength characteristics of both outputs are then compared from semblance.

The fifth chapter of the thesis presents a simple routine for enhancing the output of edge solutions solved for with source edge detection (SED). Data transformation algorithms, which modify geophysical gradients associated with physical property contact information into peaks, is a necessary step required for the SED operator. There are however numerous data transformation methods which all operate slightly different and produce somewhat different results. Typically an interpreter would qualitatively compare several output images. The method presented in this chapter quantitatively simplifies the interpretation to a single output that can help enhance true contact information and reduce random noise. An example of this routine is used to automate mapping of the Nine-Mile Synform using a multi-parameter approach.

Geophysical Methods

Magnetics, electromagnetic, and gravity surveying are all non-invasive geophysical survey methods that have been used for over half a century to define prospective VMS targets within the BMC. Initial ground EM exploration in the 1950s followed up targets defined by airborne magnetic anomalies resulting in the discovery of many notable deposits including the Brunswick No. 6, Brunswick No. 12, and Key Anacon deposits. The discovery of the Heath Steele ore bodies in 1954 by follow-up drilling airborne electromagnetic (AEM) anomalies represented the first successful use of AEM surveying in the world (McCutcheon et al., 2003). Ground gravity has been routinely used to screen electromagnetic anomalies, another first, and is attributed to the five discoveries including the Portage Brook and Stratmat Central North sulphide occurrences (McCutcheon et al., 2003). More recently, airborne gravity gradiometry surveying has been used within the Camp to locate potential targets. The FALCON airborne gravity gradiometry system developed by BHP Minerals had its maiden survey flown over the Heath Steele and Stratmat Mines in 1999 (Dransfield et al., 2001).

Airborne EM and magnetics have also had a key role in defining the regional geologic expression in the BMC. With outcrop at less than 1% total area, a regional high resolution multi-parameter helicopter-borne magnetic, electromagnetic, radiometric survey flown as part of the Geologic Survey of Canada's EXploration TECHnology II (EXTECH-II) is in part responsible for the current map expression of the regional geology. Gravity and gravity gradiometry has also shown to be complementary in defining some of the regional structures concurrent with the magnetic and electromagnetic expression. In all cases the utility of any geophysical method for exploration is dependent on the presence of a physical property contrast between adjacent units. A brief introduction to the different methods used within this thesis is presented below.

Magnetic method

The magnetic method is the most common geophysical method used for exploration as well as the oldest. For geophysical investigations, the magnetic flux density or magnetic induction (M) is measured in units of Tesla, or more commonly nanotesla (nT), which for low-amplitude magnetic field, is proportional to the magnetizing field strength (H) and magnetic susceptibility (χ) (Blakely, 1995). This relationship can be expressed in terms of equation 1. Measured on Earth's surface the magnetic field is composed primarily of three main sources. The primary source, accounting for the majority of the field is caused by electrical currents in earth's liquid iron outer core. Secondary influences come from the upper atmosphere in the ionosphere and are caused by solar-charged particles entering the ionosphere. Crustal sources, which are of interest to exploration geophysicists, are tertiary sources. Geologically crustal sources represent the cumulative effect of all rock from the surface down to the Currie temperature (~580 deg C) at which point demagnetization occurs.

$$M = \chi H \qquad \text{Eq. 1}$$

Magnetic susceptibility is the physical property that controls how susceptible a particular material is to becoming magnetized. Geologically it represents the presence of iron rich magnetic minerals, primarily magnetite but also ilmenite, pyrrhotite, hematite and pyrite (Reynolds, 1997). Different lithologies have different susceptibilities originating from their specific mineralogical compositions. A contrast of magnetic susceptibility is required between adjacent rock units to produce laterally varying changes in the magnetic field. Most geologic sources are assumed to be produced by a purely inducing field (M_i), which is equivalent to earth's current field strength and direction. Remanent magnetization (M_r) is magnetization retained in a rock in the absence of an external field. Remanence may have been acquired during formation or metamorphism, but often has a different direction and magnitude than the current inducing field. It is therefore customary to consider the total magnetization (M) of a rock as a vector sum of its induced and remanent magnetization (Eq. 2) (Blakely, 1995).

$$M = \chi H + M_r \qquad \text{Eq. 2}$$

As the largest field measured will almost always originate from the core and is of no interest to geologic investigations it must be removed from the data prior to interpretation. Atmospheric effects from solar wind interactions in the magnetosphere too must be removed leaving behind only those generated by crustal sources. Processing raw magnetic data removes these effects through a series of correction including aircraft compensation (only for airborne surveys), heading, base station, lag, and International Geomagnetic Reference Field (IGRF) correction. Aircraft compensation compensates for the magnetic field induced by the moving airborne platform; this is typically done during acquisition in real time. Base station corrections use a secondary magnetometer setup near the survey to remove time-varying fields including those produced by external influence. The heading correction accounts for symmetric biases in the magnetic field produced by differences in travel direction during acquisition. Finally, the IGRF, which is a mathematical model of earth's normal magnetic field updated every five years to account for slow changes, is removed from every point in the survey leaving behind geologic influence. Once the external fields have been removed that data is leveled using tie-line information to adjust differences in the survey where intersecting survey lines occur. Often, corrugation is still present in the field after leveling and microleveling is used to remove this.

Gravity Method

Initially used for petroleum exploration, gravity surveying has become a very popular tool for mineral exploration, regularly used as a secondary or follow-up survey method. The gravity method measures the Earth's gravitation field which is controlled by variations in the subsurface mass distribution, or more simply put, density. It is similar to magnetics in that the signal at any observation point represents the sum of all sources below the observation point. When one attempts to model these observations the signal can be represented by non-unique solutions. The gravitational field is governed by Newton's Law of gravitation stating the mutual attractive forces between two point masses are proportional to the inverse distance between them (Eq. 3). Though this is true for any direction, for ground gravity surveys only the vertical acceleration of the gravitation field is measured (g) which by inserting Newton's second law of motion, (Eq. 4) is proportional to the mass of the earth (m_1), universal gravitational constant (G), and inversely proportional to distance from the center of earth's mass (r) squared (Eq. 5). Truly a vector quantity, this value is typically treated as scalar because non-vertical accelerations are never measured or considered for exploration. Gravitational data is often described in term of miligals (mgal) where 1 mGal = 0.001 cm/s^2.

$$F = \frac{Gm_1m_2}{r^2} \qquad \text{Eq. 3}$$

$$F = ma \qquad \text{Eq. 4}$$

$$g = \frac{Gm_1}{r^2} \qquad \text{Eq. 5}$$

Raw gravity data (g_{obs}) must first be corrected prior to interpretation. Instrument drift, Earth tides, latitude and elevation changes as well as local topographic effects all influence raw readings and must be removed prior to interpretation. Drift and tides are removed by repeat and base station reading during the course of the survey day. Latitude variations associated with the non-spherical shape of the Earth are corrected by using the International Gravity Formula (g_n). The free-air correction (FA_{corr}) accounts for gravity changes due to elevation, being positive above sea level and negative below. Highly accurate elevation data is needed to accurately compute the FA_{corr} that changes by 0.3086 mGal/m. Consequently in modern surveys differential GPS is typically acquired alongside field measurements. Older surveys relied on local surveying linked to some local bench mark elevation point. Often topographic errors were typically the largest unknown (Nabighian et al., 2005). The Bouguer correction (g_b) is the final routine correction to be applied which accounts for the mass of rock between the station elevation and sea level. Any density value may be applied to the slab, but most commonly 2.67 g/cm^3 is used, a value believed to represent the average of crystalline continental rock (Hinze, 2003). The gravity reduction formulation is defined in Eq. 5 where g_{geol} is residual gravity representing purely geologic signal. An additional correction, the terrain correction (g_t), is also sometimes applied, and should always be used in areas of rugged relief. This correction accounts for the local influence of topography on the station. The value for terrain correction can be solved for using digital elevation models by calculating the effect of excess or absent mass on a point location within the survey.

$$g_{geol} = g_{obs} - (g_n + FA_{corr} + g_b + g_t) \qquad \text{Eq. 6}$$

Gravity Gradiometry Method

Though gravity gradiometry is becoming increasingly popular with the advent of airborne systems, the use of gradiometry for exploration actually predates that of vertical gravity (Nabighian et al., 2005). The torsion balance gravity gradiometer was first used in the 1920's for oil and gas exploration, but as the accuracy of spring gravimetry improved, the torsion balance was phased out. More recently, several airborne gravity gradiometry (AGG) systems have become available based on technology developed by Bell Aerospace (now Lockheed Martin) for the US Navy (Murphy, 2004). Similar to the gravimetry method, gradiometry maps subsurface mass density changes reflecting density differences between lithologies, but instead of recording the amplitude of gravitation acceleration, it is recording the rate of change of gravitational acceleration in a number of directions (tensors).

The gravity gradient tensor has nine components corresponding to the three spatial directions in which the vertical gravity acceleration field can vary. However, three of the components are redundant and therefore full tensor systems only measure six components. An AGG system may either record all six tensor components (e.g. Bell 3D-FTG) or partial tensor components (e.g. Fugro FALCON). A full tensor survey will record the six tensor components listed below. Individual components can each be related to geologic attributes such as edges of geologic bodies, depth, or density information (Murphy and Brewster, 2007). Gradiometry data is expressed in terms of Eotovs where 1 Eo = 1 ns^{-2}.

$$\begin{bmatrix} g_{xx}\ g_{xy}\ g_{xz} \\ g_{yy}\ g_{yz} \\ g_{zz} \end{bmatrix}$$

The theoretical correction to gravity gradiometry data is simpler than gravity data, nevertheless it is practically much more difficult. Gradiometry systems do not require the latitude, free-air or Bouguer corrections required of gravimetry data, however critical to the AGG system is the effects of aircraft acceleration and terrain. Long wavelength drift may also be present and require compensation. Full tensor noise reduction is also typically performed to remove uncorrelated signal between the tensor components using Fourier domain or equivalent source techniques (Barnes and Lumley, 2011). Leveling and microleveling may also be applied but an ‘optimal’ or ‘standard’ for AGG data correction is not yet established and processing varies between acquisition platforms.

Electromagnetic method

The electromagnetic method (EM) is the second most popular geophysical exploration method in the mining industry surpassed only by magnetics. It is also possibly the most diverse method in terms of instrument arrays and configurations and therefore will restrict the discussion to only active airborne electromagnetic methods (AEM). An active AEM system works by induction and may be either frequency domain (FDEM) or time domain (TDEM). Frequency domain AEM systems measure the ground response from a set of specific transmitting frequencies, while time domain systems take measurements as a function of time.

The basic principle for both FDEM and TDEM system is the same. A transmitter coil generates the primary electromagnetic field that propagates above and below ground. When this field interacts with conductive bodies below surface it induces eddy currents which in turn generate their own secondary electromagnetic field. A receiver coil records the signal induced in-phase with the primary field (the in-phase component) and that at 90 degrees to it (the quadrature component). It is typically inappropriate to interpret the in-phase to quadrature ratio since flight height variation can have a significant influence on the response and therefore AEM data is converted into apparent conductivity maps. There are a number of ways to convert the data but two of the most popular are the homogeneous half space model and pseudo layer/ layered earth model (Fraser 1978).

AEM data reflect the various conductivity responses in the subsurface. In FDEM surveys, higher frequencies represent shallower sources, while lower frequencies deeper. The limit of penetration depth for FDEM surveys is function of the ground conductivity and frequency of transmitter coil but is usually restricted less than two hundred meters from surface. TDEM surveys are able to resolve deeper structures where their maximum penetration is a function of the on-time during transmission. Some TDEM surveys claim to be capable of resolve features over 1 km from surface.

References

Barnes, G., and Lumley, J., 2011. Processing gravity gradient data. Geophysics, **76**, I33-I47.

Blakely, R. J., 1996. Potential theory in gravity and magnetic applications. Cambridge University Press.

Dransfield, M., Christensen, A., Diorio, P., Rose, M., and Stone, P., 2001. FALCON test results from the Bathurst Mining camp. ASEG Extended Abstracts 2001, 1-4.

Fraser, D. C., 1978. Resistivity mapping with an airborne multicoil electromagnetic system. Geophysics, **43**, 144-172.

McCrutcheon, S.R., Luff, W.M., and Boyle, R.W., 2003. The Bathurst Mining Camp, New Brunswick, Canada: History of discovery and evolution of the Geologic Models. *In* Massive Sulfide Deposits of the Bathurst Mining Camp, New Brunswick, and Northern Maine. *Edited by* W.D., Goodfellow, S.R., McCutcheon, and J.M., Peter. Economic Geology Monograph 11, 17-35.

Murphy, C. A., 2004. The Air-FTG airborne gravity gradiometer system. ASEG-PESA, Sydney-2004, 7-14.

Murphy, C. A., and Brewster, J., 2007. Target delineation using full tensor gravity gradiometry data. ASEG Extended Abstracts 2007, 1-3.

Nabighian, M. N., Ander, M. E., Grauch, V. J. S., Hansen, R. O., LaFehr, T. R., Li, Y., Pearson, W. C., Peirce, J. W., Phillips, J. D., and Ruder, M. E., 2005. Historical development of the gravity method in exploration. Geophysics, **70**, 63ND-89ND.

Reynolds, J. M., 1997. An introduction to applied and environmental geophysics. West Sussex, England. John Wiley & Sons Ltd. 796 pp.

Chapter Two: Bivariate Analysis of Petrophysical Properties of Rocks from the Bathurst Mining Camp: Constraints to Geophysical Modelling

Peter Tschirhart and Bill Morris

MAGGIC, SGES, McMaster University, Hamilton ON L8S 4K1.

Abstract

Understanding the physical rock properties of different lithologies within a geologic district can act as the catalyst to allow for the geologic and geophysical interpretations to cohere. A comprehensive physical property database is therefore beneficial to any exploration program. This paper expands upon an existing physical rock property database for the Bathurst Mining Camp by incorporating new density and magnetic susceptibility measurements. Mean, standard deviation, median, 1st and 3rd quartiles are calculated for a variety of lithologies in the Camp and supplied in tables for reference. Density – magnetic susceptibility bivariate plots are used to illustrate and quantify patterns in the density-magnetic susceptibility relationship that are indicative of mineralogical changes occasioned by depositional style and alteration history variations. Geophysical modeling exercises can use these data as inputs in the forward and inversion modeling calculations by introducing real-world constraints. We demonstrate this with two examples: 1) a joint gravity-magnetic profile model across the geologically complex Nine Mile Synform (NMS) and 2) remote detection of the remanence contribution for the magnetic anomaly associated with the Armstrong B deposit. The NMS model reveals the deep structure of the BMC to be highly deformed. The geometry of most tectonic and lithological contacts is near vertical. Deformation is often distinct within individual nappes and reflects intense deformation prior to amalgamation within the Brunswick Subduction Complex. Most tectonic blocks continue below the 5 km threshold of the profile and the total depth remains unknown. The magnetic anomaly associated with the Armstrong B deposit contains a remanence vector oriented roughly south and inclined just below the horizon. The intensity of remanence is comparable to the Present Earth's Inducing Field. A comparison between the calculated remanence vector and that estimated for the Laurentia continent reveals the remanence must have been acquired concurrently with the estimated peak of metamorphism in the Salinic orogeny.

Introduction

Physical rock properties, which reflect the chemical and mineralogical composition of a rock, influence the response of a rock unit when surveyed by different geophysical and geochemical measuring systems. Common physical rock properties include, but are not limited to density, conductivity/resistivity, magnetic susceptibility (MS), P and S-wave velocities. Respectively, these properties would correspond to gravity surveys, electromagnetic and induced polarization surveys, magnetic surveys and seismic surveys. Geological interpretations of geophysical data require an understanding of physical rock properties in order to better constrain possible model geometries and to avoid erroneous model solutions (e.g. areas where remanent magnetization exists or strong electrical anisotropy is present). Even processing of some geophysical datasets can be improved by a detailed knowledge of rock property variations across an area, for example, density is used in the reduction of all gravity data. It is for these reasons that many mining and exploration companies, as well as government geological agencies have begun acquiring physical property information to improve exploration programs. Regional scale physical property information is also available in textbooks and published literature. However these values may not be accurate for the study area under investigation as deposition style, alteration, and metamorphic histories; all of which affect a rock's chemical and mineralogical composition, may differ. Having more precise local information, significantly improves the interpreter's ability to combine geologic and geophysical information into a single integrated "Common Earth" exploration model.

In this paper we expand upon the existing rock property database developed by Mwenifumbo et al., (2003) and Thomas et al., (2000) for the Bathurst Mining Camp (BMC) by incorporating new density and MS information. Previous work by Mwenifumbo et al., (2003) reported multi-parameter downhole logs at the Stratmat, Halfmile Lake and Restigouche deposits, but only in a local context, emphasising the massive sulphide component and neglecting any correlation of the physical properties between similar host and ore rocks across deposits. The first part of this paper we present statistical analyses of physical property variations of the various lithologies recorded in the sample population. Mean, standard deviation, median, 1st and 3rd quartiles are provided in tables for future reference. Density - MS bivariate plots are used to illustrate and quantify patterns in the density-MS relationship that are indicative of mineralogical changes occasioned by depositional style and alteration history variations. From these plots and descriptive statistics, a bivariate probabilistic representation (BPR) of the density and magnetic susceptibility relationship is created. Such a plot creates statistically significant density – MS signatures for the different lithological settings that form the basis for a geologically realistic starting point for geophysical modelling exercise.

The second section of this paper illustrates the usefulness of these new physical property measurements by producing two geophysically constrained models. A 2-dimensional profile model is constructed across the geologically complex Nine Mile Synform (NMS) using joint gravity and magnetic data alongside geologic contact and structural information. The second model uses known magnetic susceptibility information and geologic structure controls for a constrained inversion to remotely solve for the magnetic remanence contribution to the total magnetic anomaly signal associated with the Armstrong B deposit.

Study Area

The Bathurst Mining Camp, (Figure 2-1) has been an important mining camp in Eastern Canada for over 50 years, hosting 46 volcanogenic massive sulphide (VMS) deposits including the supergiant 121 Mt Brunswick 12 deposit (McCutcheon et al., 2003). Geologically the BMC is interpreted to represent a preserved section of the Brunswick subduction complex (BSC) which developed in response to the closure of the Tetagouche-Exploits Basin, analogous to the modern day Japan Sea (van Staal et al., 2003). Felsic to mafic back arc volcanogenic rocks with coeval sedimentary rocks of the California Lake, Tetagouche, Fournier and Sheephouse Brook tectonic blocks diachronously developed in separate sub-basins, sharing a common tectonic environment along the margin of the Laurentia continent (Rogers et al., 2003a). Subsequently these adjacent terranes were incorporated into the southeast facing Brunswick subduction complex during the Salinic orogeny. From the Ordovician through to the Early Silurian on-going subduction resulted in a series of tectonic blocks that were structurally juxtaposed and imbricated into a series of nappes. D_1 and D_2 thrusting created older over younger relationships both locally, within individual nappes, and regionally across tectonic blocks. The Arenig to Caradoc age Fournier Block was proximally closest to the BSC and as such was the first terrane incorporated. Through the Late Ordovician – Early Silurian, the California Lake Block underthrust the Fournier Block, which was in turn underthrust by the coeval Tetagouche Block. The Sheephouse Brook Block was last to be incorporated and structurally lies at the deepest level. Regional high-pressure, low-temperature penetrative deformation followed closure of the complex. D_3 and D_4 structures overprint D_1 and D_2 during unroofing and exhumation of the BMC. A thorough discussion on the geology and tectonostratigraphy of each tectonic block is given in van Staal et al., (2003) and van Staal et al., (2008).

Rock Property Information

Physical Property Sample Populations

This work incorporates results from two studies of density and magnetic susceptibility measurements. The two studies were acquired at different times and in different contexts. The first study, P_1, is composed of 311 density and magnetic susceptibility values measured on rock samples acquired in situ on outcrops during fieldwork throughout the camp (Figure 2-1). These samples were acquired over the course of several field seasons: 1985-89, 1995, and 1996 by Cees van Staal of the Geological Survey of Canada. Density and susceptibility measurements were made in 1997 for the Exploration and Technology II (EXTECH) project. Sample lithologies were assigned by the field geologist.

The second study, P_2, reports density and magnetic susceptibility measurements acquired on drill core at the Madran Core Facility, Madran New Brunswick. Fifteen different drill cores were sampled in the fall of 2011. Density and susceptibility readings were taken on 960 samples during this study. The location of the individual drill cores is shown in Figure 2-1 where they are prefixed with BVJ- and ELN-. Complete logs are shown in Appendix A of this thesis. Lithologies were assigned to samples via geologic logs accompanying the cores.

Physical Property Measurements

For both P_1 and P_2 density values are obtained from samples by first weighing the sample in air then again submerged in water. Applying the formula (0.9975 x weight in air) / (weight in air – weight in water) yields density. Three magnetic susceptibility measurements are taken and averaged for each susceptibility value used in these two populations. This is done to minimize the effects of localized magnetic mineral content variations. Different magnetic susceptibility meters were used for the two studies. P_1 used a KT-5 instrument and P_2 a Bartington MS2-E. Both meters have a sensitivity of 10^{-5} SI. Minor differences have been noted by Lee and Morris (2012) when different meters are used on identical samples which results from different coil diameter inside the meter's measuring pad, however the differences are negligible relative to the large dynamic range of susceptibility measured. Because of the similarities in measurement methodology the populations P_1 and P_2 have been combined into a larger sample size ($P_{1,2}$) to perform descriptive statistic and bivariate analysis.

Methods

Statistical Procedures

Descriptive statistics including: mean ($\overline{x}$), standard deviation (s), 25th, 50th (median), and 75th quartiles (Q_1, Q_2, and Q_3 respectively) are applied to the combined P_1 and P_2 data base for both density and MS. Results are listed in Table 2-1 for density and Table 2-2 for MS. Various density-MS bivariate plots are generated from the combined $P_{1,2}$ dataset. These plots are subdivided into the most basic classification (herein referred to as bulk classification): Felsic-Intermediate, Mafic, Sedimentary Rock, and Iron Formations, where within more specific lithologies are plotted for comparison (Figures 2-2 – 2-5). There are some instances within these plots where a specific lithology may not strictly belong to the bulk classification but have

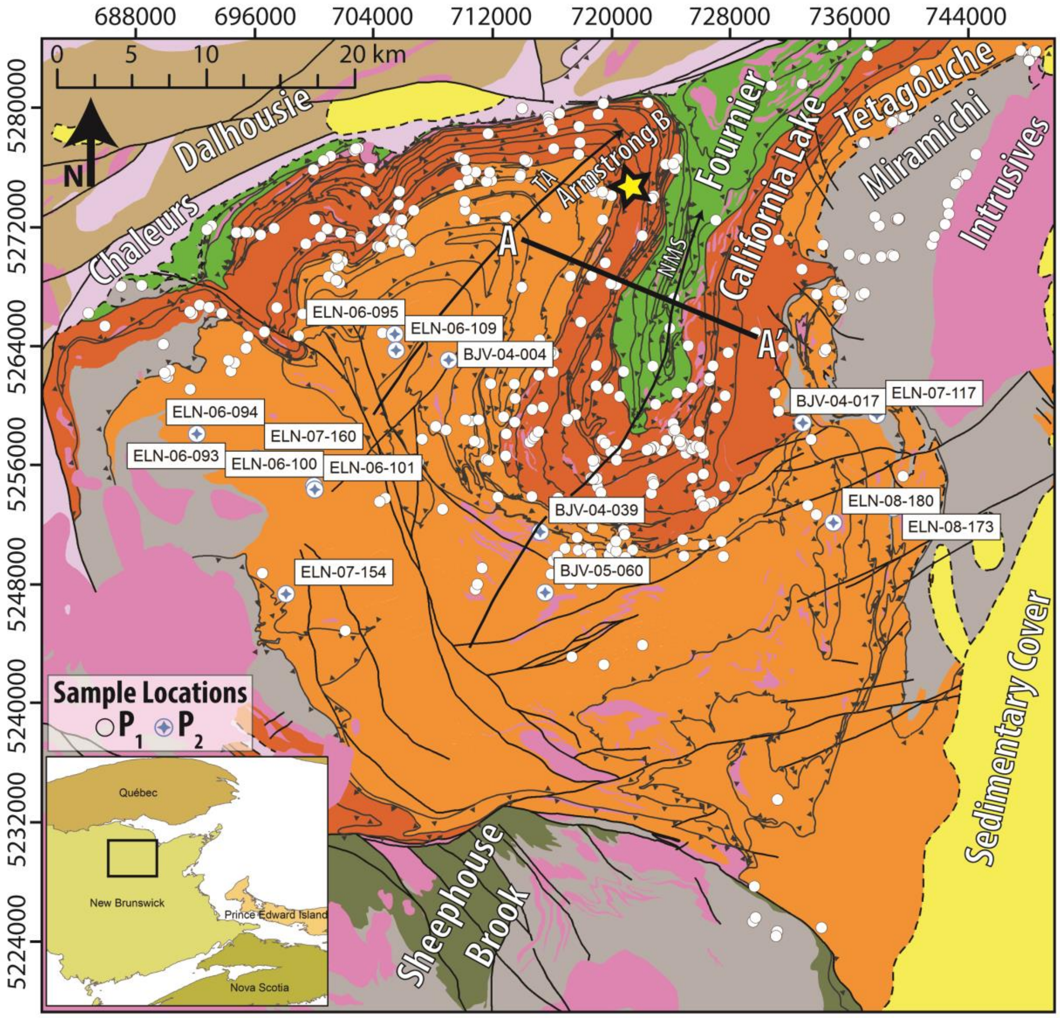

Figure 2-1: Simplified tectonic map of the Bathurst Mining Camp outlining the geologic groups, modified from Van Staal et al., 2003. Locations of rock property samples and geophysical models identified. TA = Tetagouche Antiform, NMS = Nine Mile Synform.

been included or excluded for a specific reason. Felsic and intermediate samples have been combined into a single plot because the only truly intermediate rock type, dacite has a small sample size (n=4) and has similar petrophysical characteristics to other felsic rock types. It was therefore not practical to create a purely intermediate plot. Conversely, iron formation samples are split from the sedimentary plot and given their own grouping because of their petrophysical uniqueness and importance as an exploration marker. A bivariate plot for sulphides was also generated discretizing some of the different bedding styles (Figure 2-6).

From the descriptive statistics on $P_{1,2}$ and bivariate plots a probabilistic bivariate plot (PBP) is created for all bulk classifications (Figure 2-7). Within this plot the density and susceptibility mean is represented by a dot surrounded by an ellipse encompassing the 25th to 75th quartile. In essence 50 percent of the recorded data statistically falls into the ellipse for each classification.

Geophysical Modelling

Forward geophysical models attempt to test the veracity of a hypothetical geologic model by iteratively adjusting contact boundaries to find an optimum fit between the observed and the calculated geophysical signal (Figures 2-8, 2-9). It can be thought of as building up from what is known. The operator uses input geologic information such as contact locations, strike, dip, body geometry and depth extent to build a geologic cross section representative of the suspected subsurface geometry. Density and/ or magnetic susceptibility information is assigned to the model lithologies and body geometries adjusted so the observed gravity and magnetic signal produced by the model matches the gravity and magnetic fields observed. A geologically and geophysical consistent model will produce a geophysical signal that has a close fit to the observed geophysical data while being geologically accurate.

Remanence Vector Determination

Determination of the remanence vector is a vital yet often overlooked aspect of magnetic interpretation. The magnitude of the observed magnetic anomaly at any point is the vector summation of individual contributions arising from the Earth's core, the Earth's crust and temporarily fluctuating contributions from the Sun. The crustal magnetic component comprises two elements; the induced and the remanent magnetic fields. The induced magnetic field vector is dependent on the magnetic susceptibility of the rock and the local orientation and magnitude of the present Earth's magnetic field (the core signal). The remanent vector is independent of the present Earth field. Rather, it represents the orientation of the Earth's field for some previous point in time when the remanence was fixed in the rock. The amplitude of the remanence vector is a function of the magnetic mineralogy present in the rock and the strength of the Earth's field at the time of remanence acquisition. The resulting magnetic anomaly pattern reflects the interaction between the effective magnetic vector and the geometry of the anomalous source body.

There are a number of both qualitative and quantitative methods for detecting regions of remanently magnetized terrane within a project area. Zietz and Andreasen (1966) introduced the idea of using the direction between the positive and negative poles of a magnetic anomaly to estimate the declination of the magnetic vector. However, as later shown by Schnetzler and Taylor (1984), while this provides reasonable control on the magnetic declination, it does not provide direct control on the inclination of the magnetic vector. An alternative approach proposed by a number of authors (Baranov, 1957, Bott et al., 1966, Muniruzzaman and Banks, 1989) attempted to solve the problem by comparing the aeromagnetic signal and the regional gravity signal. Other authors have compared different derivatives of the observed magnetic field, for example Roest and Pilkington (1993) compare the amplitude of the analytic signal with the horizontal gradient of the pseudo gravity signal. Most recently, Tschirhart (this thesis, Chapter 3) has introduced a method based on a comparison of the observed total magnetic field and a TMI computed using susceptibility derived from a helicopter-borne frequency domain EM survey. Where the method shows well-defined differences between the observed and calculated TMI signal is a direct indication of a remanence contribution in the observed TMI.

All magnetic inversion model routines (discrete object, discrete surface, voxel mesh (Morris et al., 2012)), irrespective of the details of the actual technique applied, describe three elements of the anomalous source body: 1) its location, 2) its geometry, and 3) its physical rock properties. Having identified that magnetic remanence contributes to the observed magnetic anomaly this constraint should be included in any subsequent attempt to model the anomalous signal. To accurately include the remanence contribution in the inversion model ideally one needs the information regarding the full orientation of the remanence vector. Unfortunately, as recognised by Paterson and Reeves (1985) this can be complicated by the source body being tectonically inclined; with total field data it is impossible to differentiate between source tilt and remanence inclination. More recent studies have attempted to overcome this problem by modeling the amplitude of the anomalous vector (Li et al., 2010, Foss et al., 2012).

We apply an inversion approach where we fix several source body parameters and invert for the resultant total magnetization. Using the geologic and petrophysical information we generate a forward model which acts as a starting point for our inversion (Figure 2-10). The location and geometry of the Armstrong B deposit is well defined by a number of drill-holes intersecting mineralization and a geologic cross section . We approximate the lensed shaped deposit as a steeply dipping (65°), northerly striking (15°) tabular body of 244 m length. These parameters, which were derived from Thomas et al., (2000), together with pierce points where drill holes intersected ore body contact were held as fixed parameters in the inversion. The average MS of the deposit and host rock can also be accurately extrapolated using our statistic results. The average susceptibility for host felsic tuffs and ore massive sulphides were set to 0.1 x 10^{-3} SI and 6 x 10^{-3} SI respectively, which are the average values for the respective rock types listed in Table 2-2. The orientation and magnitude of the present Earth's field were also fixed. Having identified the fixed variables we then looked at the floating parameters in our inversion model. The body thickness was set to be slightly wider than logged (25 m versus 12 m) but allowed to vary during the inversion. The depth extent was also allowed to vary during the inversion and set to start at 183 m; the maximum recorded downward extension from drill core intercepts. Finally, we allowed the magnetic remanence contribution to float. The output of our inversion model is a geologically constrained approximation of geometry of the Armstrong B deposit and an estimate of the orientation of the remanent magnetic vector.

Results and Discussion

Bivariate Analysis

The BMC is mainly composed of felsic volcanic rocks, principally rhyolites and volcanic tuffs being an order more voluminous than other lithologies (Rogers et al., 2003b). Because of the numerous rock-types within the felsic-intermediate classification, two plots are generated for simplicity of the different sub-species (Figures 2-2A, 2-2B). Also a third comparing different bedding styles (Figure 2-2C) is created. Most of the tuffaceous samples (Figure 2-2A) overlap within their respective ranges though ash tuff tends to preferentially be restricted to < 2.8 g/cm^3. A very similar distribution is present in the proceeding bivariate plot (Figure 2-2B) with the vast majority of samples being low density and low susceptibility clustered around 2.70 g/cm^3 and 1.0x10^{-4} SI. Since a majority of samples were measured on core above exploration targets, the prevailing interpretation is that during hydrothermal alteration, magnetic minerals within the host rock are altered to weakly magnetic minerals creating an anomalously low susceptibility in the alteration zones (Mwenifumbo et al., 2003). In part this statement must imply that density is also systematically being modified (reduced) which is evident in the log-linear trend of the data. It is likely that this relationship does not universally apply. Some massive rhyolite samples have atypically high magnetic susceptibility values which are not accompanied by high density values. The magnitude of the susceptibility implies an enrichment of magnetite or pyrrhotite with no increase in density. Similarly, many of the high density – high susceptibility samples imply an enrichment of sulphide and magnetic minerals to the host rock above sulphide zones which again contradicts Mwenifumbo et al., (2003).

Sedimentary rocks occur throughout the BMC in all major stratigraphic groups (van Staal et al., 2003). Many of the sedimentary rock types have widespread distributions both for density and susceptibility with considerable overlap amongst the different lithologies (Figure 2-

3A). Relationships which would be expected are followed such as increasing density with decreasing grain size (ex. siltstone to shale) and low susceptibility in quartzite. High susceptibility values are present for many for siltstone and shale samples especially in regions where the detrital source was nearby mafic ophiolites. Sedimentary rocks, like rhyolites, share a close relationship with the genetic model for sulphide deposits and it is therefore not surprising that some samples have high density (>2.90 g/cm^3) and susceptibility (>1x10^{-2} SI) values. In all cases, these samples were acquired from boreholes above exploration targets where local enrichments in magnetite and pyrrhotite is common. Interestingly the measurements seem to follow two susceptibility trends, S1 and S2, which can be explained to some extent by degree of metamorphism and alteration (Figures 2-3B, 2-3C). Samples with no stated metamorphism follow S1 and have steadily increasing magnetic susceptibility with increasing density. Conversely low-grade metamorphism (i.e. slate and phyllite) or sericitic/ chloritic alteration seems to suppress the magnetic content of the sample, obeying the S2 trend such that increasing density is only loosely linked to increasing susceptibility. This observation is more consistent with that by Mwenifumbo et al., (2003) stated above. The S2 trend is also subtly present in Figure 2-3B which may suggest that the degree of metamorphism was inadequately described by the logging geologist.

Iron formations (Figure 2-4) are significant within the BMC as they are spatially and temporally associated with massive sulphide deposits, representing primary sedimentary units forming coevally alongside deposits (Peters et al., 2003). For this reason their importance has been stressed as an exploration vector (Keating et al., 2003, Peters et al., 2003, Thomas, 2003, Goodfellow et al., 2003). As discussed in Goodfellow et al., (2003) iron formations occur as two types, Type 1 - Llanvirn-hematite rich and Type 2 - Arenig-magnetite rich types; the latter being associated with sulphide mineralization. The Llanvrin-type formations are associated with high concentrations of heavy elements Fe, Mn, Zn, Co, Ni and P, while the Arenig-type facies are associated with siderite, chert and epiclastic sedimentary rocks. We speculate that from their chemical constituents Type 2 iron formations should be less dense and magnetically more susceptible than Type 1. A trend corresponding to this pattern is apparent in our limited data set. Samples with lower susceptibility values correspond to Type 1 - hematite rich samples while higher values represent Type 2 - magnetite rich. It is anticipated that more samples would better define this relationship.

In the bivariate plot of mafic rocks, (Figure 2-5), all lithologies exhibit some degree of overlap. Of the lithologies present, basalt has the greatest range, both in terms of density and MS. This may in part result from it also having the greatest sample population. There is no real unique signature associated with any of the lithologies, though diabase does tend to be slightly more restricted in its density range than the others. An interesting observation is that the mafic values produce two distinct clusters, a high susceptibility M1 cluster and low susceptibility M2

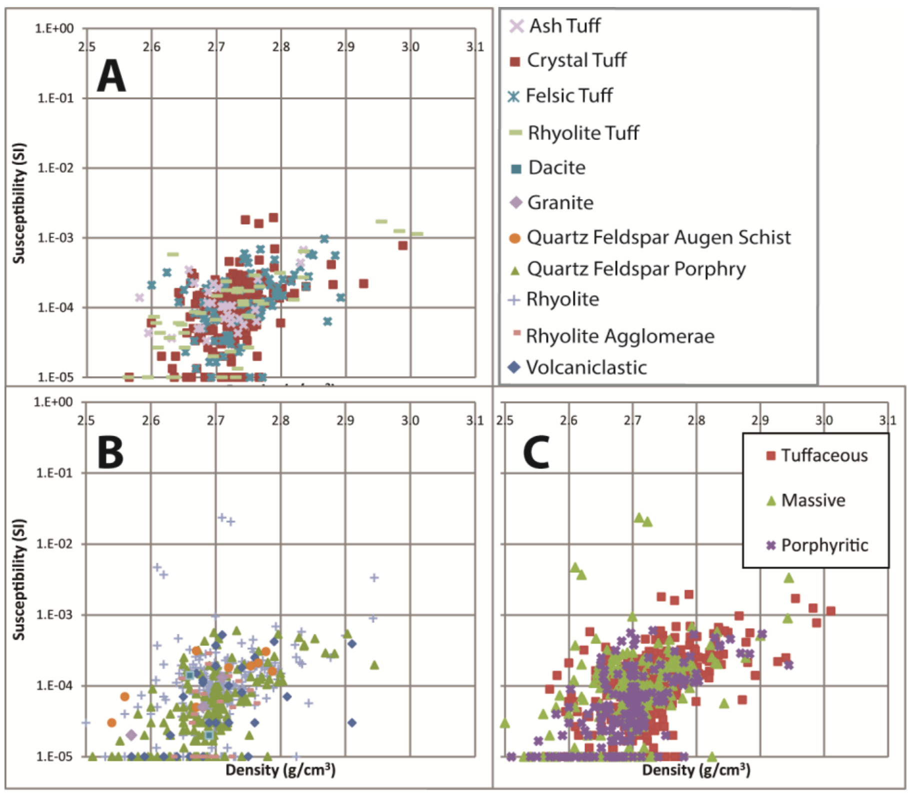

Figure 2-2: Comparison between different sub-specifies of felsic – intermediate rock types. Sub-species have been divided between tuffaceous lithologies in A and other species in B for simplicity. 4C compares bedding styles.

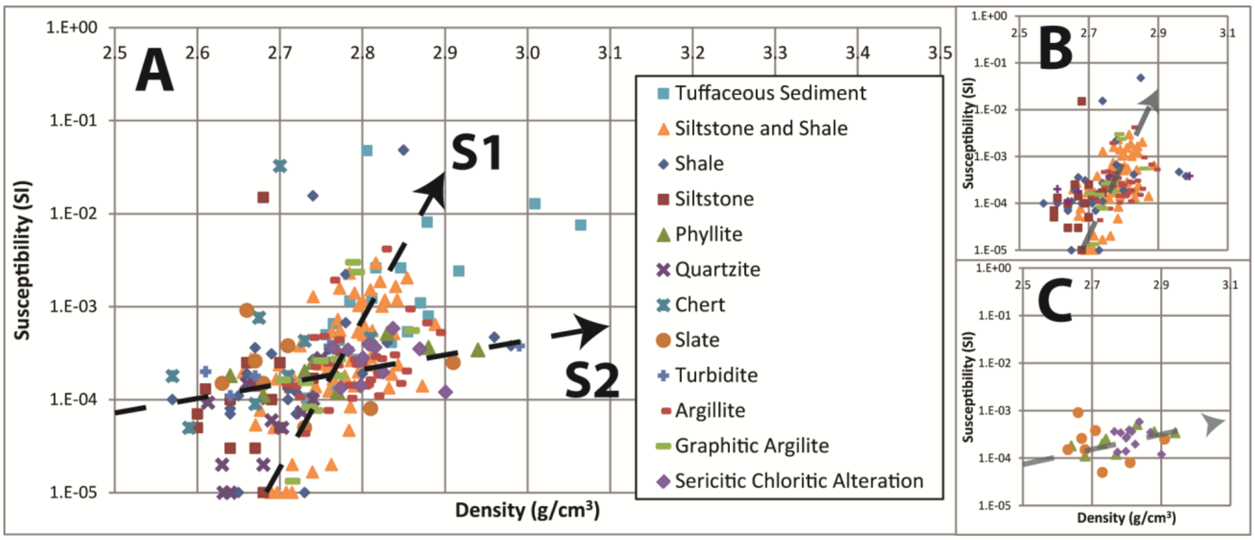

Figure 2-3: (A) Comparison of all lithologies for sedimentary rocks excluding iron formations. **(B)** Non-metamorphosed or altered sedimentary rock types. **(C)** Metamorphosed or altered lithologies.

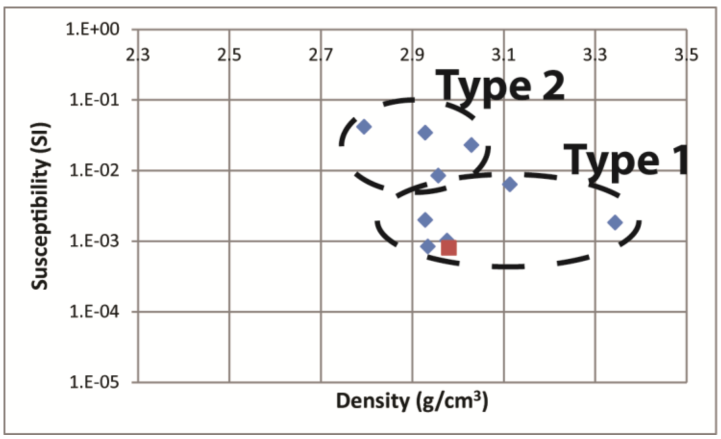

Figure 2-4: Bivariate plot of iron formation samples.

cluster. Also interesting is that this is not specific to any one lithology, all five have at least one sample contained within each cluster. As a first pass it was thought that perhaps this bimodal cluster may be related to specific stratigraphic horizons however, a map of the spatial distribution of the two clusters failed to provide any conclusive evidence since spatially and geologically similar samples fall into both clusters. Another possible explanation could be related to the rate of cooling for the intrusive gabbro, diabase and mafic dyke and flow style for basalt since susceptibility is seemingly only affected. For blueschist this could be an artefact of the pre-metamorphosed basalt. A third possible explanation could be chemical compositional differences in source magma. Calc – alkali magma series tend to precipitate more significant amounts of iron oxides, thus magnetite, than tholeiitic series, however in our samples both calc-alkalic and tholeiitic samples are contained in both populations though this may also result from improper classification.

Sulphides are unquestionably the most important lithology in the BMC and occur in four different facies styles: economically viable bedded ores, uneconomic bedded pyrite, vent complexes and sulphide stringer zones (Goodfellow, 2007), however herein sulphides are discriminated on ore styles more typical of exploration programs in the camp; massive, disseminated, and stringer (Figure 2-6). Relative to the other rock types sulphides have by far the broadest density-MS distribution. They are also typically the most dense rock type and are comparable to iron-formations and the M1 cluster of mafic rocks in terms of their MS. Most VMS deposits are hosted in sedimentary and felsic volcanic successions where the density and MS characteristic of the ore is distinct relative to the host. Density is the primary defining factor in massive ores versus disseminated or semi-massive. It is expected that massive ores would have a greater concentration of heavy minerals such as sphalerite and galena. Susceptibility values completely overlap within the plot with massive ores recording both the highest and lowest susceptibility values suggesting similar amounts of magnetite and pyrrhotite within each.

Probabilistic Bivariate Plot

Critical to geophysical modelling is the need of physical constraints to minimize the non-uniqueness problem associated with gravity and magnetics. Obviously the best way is to actually measure this information on core and samples but practically this may not be possible. In Figure 2-7 we present a probabilistic bivariate plot (PBP) of all $P_{1,2}$ samples which allows for a geophysically realistic starting point for each of the five bulk lithologies. The center dot represents the density-MS mean which is surrounded by an ellipse from the 25^{th} to 75^{th} percentile, so for a modelling exercise the operator may start somewhere near the mean and iterate away until an accurate and realistic model is created. This plot also acts as an illustration of how well a specific gravity and/ or magnetic modelling exercise will work at defining contacts

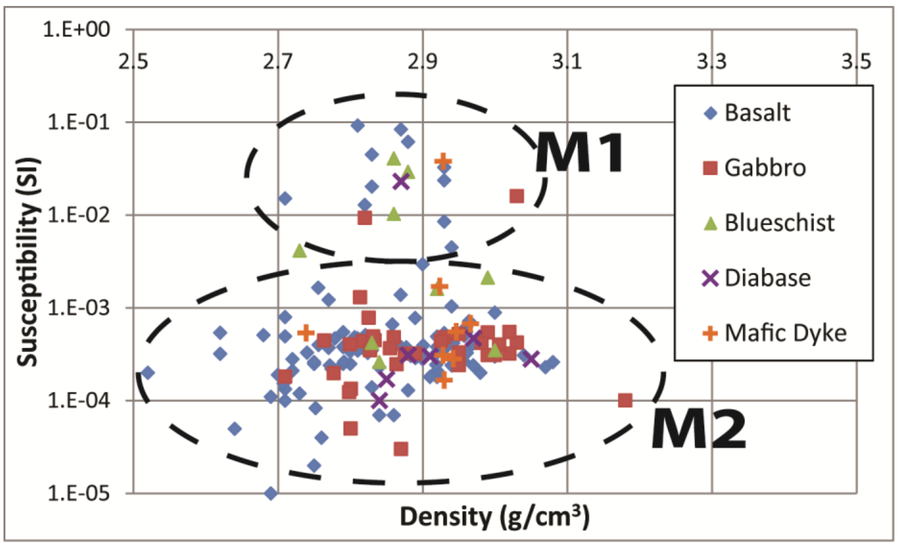

Figure 2-5: Comparison of all lithologies for the Mafic Group.

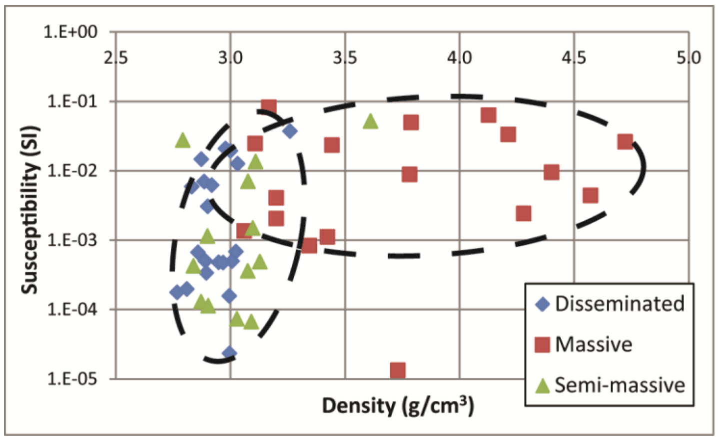

Figure 2-6: Cross plot of sulphidic samples differentiated on bedding type. All samples are located within the Tetagouche block.

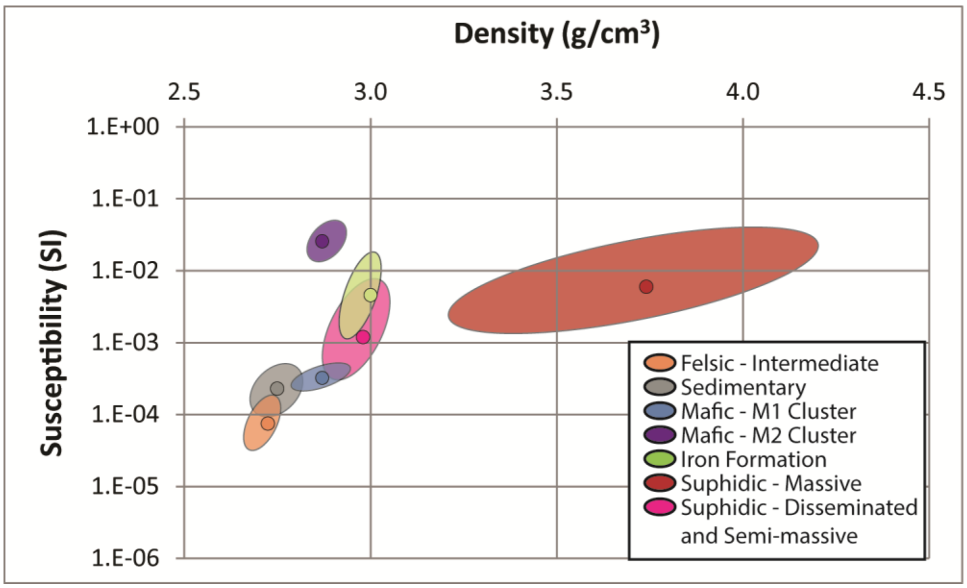

Figure 2-7: Probability plot for the five rock types discussed. The center dot represents sample mean and surrounding ellipse 25th to 75th quartile.

and body geometry based on the overlap of the ellipses. With the exception of iron formations and disseminated sulphides all lithologies have unique central mean co-ordinates. There is overlap between the ellipse of most bulk lithologies which for example could mean that a rhyolite and sedimentary sequence cannot be differentiated in a geophysical modeling exercise. The important massive sulphide population is distinct relative to all other lithologies and should therefore be easily modeled jointly.

Nine-Mile Synform GM-SYS model Profile

The Nine-Mile Synform (NMS) is a prominent D_4 structural feature in the northern half of the Bathurst Mining Camp (Figure 2-1). Both the synform and the adjacent Tetagouche Antiform (TA) were created during regional tectonic uplift and exhumation of the Brunswick subduction complex following slab breakoff (van Staal et al., 2003). The 17 km joint gravity-magnetic profile (Figure 2-1, Figure 2-8) begins just west of the TA hinge line, bearing 110° across the NMS and ending in Boucher Brook Formation in the California Lake Group. Surficial geologic contacts and structural relationships for the model were acquired from the van Staal et al., (2003) and van Staal et al., (2008). Tectono-stratigraphic relationships within individual nappes and across tectonic blocks were developed from van Staal et al., (2003) and van Staal et al., (2008). Magnetic data used for modelling was acquired from the Geologic Survey of Canada's Geoscience Data Repository (GDR) through Geosoft's Oasis Montaj Data Seeker extension. The data was acquired in 1995 during an Aerodat multi-parameter survey flown for the New Brunswick Department of Natural Resources and Energy, Minerals and Energy Division and the Geological Survey of Canada. Survey specifications followed a mean terrain clearance of 60 m with the magnetometer towed 15 m below the helicopter. Flight and tie lines are 200 m and 2000 m respectively. Processing and geologic interpretation of the magnetic dataset is discussed in Keating et al., (1998) and Keating et al., (2003). Gravity data, also downloaded from the GDR, was reprocessed to a Bouguer slab correction of 2.70 g/cm^3. This new value was chosen because the density measurements suggest a local average in the BMC greater than the original Bouguer correction factor of 2.67 g/cm^3. Aside from the new Bouguer slab value, all reprocessing was synonymous to the original dataset, described in Morris R., et al., (2007).

Geologically the profile is very complex, numerous D_1 and D_2 thrusts running perpendicular to the profile were later refolded by D_3 and D_4 tectonics. Major tectonic blocks were first defined then subsequently divided into their respective internal nappes. Structural relationships across nappes were defined at depth from the tectono-stratigraphic relationships and down dip-projection of the currently accepted geologic map (van Staal et al., 2008). Nappes were then internally subdivided into their respective Formations from the geologic map. Rock property information is based on Tables 2-1 and 2-2 and the bivariate probability plot. Local changes in physical property were introduced where necessary to achieve acceptable match between the observed and the computed signal. The geologic maps where available discriminate rock units at a formation level. In some instances this subdivision is not compatible with the observed geophysical signal which indicates there may be several rock types within a single formation. For example, the Sormany Formation of the Fournier Group for example is primarily basalt, but it also contains lesser amounts of diabase and gabbro. Using the exact value for basalt may not accurately model the formation.

Results of the geophysical profile are shown in Figures 2-8 and 2-9. Most of the contacts are defined as being near vertical. In the model the contacts are extended to a maximum depth of 5 km, it is likely they extend to some distance beyond, but the geophysics does not provide any meaningful constraint below this point (> 5 km). The structure is primarily divided on the basis of the D_1 and D_2 nappes (Figure 2-9). Within each thrust panel there are meso-scale folds which do not cross these boundaries. This indicates the major thrust surfaces, as expected, represent major tectonic boundaries with considerably different deformation histories prior to amalgamation. On a macro-scale the NMS must infold at depths of approximately 4 km. Part of the Sormany Formation must come up to the near surface (~1 km) from below the Millstream Formation to satisfy the gravity data. The Spruce Lake Nappe (SLN) exists on both sides of the profile, as well the Lucky Lake Nappe further east. It is unclear how continuous these nappes are around the nose of the fold. The California Lake block consists of 4 imbricated nappes (CLL 1-4). CLL 1 thins with depth and may pinch out at some point. CLL 3 conversely thickens with depth. We have it modeled that a sequence of Boucher Brook mafic volcanics pinching in and thickening at depth. This would imply internal imbrication within the CLL3 nappe as depositionally the California Lake Formation conformably underlies the Boucher Brook Formation. We have drawn this conclusion from down dip projection where internal imbrication of the Boucher Brook Formation is present. The exact thickness or whether California Lake mafic volcanics underlies the Boucher Brook is unclear because the Boucher Brook mafic volcanics and California Lake mafic volcanics are petrophysically identical. CLL 2 and CLL 4 blocks are also petrophysically similar and their juxtaposition is marked by a small magnetic anomaly of repeating Boucher Brook sediments – California Lake mafics sequences. At depth an increasing amount of California Lake mafics is introduced into the CLL 2 nappe to satisfy the gravity anomaly. A sliver of Mount Brittan Formation is also introduced at depth in the CLL 2 nappe which becomes an anticlinal feature to the south of the profile. The contacts between the CLL 4–SLN and SLN-CLL2 is tectonic and also represents a major thrust surface. Immediately east of this we have modelled a syncline within the CLL 2 block. Again this feature becomes more obvious south of the profile but also must exist here. Finally the CLL 2 and SLN contact does not produce a gravity or magnetic anomaly and is therefore not included in the model. At surface both are Boucher Brook sediments though at depth this thrust contact may truncate the California Lake mafics of the CLL 2 nappe.

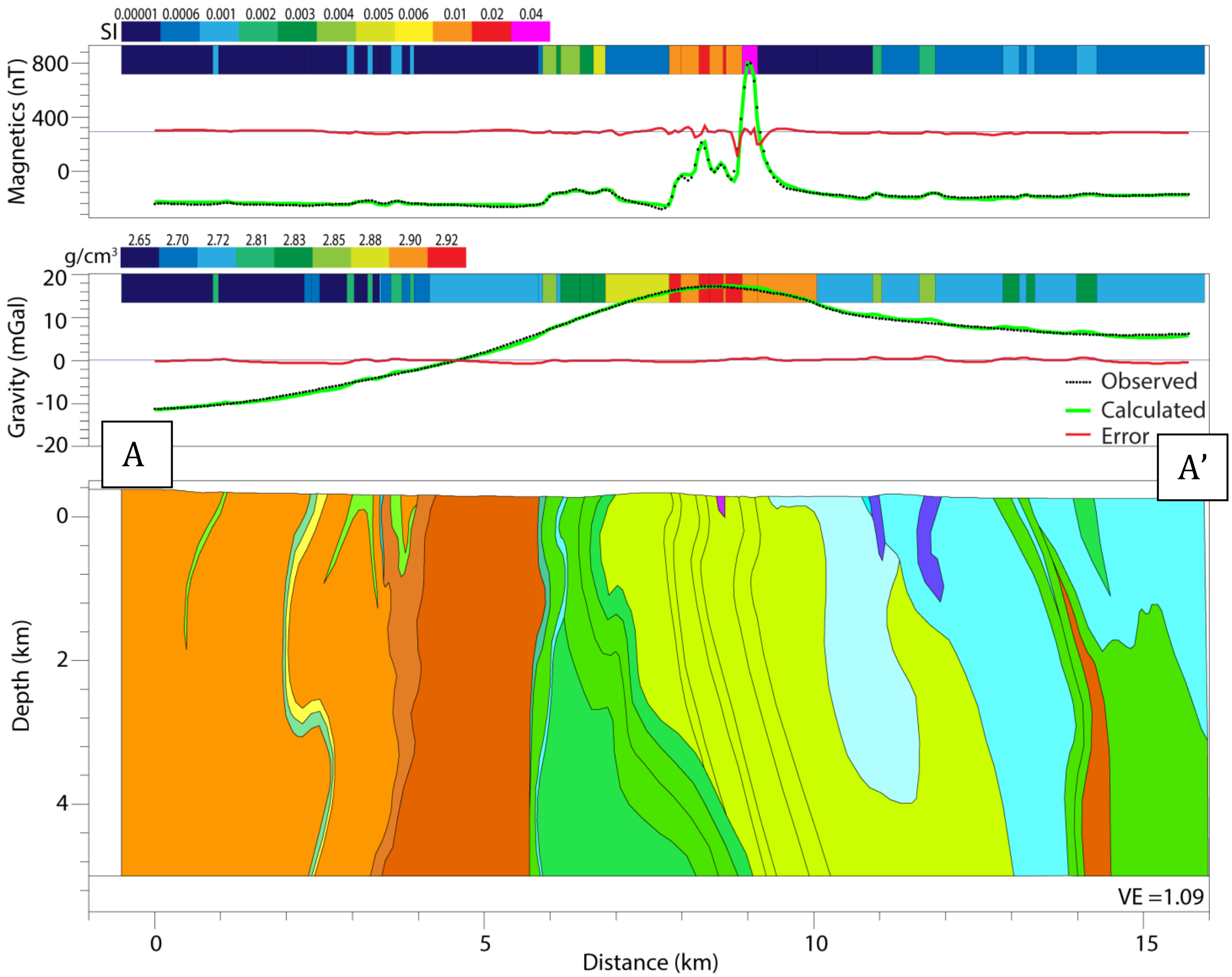

Figure 2-8: Geophysical profile across the Nine Mile Synform. Refer to Figure 2-9 for legend.

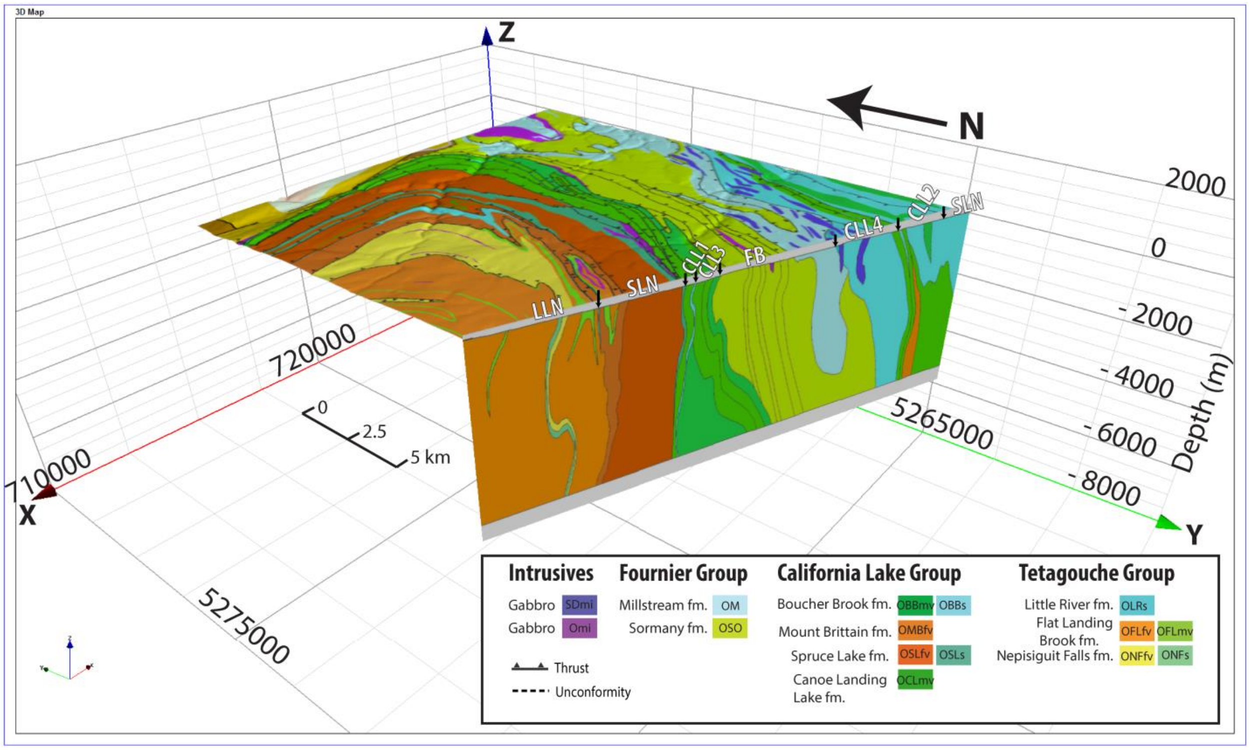

Figure 2-9: Perspective view of geophysical profile from Figure 2-8. LLN = Lucky Lake Nappe, SLN = Spruce Lake Nappe, CLL = California Lake Nappe, FB = Fournier Block.

There are some instances in the model where different densities and/ or susceptibilities are assigned to identical formations. Primarily this is due to local compositional differences. The FB for example has several adjacent units defined as OSO that have different MS and slightly different density values. The MS can be altered based on the relative abundance M1 versus M2 mafic populations or more specifically the relative abundances of the individual rock types within (i.e. amount of basalt vs. gabbro). This is also the case for density; denser blocks likely have a greater percentage of denser gabbro to basalt. There are also some instances within the FB in which thrust surfaces defined on the geologic map do not correspond to thrust in the geophysical model. Quite simply the geologic thrusts do not produce a geophysical contrast and therefore cannot be quantitatively modelled.

Armstrong B Deposit Remanence determination Inversion Model

The Armstrong B deposit is located on the east limb of the Tetagouche Antiform (Figure 2-1). The deposit consists of disseminated to massive-sulphides hosted in a mixed sequence of ash, feldspar-crystal and lithic-lapilli tuffs of the Spruce Lake Formation (SLF) (Thomas et al., 2000). Sulphide mineralization forms a lensed shape deposit striking roughly north and dipping east at 65°. The geometry of the body is constrained at a number of locations by drill-hole intercepts. The deposit produces a positive oval shaped anomaly of 50 nT in the total magnetic field which is broader than the projected surface outcrop trace (Figure 2-10A). Through an abundance of magnetically susceptible pyrrhotite the deposit generates an anomaly with the surrounding magnetically weak felsic tuffs of the SLF. Magnetic susceptibility measurements by Thomas et al., (2000) show felsic tuffs in the area to have average MS values of 0.2×10^{-3} SI which is very close to the 0.1×10^{-3} SI average for all felsic tuffs measured in this study.

Magnetic data for this section comes from a 2004 Fugro Airborne Survey Megatem II survey contracted by the Government of New Brunswick and Noranda Inc (now Xstrata Zinc). Survey specifications followed a mean terrain clearance of 120 m with flight and tie lines at 200 m and 2000 m respectively. The magnetometer was towed 95 m behind the fixed wing aircraft and 73 m above the topographic surface. At the Armstrong B location two adjacent survey blocks (Block 2 and Block 3) overlap. These blocks have different line azimuths (Block 2 = 148°; Block 3 = 109°). By first microleveling the data from each block independently and then stitching the outputs of the two blocks together in a single database, better spatial control on the Armstrong B anomaly is achieved. In essence merging data from the two blocks increased the data density over the anomaly. A slight NW-SE regional trend was removed from the study area using a 500 m non-linear filter for regional residual separation (Keating and Pinet, 2011).

The results of the inversion routine described in the methods section are presented in Figure 2-10 and Table 2-3. The RMS error between the observed field (Figure 2-10A) and modelled field (Figure 2-10B) is 2.79 indicating a very close fit. The resultant Armstrong B anomaly itself closely matches the observed field. The misfit between the observed and calculated anomalies can be mainly attributed to an interfering magnetic anomaly associated with a large adjacent source body. During the inversion computation the estimated width of the magnetic source body increased from 25 m to 163.9 m to accommodate the broad anomaly (Figure 2-10B'). There are two possible explanations for this mis-match between the known geology and the model solution. First, there is fundamental spatial resolution imposed by the height of the magnetic sensor above the ground and the sampling rate of the sensor. Both factors would increase the width of the anomaly. Second, it is possible that the model is describing the ore body and its alteration halo which may contain sufficient pyrrhotite to also register as a magnetic anomaly. The depth extent is also increased from 183 m to 343 m which can be attributed to the difficulty geophysical inversion models have at defining depth extents and again the spatial resolution of the gridded data.

Remanence may either be acquired during deposition or metamorphism but it is always representative of a specific time period in the geologic past. In the case of the BMC Morris B., et al., (2007) observed magnetic remanence at the Stratmat Deposit and given the conspicuous nature of the Armstrong B anomaly, we suspect it too may contain a remanence component. Acquisition or blocking of remanence is always linked to some geological event. Timing of the geological event could range from a primary depositional record to a later thermo-chemical reset associated with peak metamorphism, or fluid expulsion events. The upper age bound for remanence acquisition is the depositional age of the hosting SLF; 471 Ma (NB Energy and Mines, 2013), while the lower age limit compatible with the geologic evidence is the end of the Salic orogenic episode; 418 Ma (van Staal et al., 2008). We speculate the remanence is most likely representative of D_1 or D_2 times when sulphides were recrystallized and underwent major remobilization (Goodfellow et al., 2003). Using the comprehensive Phanerozoic apparent polar wander path by Torsvik et al., (2012) for the Laurentian supercontinent we can estimate the expected remanence directions for the location of the Armstrong B deposit during the time period between 470 Ma to 420 Ma (Table 2-3). By comparing these directions with our results we are accepting that the area around the Armstrong B deposit was fully attached to Laurentia at the time of remanence acquisition. The Koenigsberger (Q) ratio solved from the inversion is 1.35 implying the remanent field is slightly stronger than the inducing field, but the two are very comparable. The remanent magnetic intensity, inclination and declination estimated by the inversion are 35.24, -7.0° and 172.3° respectively.

The remanence direction computed through the inversion differs from the anticipated remanence direction by slightly over 30^{o}. Most of this difference is in the inclination of the computed remanence vector. There are two possible explanations for apparent difference in the remanence vector; 1) the computed direction contains some portion of the Present Earth's Field, that is the susceptibility we used is slightly incorrect, or 2) the rocks have been

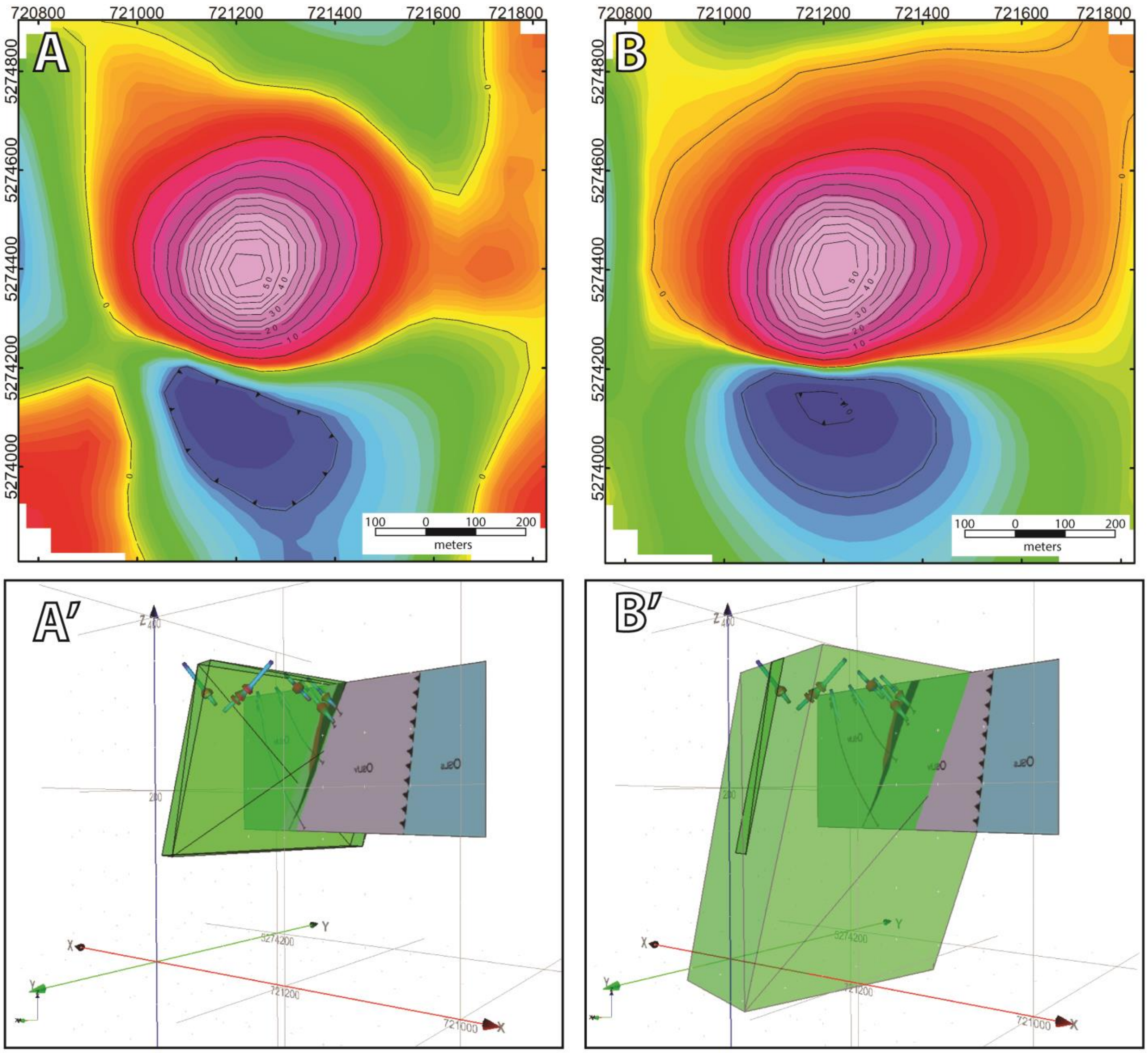

Figure 2-10: Remanence inversion input and results. (**A**) The observed magnetic signal of the Armstrong B deposit. (**A'**) Input geophysical model with reference information. (**B**) Resultant magnetic signal. (**B'**) Resultant geophysical model.

tectonically rotated (tilted) subsequent to acquisition of the remanence direction. If option 1) is valid then the model remanence vector should fall on a great circle path between the Present Earth's Field direction and the expected remanence direction. Alternatively, if option 2 is appropriate then the difference between the model remanence direction and the expected remanence direction should fall on a small circle path with the axis of the small circle describing the strike of the fold axis. As shown by Figure 2-11 on the basis of the evidence provided by this study it is not possible to definitively differentiate between the two options. Option 1 does indeed outline a simple great circle path which intersects the Apparent Polar direction path between the time period 430 Ma and 420 Ma. This timespan coincides with the estimated peak of the Salinic orogeny: 430 Ma – 423 Ma (van Staal et al., 2008). Option 2, in contrast requires a tilt of approximately 30^o but the strike of this tilt rotation axis is perpendicular to the current strike of the Armstrong B deposit. It must be remembered that the California Lake block in which the Armstrong B deposit is located was buried at 14 – 20 km depth after incorporation into the BSC and later uplifted during exhumation. It is possible that the this remanence was acquired during the cooling accompanying exhumation. Two deformation event followed peak metamorphism (D_3 and D_4) during buoyant rise of the BMC in the Late Silurian – Early Devonian. It is possible that local deformation during D_3 or D_4 affected the Armstrong B area, tilting it, but not resetting the remanence vector.

Conclusion

Physical rock property information is a critical component of any geophysical modelling or interpretation exercise. When used in conjunction with the known geology and/ or drill-hole information the uncertainty in the geophysical solution is greatly reduced. This paper has built upon the physical rock property database originally created by Thomas et al., (2000) and Mwenifumbo et al., (2003) for the Bathurst Mining Camp. Descriptive statistics including mean, standard deviation, median and 25th and 75th quartiles are calculated for density and magnetic susceptibility measurements and listed for a variety of rock types. Density-magnetic susceptibility bivariate plots are used to compare the natural trends of the different lithologies and bedding styles against each other. A probabilistic bivariate plot is also generated to provide a geologically realistic starting point for any geophysical modelling exercise. Suitable modelling expectations has also been discussed and we agree with Mwenifumbo et al., (2003) and Thomas (2003) that gravity and magnetic surveys, especially when used in conjunction with one another, should be an excellent exploration tool for massive sulphide deposits either by direct targeting or indirectly detecting iron formations.

The physical property information collected has also been used to generate two geophysical models within the Camp; joint gravity-magnetic profile model across the NMS and a 3-D remanence inversion of the Armstrong B anomaly. The NMS profile reveals the deep

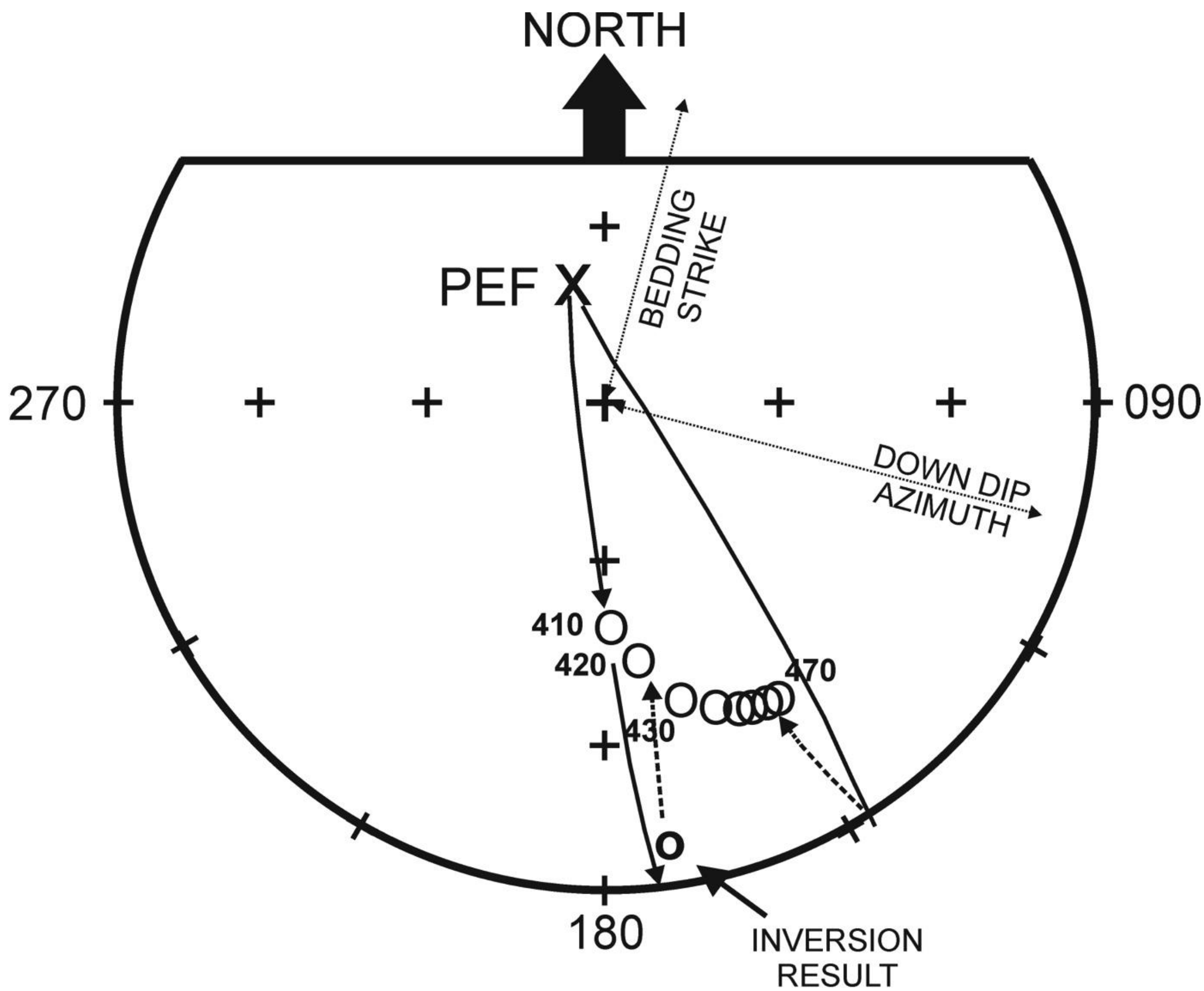

Figure 2-11: Estimated and inverted remanence values.

structure of the BMC. The major tectonic nappes of the camp are shown to be highly deformed. The geometry of most lithologic and tectonic surfaces is near vertical. Within each nappe there are unique deformation trends which are truncated at the thrust surface with adjacent nappes. The Fournier Block must infold at depth under the Millstream Formation and come back up near surface. All nappes extend to at least 5 km depth, but their total depth extents are not defined. Constrained inversion modeling of the magnetic anomaly associated with the Armstrong B deposit indicates this anomaly has a strong magnetic remanence component. The strength of the remanence field is of a comparable magnitude to that of the inducing field. The model calculated remanent declination is very close to the expected direction calculated from the reference APWP for continental Laurentia. The difference between the model calculated and APWP expected direction can be explained either in terms of partial overprinting of the remanence direction by a component of the Present Earth's Field direction, or by later tilting along an axis perpendicular to current strike of the Armstrong B deposit. Irrespective of which option is preferred the model confirms that remanence acquisition occurred concurrently with the estimated peak in the Salinic orogeny (423 – 430 Ma).

Table 2-1: Density statistics

Density *(g/cm^3)*						
Rock Type (1271)	N	$\bar{x}$	s	Q_1	Q_2	Q_3
***Mafic** (165)*						
Basalt	105	2.85	0.11	2.77	2.86	2.93
Blueschist	9	2.88	0.08	2.84	2.86	2.92
Diabase	7	2.91	0.08	2.86	2.88	2.94
Gabbro	36	2.90	0.11	2.82	2.87	2.99
Mafic Dyke	8	2.91	0.07	2.93	2.93	2.94
***Sedimentary** (240)*						
Argillite	37	2.79	0.04	2.76	2.78	2.82
Graphitic Argillite	11	2.76	0.04	2.73	2.75	2.78
Chert	8	2.68	0.08	2.65	2.69	2.72
Phyilite	8	2.78	0.10	2.72	2.76	2.84
Phylonite	2	2.73	0.06	2.71	2.73	2.75
Quartzite	11	2.68	0.05	2.64	2.68	2.71
Sericitic / Chloritic sediments	12	2.81	0.04	2.79	2.80	2.83
Shale	30	2.72	0.10	2.66	2.72	2.77
Siltstone	16	2.65	0.09	2.63	2.68	2.69
Siltstone and Shale*	107	2.74	0.09	2.68	2.74	2.79
Slate	8	2.73	0.09	2.67	2.70	2.75
Tuffaceous Sediments	21	2.83	0.08	2.77	2.81	2.87
Turbidite	5	2.73	0.15	2.64	2.67	2.76
***Iron Formation** (10)*						
Iron Formation	10	3.00	0.15	2.93	2.97	3.02
***Felsic – Intermediate** (806)*						
Granite	5	2.62	0.07	2.57	2.58	2.68
Ash Tuff	30	2.71	0.05	2.68	2.71	2.73
Crystal Tuff	193	2.73	0.05	2.70	2.73	2.75
Dacite	4	2.68	0.01	2.66	2.68	2.69
Felsic Tuff	82	2.74	0.07	2.70	2.74	2.78
Quartz Feldspar Augen Schist	11	2.69	0.08	2.67	2.68	2.76
Quartz Feldspar Porphyry	163	2.69	0.07	2.65	2.70	2.72
Rhyolite	225	2.71	0.07	2.67	2.71	2.74
Rhyolite Agglomerae	22	2.69	0.03	2.66	2.68	2.71
Rhyolite Tuff	45	2.72	0.10	2.64	2.72	2.75
Volcaniclastic	30	2.70	0.10	2.64	2.70	2.74
***Sulphide** (50)*						
Massive	17	3.74	0.94	3.20	3.73	4.21
Semi-massive	13	3.04	0.21	2.90	3.08	3.10
Disseminated	20	2.94	0.89	2.88	2.93	3.00

* Uses the 30 shale and 16 siltstone listed plus 61 additional samples which were not differentiated into either lithology.

Table 2-3: Magnetic susceptibility statistics

Susceptibility *(SI)*						
Rock Type (1271)	*N*	$\bar{x}$ *(SI x 10^{-3})*	*S* *(Si x 10^{-6})*	Q_1 *(SI x 10^{-3})*	Q_2 *(SI x 10^{-3})*	Q_3 *(SI x 10^{-3})*
Mafic *(165)*						
Basalt	105	0.48	4.9	0.24	0.36	0.54
Blueschist	9	2.66	6.6	0.42	2.13	10.35
Diabase	7	0.47	6.0	0.22	0.30	0.38
Gabbro	36	0.37	3.1	0.24	0.38	0.48
Mafic Dyke	8	0.81	5.5	0.30	0.54	0.85
Sedimentary *(240)*						
Argillite	37	0.25	2.34	0.15	0.24	0.34
Graphitic Argillite	11	0.23	4.63	0.11	0.18	0.11
Chert	8	0.40	7.30	0.15	0.28	0.52
Phyilite	8	0.23	1.72	0.16	0.22	0.34
Phylonite	2	0.14	1.69	0.12	0.14	0.17
Quartzite	11	0.05	3.00	0.02	0.06	0.10
Sericitic / Chloritic Sediments	12	0.26	1.64	0.18	0.31	0.36
Shale	30	0.21	5.95	0.10	0.18	0.36
Siltstone	16	0.09	5.29	0.04	0.08	0.14
Siltstone and Shale*	107	0.20	5.14	0.09	0.19	0.51
Slate	8	0.19	2.47	0.13	0.19	0.29
Tuffaceous Sediments	21	1.08	4.84	0.41	0.79	2.60
Turbidite	5	0.22	1.70	0.18	0.20	0.38
Iron Formation *(10)*						
Iron Formation	10	4.59	4.73	1.17	3.53	17.81
Felsic – Intermediate *(806)*						
Granite	2	0.05	2.5	0.03	0.05	0.08
Ash Tuff	30	0.11	2.1	0.06	0.10	0.18
Crystal Tuff	193	0.09	2.8	0.05	0.11	0.18
Dacite	3	0.053	4.0	0.03	0.05	0.09
Felsic Tuff	82	0.11	3.0	0.06	0.12	0.24
Quartz Feldspar Augen Schist	11	0.11	2.3	0.05	0.16	0.20
Quartz Feldspar Porphyry	163	0.05	3.3	0.02	0.05	0.12
Rhyolite	225	0.08	3.6	0.05	0.09	0.18
Rhyolite Agglomerae	22	0.04	3.3	0.01	0.04	0.09
Rhyolite Tuff	45	0.08	4.0	0.03	0.08	0.18
Volcaniclastic	30	0.05	3.9	0.01	0.05	0.14
Sulphide *(50)*						
Massive	17	5.99	8.67	2.05	8.87	26.18
Semi-massive	13	1.02	9.84	0.130	0.49	7.02
Disseminated	20	1.48	7.78	0.435	0.67	8.10

* Uses the 30 shale and 16 siltstone listed plus 61 additional samples which were not differentiated into either lithology.

Table 2-3: Remanence estimation from APWP and results from geophysical inversion

Age	Estimate Declination	Estimated Inclination	Recovered Declination	Recovered Inclination
410	178.3	-52.6		
420	**173.2**	**-46.4**	172.3	-7.0
430	**165.5**	**-37.8**		
440	160.3	-34.5		
450	157.7	-33.8		
460	155.7	-33.4		
470	154.2	-33.4		
480	151.2	-32.4		

References

Baranov, V., 1957. A new method for interpretation of aeromagnetic anomalies: Pseudo-gravimetric anomalies. Geophysics, **22**, 359-383.

Bott, M. H. P., Smith, R.A., and Stacey, R. A., 1966. Estimation of the direction of magnetization of a body causing a magnetic anomaly using a pseudogravity transformation. Geophysics, **31,** 803-811.

Foss, C., and McKenzie, B., 2011. Inversion of anomalies due to remanent magnetisation: an example from the Black Hill Norite of South Australia. Australian Journal of Earth Sciences 58, 391-405.

Foss, C., McKenzie, K.B., and Hillan, D., 2012. A robust approach to estimation of magnetization direction from interpretation of magnetic field data. SEG Technical Program Expanded Abstracts 2012, pp. 1-5. doi: 10.1190/segam2012-1550.1

Goodfellow, W.D., 2007. Metallogeny of the Bathurst Mining Camp, northern New Brunswick. *In* Mineral Deposits of Canada: A Synthesis of Major Deposit-Types, District Metallogeny, the Evolution of Geological Provinces, and Exploration Methods. *Edited by* W.D. Goodfellow. Geological Association of Canada, Mineral Deposits Division, Special Publication No. 5, 449-469.

Goodfellow, W.D., and McCutcheon, S.R., 2003. Geologic and genetic attributes of volcanic sediment-hosted massive sulfide deposits of the Bathurst Mining Camp, Northern New Brunswick. *In* Massive Sulfide Deposits of the Bathurst Mining Camp, New Brunswick, and Northern Maine. *Edited by* W.D., Goodfellow, S.R., McCutcheon, and J.M., Peter. Economic Geology Monograph 11, 245-302.

Keating, P.B., Kiss, F.G., Katsube, J., Best, M.E., 1998. Airborne conductivity mapping of the Bathurst Mining Camp. Exploration Geophysics, **29**, 211-217.

Keating, P., Thomas, M.D., and Kiss, F.G., 2003. Significance of a high resolution magnetic and electromagnetic survey for exploration and geologic investigation, Bathurst Mining Camp, *In* Massive Sulfide Deposits of the Bathurst Mining Camp, New Brunswick, and Northern Maine. *Edited by* W.D., Goodfellow, S.R., McCutcheon, and J.M., Peter. Economic Geology Monograph 11, 783-798.

Li, Y., Shearer, S., Haney, M., and Dannemiller, N., 2010. Comprehensive approaches to 3D inversion of magnetic data affected by remanent magnetization. Geophysics, **75**, L1 – L11.

Lee, M.D., and Morris, W.A. 2012. Comparison of magnetic susceptibility meters using rock samples from the Wopmay orogen, Northwest Territories, Canada. Geological Survey of Canada, Current Research, in press.

McCrutcheon, S.R., Luff, W.M., and Boyle, R.W., 2003. The Bathurst Mining Camp, New Brunswick, Canada: History of discovery and evolution of the Geologic Models. *In* Massive Sulfide Deposits of the Bathurst Mining Camp, New Brunswick, and Northern Maine. *Edited by* W.D., Goodfellow, S.R., McCutcheon, and J.M., Peter. Economic Geology Monograph 11, 17-35.

Morris, R., Jobin, D.M., Thomas, M.D., Rogers, N., McCutcheon, S.R. 2007. New gravity data for the Bathurst Mining Camp, Northeastern New Brunswick: A colour-shaded Bouguer gravity anomaly map (linear colour contour intervals) with gravity station locations and posted Bouguer Anomaly values. Geologic Survey of Canada, Open File 5542. New Brunswick Department of Natural Resources, Minerals, Policy and Planning Division, Plate 2007-13A.

Morris, B., Ugalde, H. and Thomson, V., 2007. Magnetic remanence constraints on magnetic inversion models. The Leading Edge, **26**, 960-964.

Morris, W. A., Spicer, B., Tschirhart, P., Tschirhart, V., Lee, M.D., and Ugalde, H., 2012. Integrating geological constraints in geophysical models. SEG Technical Program Expanded Abstracts 2012: pp. 1-5. doi: 10.1190/segam2012-0487.1

Mwenifumbo, C.J., Elliot, B.E., and Street, P., 2003. Borehole geophysical characteristics of massive sulfide deposits in the Bathurst Mining Camp. *In* Massive Sulfide Deposits of the Bathurst Mining Camp, New Brunswick, and Northern Maine. *Edited by* W.D., Goodfellow, S.R., McCutcheon, and J.M., Peter. Economic Geology Monograph 11, 841-860.

New Brunswick Department of Energy and Mines, 2013. New Brunswick Bedrock Lexicon, Spruce Lake Formation. http://dnr-mrn.gnb.ca/Lexicon/Lexicon/Lexicon_View.aspx. June 19, 2013

Paterson, N. R. and Reeves, C. V., 1985. Applications of gravity and magnetic surveys: The state-of-the-art in 1985. Geophysics, **50**, 2558-2594.

Peter, J.M., Kjarsgaard, W.D., and Goodfellow, W.D., 2003. Hydrothermal sedimentary rocks of the Heath Steele Belt, Bathurst Mining Camp, New Brunswick: Part 1. Mineralogy and mineral chemistry. *In* Massive Sulfide Deposits of the Bathurst Mining Camp, New Brunswick, and Northern Maine. *Edited by* W.D., Goodfellow, S.R., McCutcheon, and J.M., Peter. Economic Geology Monograph 11, 391-416.

Roest, W. and Pilkington, M., 1993. Identifying remanent magnetization effects in magnetic data. Geophysics, **58**, 653-659.

Rogers, N., can Staal, C.R., Winchester, J.A., and Fyffe, L.R., 2003a. Provenance and chemical stratigraphy of the sedimentary rocks of the Miramichi, Tetagouche, California Lake, and Fourier Groups, Northern New Brunswick. *In* Massive Sulfide Deposits of the Bathurst Mining Camp, New Brunswick, and Northern Maine. *Edited by* W.D., Goodfellow, S.R., McCutcheon, and J.M., Peter. Economic Geology Monograph 11, 111-128.

Rogers, N., van Staal, C.R., McNicoll, V., and Thériault, R., 2003b. Volcanology and tectonic setting of the Northern Bathurst Mining Camp: Part 1. Extension and rifting of the Popelogan Arc. *In* Massive Sulfide Deposits of the Bathurst Mining Camp, New Brunswick, and Northern Maine. *Edited by* W.D., Goodfellow, S.R., McCutcheon, and J.M., Peter. Economic Geology Monograph 11, 157-180.

Schnetzler, C. and Taylor, P. T., 1984. Evaluation of an observational method for estimation of remanent magnetization. Geophysics, **49**, 282-290.

Thomas, M.D., Walker, J.A., Keating, P., Shives, R., Kiss, F., and Goodfellow, W.D., 2000. Geophysical atlas of massive sulphide signatures, Bathurst mining camp, New Brunswick. Geological Survey of Canada, Open File 3887; and New Brunswick Department of Natural Resources and Energy; Minerals and Energy Division, Open File 2000-4, 105 pp.

Thomas, M.D., 2003. Gravity signatures of massive sulfide deposits, Bathurst Mining Camp, New Brunswick. *In* Massive Sulfide Deposits of the Bathurst Mining Camp, New Brunswick, and Northern Maine. *Edited by* W.D., Goodfellow, S.R., McCutcheon, and J.M., Peter. Economic Geology Monograph 11, 799-817.

Torsvik, T. H., Van der Voo, R., Preeden, U., Mac Niocaill, C., Steinberger, B., Doubrovine, P. V., ... & Cocks, L. R. M., 2012. Phanerozoic polar wander, paleogeography and dynamics. Earth-Science Reviews, **114**, 325-368.

van Staal, C.R., Wilson, R.A., Rogers, N., Fyffe, L.R., Langton, J.P., McCutcheon, S.R., McNicoll, V., and Ravenhurst, C.E., 2003. Geologic and tectonic history of the Bathurst Supergroup, Bathurst Mining Camp, and its relationship to coeval rocks in Southwestern New Brunswick and adjacent Maine - A synthesis. *In* Massive Sulfide Deposits of the Bathurst Mining Camp, New Brunswick, and Northern Maine. *Edited by* W.D., Goodfellow, S.R., McCutcheon, and J.M., Peter. Economic Geology Monograph 11, 37-60.

van Staal, C.R., Currie, K.L., Rowbotham, G., Goodfellow, W., Rogers, N., 2008. Pressure-temperature paths and exhumation of Late Ordovician-Early Silurian blueschists and associated metamorphic nappes of the Salinic Brunswick subduction complex, northern Appalachians. GSA Bulletin, **120**, 1455-1477

Zietz, I. and Andreasen G. E., 1967. Remanent magnetization and aeromagnetic interpretation. In Mining Geophysics; Society of Exploration Geophysicists, **2**, 569-590.

Chapter Three: A new regional-residual separation for magnetic datasets using susceptibility from frequency domain electromagnetic data

Peter Tschirhart[1], Bill Morris[1], Greg Hodges[2]

[1] *MAGGIC, SGES, McMaster University, Hamilton ON, L8S 4K1*

[2] *Fugro Airborne Surveys, Mississauga, ON, L5N 5S2*

Abstract

Regional-residual separation is a fundamental processing step required before interpreting any magnetic anomaly data. Numerous methods have been devised to separate deep-seated long wavelength (regional) anomalies from the near surface high frequency (residual) content. Such methods range in complexity from simple wavelength filtering to full 3D inversions, but all rely on the fundamental assumption that long wavelengths are solely caused by deep source bodies; an incorrect assumption in some geologic environments. Herein we present a new method for determining the contributions of near surface magnetic sources using frequency domain helicopter electromagnetic (HFEM) data. We invert the in-phase and quadrature components of the HFEM data to produce an estimate of the spatial variation of magnetic susceptibility. Using this susceptibility information along with known topography and original survey flight path data we calculate a magnetic intensity grid by forward modeling. There are two immediate benefits to this approach. First, HFEM systems have a limited effective depth of penetration, within the first hundred meters from surface, so any magnetic sources detected by this method must be located in the near surface. Second, the HFEM derived susceptibility is completely independent of magnetic remanence. In contrast apparent susceptibility computed from the original magnetic intensity data incorporates all magnetic signal sources in its derivation. Cross-plotting of MS_{HFEM} versus MS_{TMI} serves to reveal areas where the observed magnetic field is dominated by magnetic remanence and provides an estimate of the polarity of the remanence contribution.

We present an example of this method from an area in the Bathurst Mining Camp, New Brunswick. Though broadly successful caution is needed when using this method since near surface conductive bodies and anthropogenic sources can cause erroneous HFEM susceptibility values, which in turn produce invalid magnetic field estimates in the forward modeling exercise.

Introduction

Regional-residual separation is one of the most important processing steps applied to potential field data. The magnetic, or gravity field, at any observation point records the summation of contributions from all sources. The goal of all regional-residual separation procedures is to isolate a regional signal caused by deep seated / buried magnetic sources from a residual signal which can be attributed to near surface source bodies: sources which outline lithological variations that might be detected by a field geologist. However, the procedure of regional / residual separation is an interpretive step. Through selection of their approach to regional / residual separation the operator is imposing an interpretation on their data.

A review of the more common traditional methods (upward continuation, downward continuation, band-pass filtering and polynomial surface matching) was presented by Hearst and Morris (2001). Classic techniques such as upward continuation (Nettleton, 1954) and match filters (Spector and Grant, 1970) attribute a uniformly smooth field to the regional signal which is subtracted off leaving behind the residual. Unfortunately, a common failing of many Fourier based filter approaches is that they estimate a correction for the whole image grid irrespective of local signal variation. More recent publications based on wavelength separation of source contributions, for example wavelet analysis (Fedi and Quarta, 1998), or non-linear filtering (Keating and Pinet, 2011, Keating et al., 2011), employ a mathematical approach which attempts to estimate the regional contribution while retaining a spatially variable amplitude that is more appropriate to the original data. Other approaches to regional / residual separation have employed more geological or geophysical reasoning. Roach et al., (1993) for example attempt to estimate the regional contribution through forward modeling of the deep geological structure. Li and Oldenburg, (1998) suggested an equivalent layer extraction approach in which an area thought to represent the residual signal being sought is nulled in the computed equivalent layer, the data is then re-gridded and TMI now representing the regional signal is re-calculated. In reality there are benefits and disadvantages to each routine, but the basic assumption that most commonly employed methods share is that long wavelength anomalies must be representative of deep sources while short wavelength signals represent shallow sources. Though in most cases this assumption holds true, the fundamental exception to this rule is that a long wavelength signal may also be caused by shallow source bodies. A signal separation approach based solely on wavelength could falsely force this source into the subsurface. Consider a model with three source bodies all having the same magnetic susceptibility. Two of the source bodies are located in the near surface, while the third body is buried at depth (Figure 3-1). The small shallow body as expected produces a large amplitude, short wavelength (peaked) anomaly. However, on the basis of wavelength alone it would be nearly impossible to separate the signals contributed by the large buried source body from the thin near surface source body (Figure 3-1). Depending on how the operator chose to filter this data set two possible problems may arise: a) a near surface body that is geologically significant could be erroneously removed from the residual; or b) evidence of the deep – seated source body which may have economic significance is artificially accepted as a near shallow source. Gravity models of the Sudbury Basin structure provide an excellent example of the broad issue of regional / residual separation. Using a forward-modeling approach to estimate the regional signal, Gupta et al., (1984) suggested the Sudbury Basin was underlain by a deep seated dense "hidden layered series". In contrast, McGrath and Broome (1994) used a simple planar surface as their regional signal and consequently found no evidence for the dense buried mass. The non-uniqueness issue that is common to all potential field inversion problems is present in the question of regional / residual separation calculations.

In this paper we present a regional / residual anomaly separation method that has no dependence on the wavelength of the source signal. Rather this method uses apparent susceptibility values calculated from frequency domain helicopter- borne electromagnetic data (HFEM) transformed into magnetic intensity to separate the signal contributed by near surface magnetic sources (residual) from the signal generated by deeper buried sources (regional). Central to this method is the limited depth penetration associated with HFEM systems. The actual depth sampled by a HFEM signal is a function of the frequency employed by the transmitter coil, and the conductivity of the source medium. Most HFEM systems have well defined effective depths of penetration which are generally limited to the first couple hundred meters below the surface.

Another added benefit of this technique is that the EM derived apparent susceptibility (MS_{HFEM}) values are independent of magnetic remanence. When computing apparent magnetic susceptibility (MS_{TMI}) from a reduced to pole total magnetic intensity (TMI) field data set, the contribution of any remanently magnetised source to the total magnetic signal is automatically carried through to the derived susceptibility signal. To demonstrate this effect, consider a simple model where a near surface horizontal sheet is intruded by a series of vertical four tabular bodies (dikes) (Figure 3-2). If all of the five bodies have exactly the same susceptibility then the observed TMI signal would exhibit the signal associated with a simple tabular body; this assumes the lower sections of the tabular bodies contribute very little to the overall signal. The computed MS_{HFEM} and MS_{TMI} in this situation should be nearly identical. If the tabular bodies have a strong remanent magnetisation signal, as diabase dikes often do, then the observed TMI anomaly pattern would be very different. As shown by Figure 3-2 the TMI signal reflects the vector summation of the induced and remanently magnetised field components. If the remanent magnetisation is normally (or vice versa reversely) polarised then the amplitude of the observed TMI signal is augmented (diminished). Computing an apparent MS_{TMI} from this more complex signal would result in a pattern of increased and reduced susceptibility values that are not representative of the true petrophysical properties of the rock. Since the computed

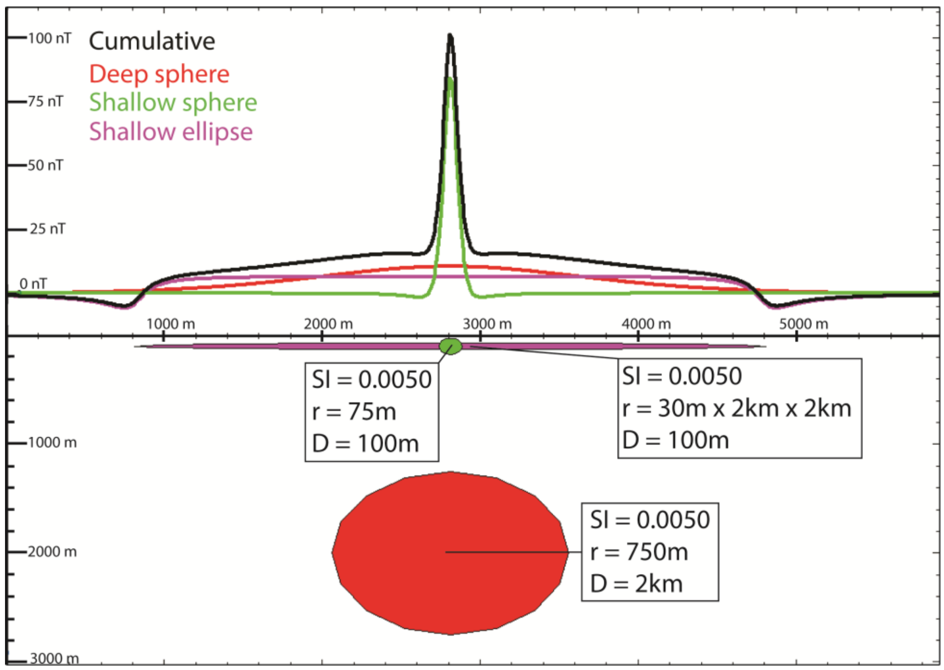

Figure 3-1: A synthetic example illustrating how the magnetic anomaly pattern resulting from source bodies having identical susceptibility is linked to the source body's geometry and depth. Though the shallow sphere produces a distinct high frequency anomaly, both the deep source body and the thin, shallow ellipsoid body produce broad anomalies which makes discriminating source depth from wavelgnth characteristics difficult.

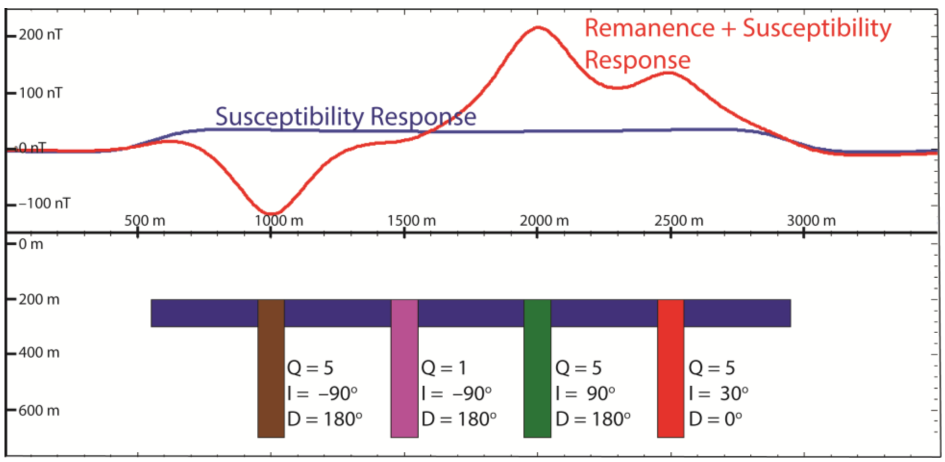

Figure 3-2: Synthetic example comparing the effects of a flat lying magnetic source with purely induced magnetisation (dark blue body) to one intruded by a series of vertical prisms with varying remanent magnetisation directions. All bodies have susceptibility set to 0.01 SI.

MS_{HFEM} profile would be uniform any comparison between MS_{HFEM} and MS_{TMI} should reveal the presence of any remanent magnetisation. Therefore our proposed regional / residual separation procedure also provides a simple technique for revealing the spatial extent of any near surface remanently magnetized bodies.

Herein we present a case study using susceptibility derived from HFEM data to forward model the local magnetic field for a test site in the Bathurst Mining Camp, northern New Brunswick, Canada (Figure 3-3). The results of the forward model are compared against a number of wavelength based residual / residual results in order to gauge 1) the effectiveness of the method at modeling the local near surface magnetic response and 2) determination of an optimum residual for the magnetic data. The effectiveness at locating remanently magnetised bodies is also demonstrated.

Method

Apparent susceptibility mapping from multi-coil coplanar HFEM surveys was first developed by Fraser (1981) as a means of mapping weight percent magnetite. Further developments by (Huang and Fraser, 2000, Huang and Fraser, 2001, Hodges, 2004) led to more robust algorithms better suited to realistic geologic environments and the ability to map all three electric earth parameters (magnetic permeability, dielectric permittivity, and apparent resistivity) simultaneously. EM anomaly patterns, which are generated by the interaction of inducing fields produced by the transmitter coil and the underlying earth exhibit a more spatially restricted / rapid fall-off with distance than standard magnetic surveys. As such apparent susceptibility mapping derived from HFEM surveys allows for tightly spaced magnetic anomalies to be better resolved than by magnetic surveys.

Magnetic susceptibility (κ) is recorded as a negative in-phase component by frequency-domain helicopter-borne electromagnetic systems. While the susceptibility signal is independent of frequency it is most easily detected with low frequency EM signals since at these wavelengths, conductivity, which is frequency dependant, is less dominant (Fraser, 1981, Hodges, 2004). Using the homogeneous half space model developed by Huang and Fraser (2000) the coplanar in-phase frequencies are inverted using a singular value decomposition (SVD) inversion to yield dielectric permittivity, relative magnetic permeability (μ_R), and apparent resistivity. The relative permeability is a function of the complex response between the quadrature (M) and inphase (N) components scaled for variation in flying height (h) and coil separation (s), the induction number (θ) and ratio of secondary (H_s) to primary field (H_0) responses, equation 1 (Huang and Fraser, 2000). It is related to magnetic susceptibility by equation 2.

$$H_s/H_0 = (s/h)^3[M(\theta, \mu_R) + \; iN((\theta, \mu_R)] \quad (1)$$

$$\kappa = \mu_R - 1 \qquad (2)$$

Using the flight path characteristics, sensor elevation, and bandwidth of the recording system it is possible to forward model the total magnetic intensity at each fiducial in the survey database using a series of right sided vertical prisms of homogeneous susceptibility equal to the inverted MS_{HFEM} (Figure 3-4). A single body (voxel) is generated at each fiducial in the database with width and strike length of 5m x 5m such that there is no overlap between bodies. The upper bound of each prism in the voxel fiducial model is defined by the topographic surface which extends 100m below this point. Each voxel thus has dimensions 5m x 5m x 100m. In this example the depth extent of each prism is arbitrarily assigned uniformly across the study area to simplify the calculation. Effectively the depth extent of the source prism only changes anomaly amplitude, and any change in depth extent would produce a proportionally equivalent change across the model area. The resulting TMI anomaly pattern is then computed using an applied field strength of 55,079 nT; the IGRF at the time of the original data acquisition. The field direction of 90^o inclination and 0^o declination is used to position magnetic peak over the centre of the source body and is equivalent to the reduction to magnetic pole filter of the raw TMI data. The products were then inspected in both grid (Figure 3-4) and profile (Figure 3-5) form.

Data

Data for this project was recorded by a helicopter-borne, multi-parameter survey flown over the Bathurst Mining Camp (BMC) for the New Brunswick Department of Natural Resources and Energy, Minerals and Energy Division, and the Geological Survey of Canada. Survey specifications followed a drape surface flown with mean terrain clearance of 60m and flight line spacing of 200m. Four individual survey blocks, totalling 3,920 km^2, were flown roughly perpendicular to local geologic strike beginning May 1995 (Keating et al., 2003). Geophysical sensors included an Aerodat 5 frequency electromagnetic (EM) system towed 30m below the helicopter, a magnetometer towed 15m below the helicopter and a 256 channel spectrometer mounted in the helicopter. The EM sensors transmitter and receiver coil pairs were housed within a 8.4328 m bird separated nominally by 6.54 m. Inphase and quadrature was measured for 5 coil pairs operating at frequencies 914 Hz and 4786 Hz in the coaxial geometry and 853 Hz, 4433 Hz, and 32290 Hz in coplanar orientation. The data was supplied and downloaded from the Geoscience Data Repository DAP application (www.NRCan.gc.ca/geodap) hosted by Natural Resources Canada.

Keating et al., (1998) describe the processing and levelling procedures they applied to the EM data used for this study. However, the initial data required further levelling as severe corrugations existed on a line-by-line basis. The levelled in-phase and quadrature components for the 853 Hz, 4433 Hz and 32 kHz frequencies were then further levelled by visual inspection and subjected to microleveling. Microleveled data showed marked improvements on the original with minimal corrugation, improving the results of the susceptibility inversion. While the entire data set for the whole BMC survey area was levelled and microleveled prior to being processed to computation of MS_{HFEM} only a small portion of the whole area was transformed into apparent magnetic intensity for this study (Figure 3-4).

Study Area

The study area is located within the Bathurst Mining Camp (BMC) (Figure 3-3) on the western limb of the Tetagouche Antiform (TA), bordering the Caribou Synform (CS) to the west. The small 0.25 MT (million tonne) McMaster volcanogenic massive sulphide (VMS) deposit is located within the study area with the larger 65 MT Caribou deposit lying 1.5 km southwest (Figure 3-3), (McCutcheon et al., 2003). Regional metamorphism affected the entire BMC. Polyphase deformation events (D1-D4) occurred as the area was incorporated and exhumed from the Brunswick subduction complex in Late Ordovician to Early Silurian (van Staal et al., 2003). Both TA and CS folds represent D4 structures, are open, upright and doubly plunging (de Roo and van Staal, 1994).

The majority of the area consists of two major tectono-stratigraphic groups, the California Lake and Tetagouche Groups. Locally three lithological types are encountered within the California Lake Group; mafic volcanics of the Boucher Brook (OBB) and Canoe Landing Lake Formations (OCL); felsic volcanics of the Spruce Lake (OSL) and Mount Brittain (OMB) Formations; and shales of OSL and OBB Formations (Figure 3-3). The Tetagouche Group consists locally of two formations and three rock types; mafic volcanics of the Flat Landing Brook (OFL), felsic volcanics of the OFL and Nepisiguit Falls Formation (ONF), and shales of OFL (Figure 3-3). In the northwestern corner of the study area a small amount of mafic volcanics of the Sormany Formation (OSO), part of the Fourier Group and Ordovician synvolcanic gabbros is also encountered. Finally siltstone and sandstones of the Chaleurs Group (SFF) unconformably overlies OSO and intrusive gabbros (Omi) in this area.

Magnetic responses primarily originate from mafic volcanics present in the OFL, OBB and OCL formations. Magnetic susceptibility measurements have systematically shown that the mafic volcanic units are more magnetic than felsic volcanic or sedimentary rocks. Sedimentary rocks are more or less indistinguishable from their felsic volcanic equivalents (Mwenifumbo et al., 2003, Tschirhart, 2013).

The primary conductivity anomalies through the study zone are correlated to shale beds of the California Lake and Tetagouche Groups (Figure 3-3). This observation is compatible with

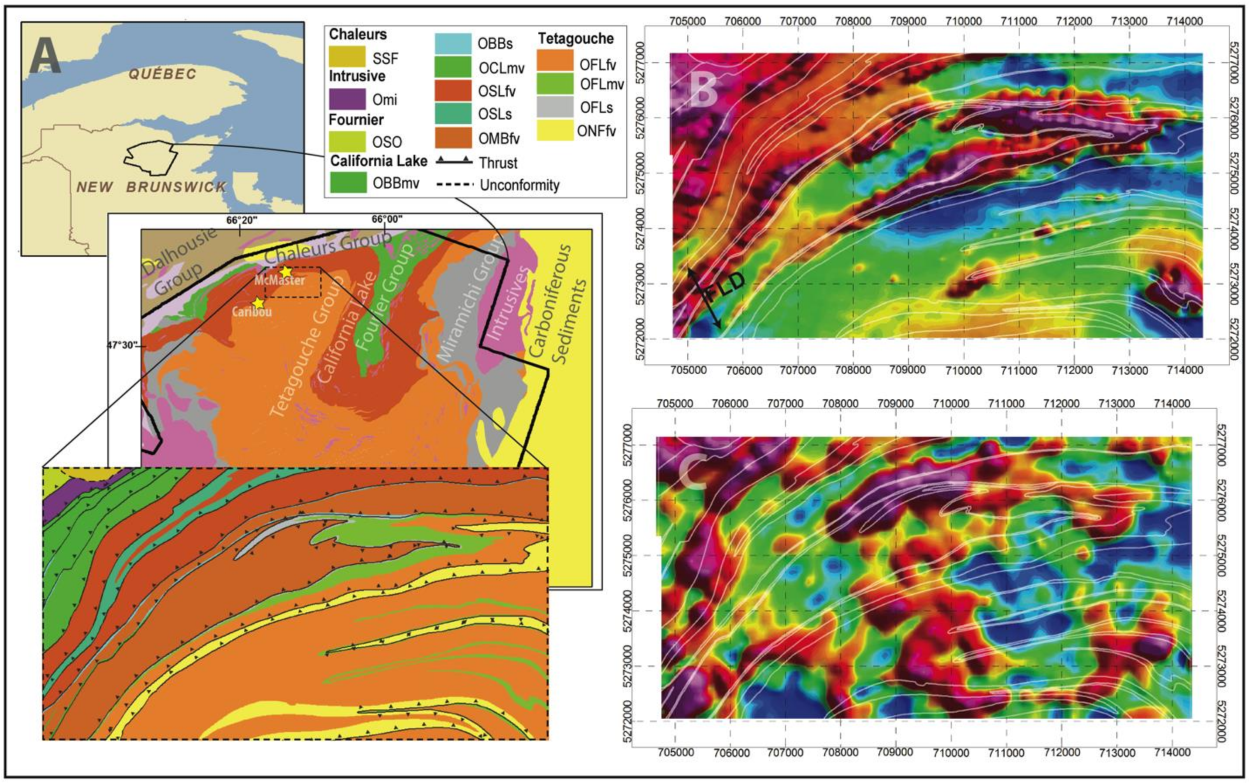

Figure 3-3: Geologic and geophysical data used for modeling. **(A)** Location and geologic map for the study area from GSC Open File 4128. **(B)** Total magnetic intensity map overlain by geology contacts. **(C)** Mid frequency (4433 Hz) conductivity with geologic contacts overlain.

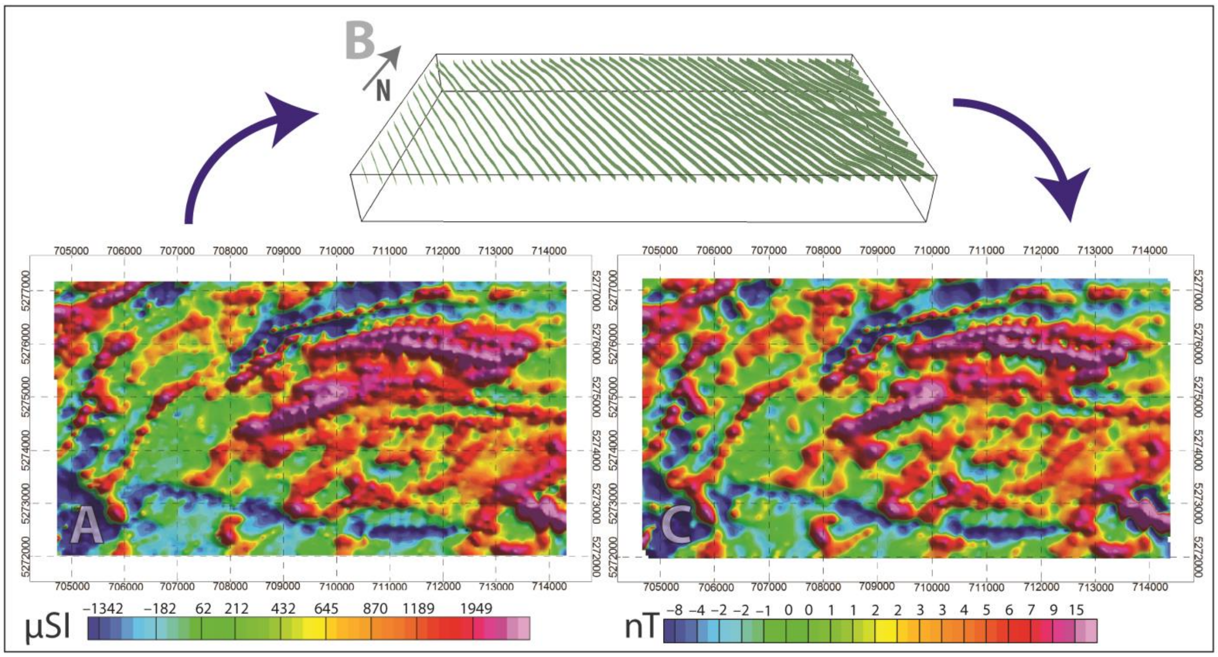

Figure 3-4: Modelling sequence **(A)** Inverted susceptibility from inphase frequency domain EM. **(B)** Forward model using 5m x 5m x 100m voxels under each fiducial in the survey database. **(C)** Calculated magnetic anomaly from model B.

laboratory measurements which have shown to range from 30 – 200 mS/m (Thomas et al., 1998). Felsic and mafic volcanic units through the area generally appear to be characterised by high resistivity values. Locally the presence of sulphides will produce high conductivity values which preclude any calculation of MS_{HFEM}.

In locations where the overburden is thick the HFEM signal may be dominated by the conductivity created by saturated clays present in the overburden. Keating et al., (1998) attempted to address the influence of overburden thickness and compositional variations on the computed conductivity signal by comparing the response from the vertical derivative of the magnetic field (1VD) with the conductivity response. The thesis employed by Keating et al., (1998) was that where a correlation exists between the two responses then there is minimal overburden coverage. This approach assumes a uniform distribution of magnetic properties within the overburden. For the study area there is very poor correlation between 1VD and conductivity. Overall surficial features do not correlate with conductivity so overburden effects should not pollute the calculated EM susceptibility.

Results

To gauge the accuracy of the derived MS_{HFEM} we compare the computed results for 25 sites with actual susceptibility values (MS_{OBS}) obtained through in-situ field measurements (Figure 3-6). In four cases the EM inversion produced negative values which are rejected in the plot. Negative susceptibility values arise when the EM response is dominated by surficial conductivity fluctuations; for these areas the MS_{HFEM} values are meaningless. The 21 positive MS_{HFEM} values associated with in-situ susceptibility measurements reveal a linear trend line. MS_{OBS} tends to be slightly higher than the inverted value and spans a broader range. Discrepancies between the computed and observed susceptibility values may be explained by the measured susceptibility representing a single point source whereas the inverted value represents an average of an area limited by the grid resolution, in this case 50m x 50m. It is also possible that there might be a consistent bias in the EM signal response; this would be reflected by a systematic shift in the computed susceptibility signal.

The correlation between the modeled magnetic intensity signal derived from EM susceptibility inversion and the observed magnetic anomalies recorded by the cesium vapour magnetometer along individual survey profiles is excellent (Figure 3-5). In some cases the modeled magnetic anomaly appears to be sharper than the observed magnetic anomaly pattern. Remember the observed magnetic intensity signal records the summation of all magnetic sources. The magnetic anomaly computed by the HFEM approach represents only the near surface sources. It is quite possible that the difference between the observed and computed magnetic anomaly patterns arises because an observed anomaly could be the summation of a near surface and a separate buried magnetic body.

A comparison is made between the modeled residual magnetics and the results of three wavelength based regional / residual separation methods (Figure 3-7). In the recorded TMI there is a strong northwestern gradient caused by increasing mafic volcanic rock volumes approaching the Fournier Group (Figure 3-3). Ideally an effective magnetic residual should eliminate this gradient as it is absent in the HFEM modeled magnetics (TMI_{HFEM}). To a point upward continuation does a reasonable job at removing this source signal, after continuation of just 400m, but it also introduces a slight gradient in the south of the image. Upward continuation residuals using 800m and 1600m separations fail to effectively remove this gradient, becoming progressively worse as the upward continuation height level is increased. Polynomial detrending performs the worst of the three techniques presented. A 1^{st} order polynomial detrend hardly removes any gradient. The 2^{nd} and 3^{rd} order polynomials improve the residual but introduce gradients into the image. Non-linear filter (NLF) performs best in this example producing the flattest regional field. Using a 400m wavelength cut-off the gradient is completely removed from the northwestern corner and some linear trends in the southeastern corner begin to emerge. At this short wavelength, over filtering is an issue and corrugation is introduced in the northeastern corner. At 1200m the non-linear filter method fails to remove all of the regional gradient. The optimum filter length in 800 m. The regional gradient is removed without the introduction of corrugation to the data.

A more direct examination between the 800m NLF magnetic residual ($RTMI_{NLF800}$) against the TMI_{HFEM} allows for a comparison of how well this new method works in modeling the magnetic response as well as isolating near surface versus deeper magnetic sources in the magnetic residual grid (Figure 3-8). Prominent high frequency features such as the east-west trending magnetic highs (M1, M2) resulting from OFL-mafic volcanics in the upper half of the map appear distinct and correlate well between both datasets. This implies these sources must be near surface. The TMI_{HFEM} creates a sharper source body than $RTMI_{NFL800}$ which results from the faster fall-off rate of the electromagnetic field. Northeast trending highs associated with Boucher Brook and Canoe Landing Lake mafic volcanics (M3, M4) are also well recovered. In the TMI_{HFEM}, M3 extends further to the northeast and wraps eastward while in $RTMI_{NLF800}$ this same anomaly has been truncated prior to the large central magnetic bodies.

Though overall there is good correlation between datasets in some locations discrepancies exist. In $RTMI_{NLF800}$ the M3 mafic volcanic bed obviously continues south through C1, and is mapped as such in the geologic map, however in MS_{HFEM} and TMI_{HFEM} a large low exists. Referencing back to the original EM dataset (Figure 3-3C) near C1 there exists a large conductive anomaly which prevents any meaningful susceptibility from being calculated for this location. A second discrepancy is the linear trending C2 feature obvious in MS_{HFEM} and TMI_{HFEM} but completely absent from the measured. Though not completely obvious in Figure 3-3C, the

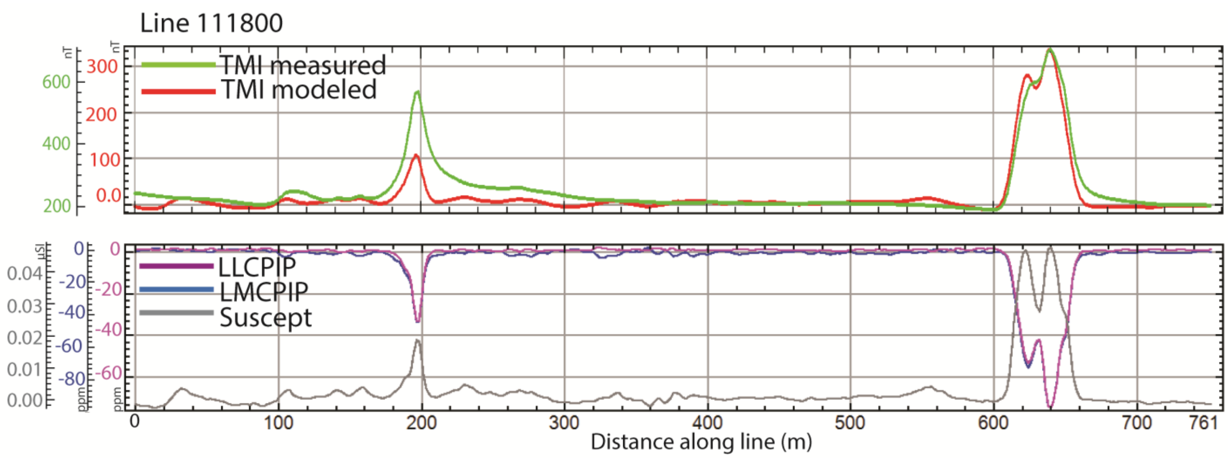

Figure 3-5: Profile along flight-line 111800. There is good correlation between measured and modeled magnetic anomalies (Top) where susceptibility is successfully recovered from low (LLCPIP) and medium (LMCPIP) coplanar inphase data (Bottom).

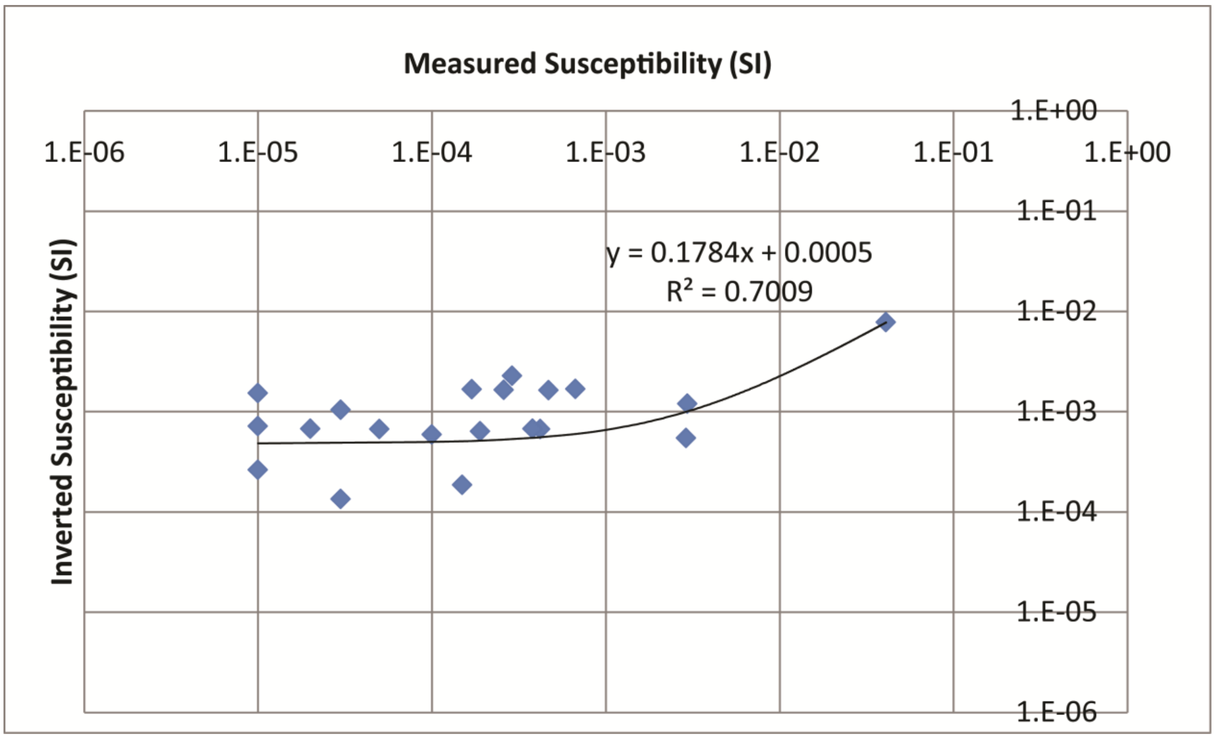

Figure 3-6: Measured susceptibility against inverted susceptibility. Negative values for inverted susceptibility (n = 4) and corresponding field measurements have been removed.

feature actually corresponds to a 2-lane highway running through the study area. Improper correction of this feature in the original EM dataset has been enhanced during the susceptibility inversion and again in the magnetic model; without due diligence the feature could easily be misinterpreted as something of geologic significance. In the south of the study area $RTMI_{NLF800}$ leaves some regional gradient which is absent from TMI_{HFEM}. At R1 there is still some subtle long wavelength content, however given that the total gradient is < 10 nT, it is less than all other residuals tested and is negligible.

A particularly strange bulls-eye anomaly (M5), has a geometry that is inconsistent with any other. Visual inspection suggests it may have a component of remanence because the magnetic field interacts to produce small lows both northwest and south of the main positive anomaly. The modeled magnetics does an excellent job at defining the geometry of the source in comparison to the residual magnetics which suffers from the same problem as the total field data. The RTP transformation performed prior to separation assumes purely inducing magnetisation so this is entirely expected of a remanent source, while the susceptibility inversion is independent of magnetic direction.

The possibility that there exists an anomaly which is remanently magnetised is supported by the observation that remanence has been observed at sulphide deposits through the camp (Thomas et al., 2000, Morris et al., 2008). It also allows us to test the effectiveness of this method at detecting and mapping the spatial extent of remanently magnetized source bodies. To do so we compare apparent susceptibly calculated on the TMI data against values obtained by the EM susceptibility inversion at each grid cell location (Figure 3-9). The standard "apparent susceptibility" filter algorithm assumes that all magnetisation is induced; that there is no remanence. The first observation is that there is good correlation between values. The vast majority cluster between -5,000 – 0 on the X-axis and 0 – 10,000 on the Y-axis, with a linear negative trend to high apparent susceptibility – low inverted susceptibility (T1). There may be a DC shift between datasets, accounting for the difference. But the most significant finding is a distinct second population of high MS_{HFEM} and low MS_{TMI} (T2). When examined in map view 91 % of these values plot directly over the M5 anomaly. The cross-plot indicates that the calculated susceptibility values are systematically higher than the spatially equivalent MS_{OBS} values. This observation is compatible with M5 having a component of reverse polarity (negative inclination) remanent magnetisation. As demonstrated in Figure 3-2 a negatively inclined remanence component, even if it is not aligned parallel to the Present Earth's Field direction will produce an decrease in the observed total magnetic field. A positively inclined remanence, even if it is of equivalent strength to the induced field will produce an apparent increase in overall total magnetic field (Figure 3-2). By comparing an apparent susceptibility transform to inverted susceptibility, it is possible one may discriminate remanently magnetized sources.

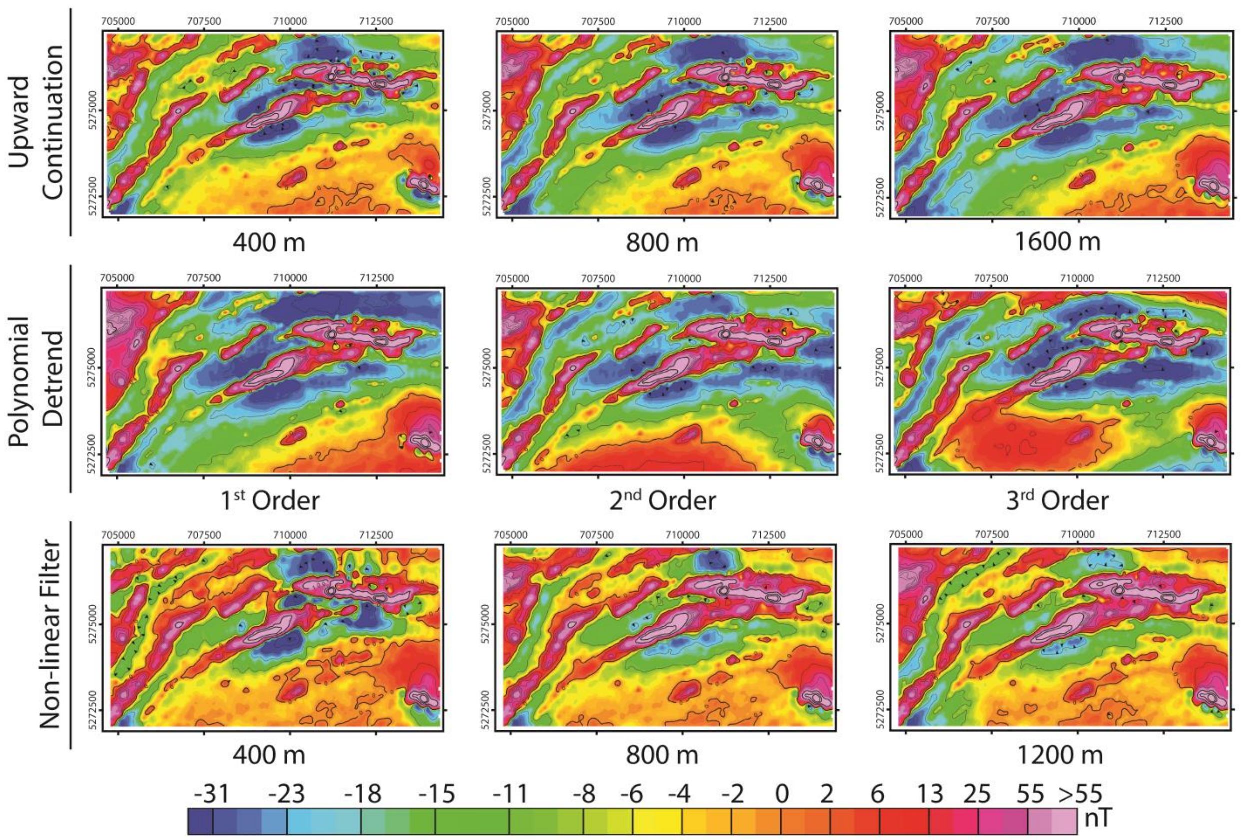

Figure 3-7: Comparison between magnetic residuals calculated using different methodologies. Colour zonation is equivalent and restricted between -40 nT to 660 nT in all maps. Thick black contour lines represent 100 nT isograms, thin black lines represent 10 nT isograms.

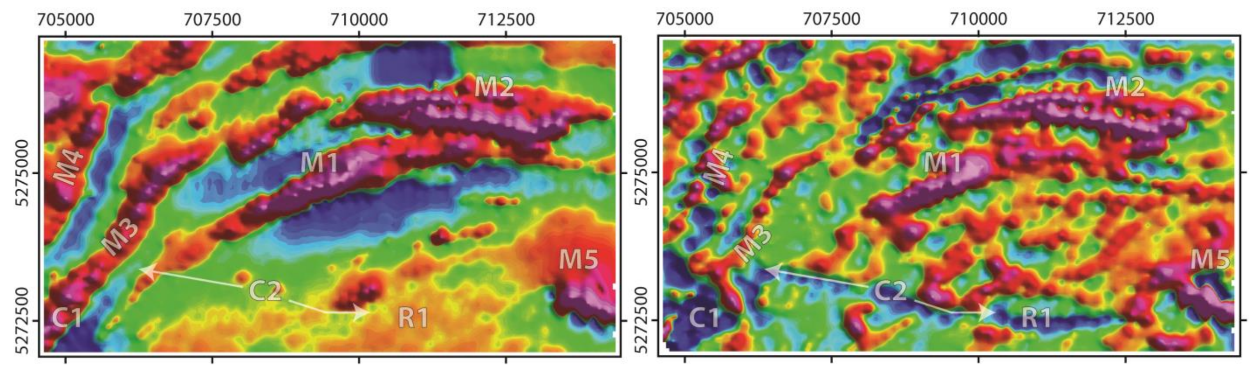

Figure 3-8: Comparison between measured and modeled magnetic anomalies. (Left) Residual magnetic anomaly from an 800m non-linear filter. (Right) Magnetic anomaly map from forward susceptibility model. See text for annotations.

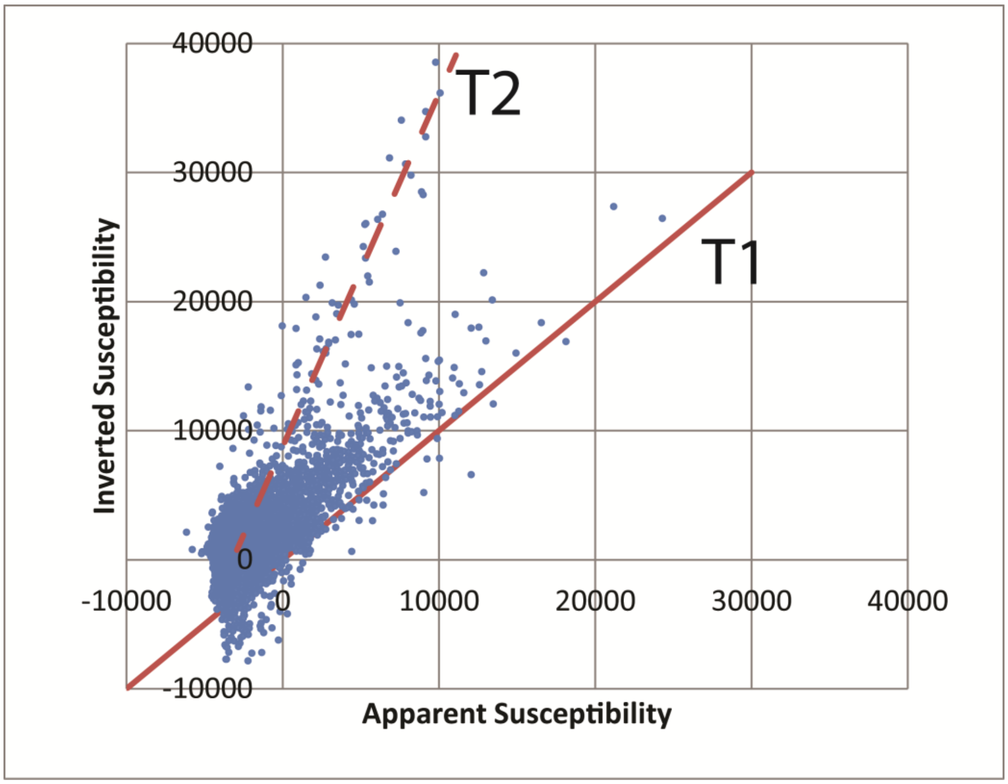

Figure 3-9: Apparent susceptibility calculated from magnetics plotted against values from inverted susceptibility at all grid cell locations in the study area.

Discussion

Overall there is good correlation between the observed and modeled magnetic datasets. Features which must be near-surface because they are defined by the depth-limited HFEM can be identified in both of the data sets. As such calculation of a model TMI signal provides an effective method for separating near surface and deep, or buried magnetic sources. Though the method is generally successful in the example shown, there are some issues and limitations that need to be addressed. As noted above, inversion of the HFEM data provides an estimate of "relative permeability" which in turn leads to an apparent susceptibility value. A comparison between the computed and observed susceptibility values suggest that there is a clear linear relationship between the two values. However, it must be remembered that variables within HFEM inversion means that the computed MS_{HFEM} cannot give absolute estimates of susceptibility. Systematic shifts in the computed susceptibility value could easily be addressed by an iterative comparison of the computed near surface TMI signal and the actual observed signal. Since any systematic shift in susceptibility would provide an equivalent systematic shift in the computed TMI, an optimum near surface magnetic source distribution could be calculated by iteratively seeking the optimum match between the computed and observed magnetic signal.

The EM inversion model used in this study makes a number of assumptions; first it assumes a uniform depth of penetration for the HFEM sensors across the study area; and second it assumes that the near surface layer can be approximated by a single layer with uniform electrical properties. When examined in detail neither of these two assumptions are fully valid. For example, any lateral change in conductivity would modify the actual depth penetration of the EM signal: lower depth penetration in more conductive zones might result in reduced susceptibility values and vice versa. For this study area overburden effects are minimal. This may not be the general case. When a layered earth is present then a more complex inversion model must be adopted. Zhang and Oldenburg (1997, 1999) for example describe a procedure for extracting a layered earth model for susceptibility and conductivity data from electromagnetic data. An important aspect of this multi-layer approach is having access to frequency domain electromagnetic data which records a signal at a number of different EM frequencies.

Geological dip is also an issue. Currently all of the bodies are modeled as a series of right rectangular vertical prisms, a geometric assumption geologically incorrect in many deformed environments. As such, the true magnetic anomaly may reflect the dip of the source body whereas the modeled field will not. Introducing a dip to the model based on field measurements would be a simple way to overcome this. However, having established the effective susceptibility of a specific stratigraphic horizon one could then use that information along with contact points in a forward modeling exercise on a series of profiles perpendicular strike to derive estimates of local dip.

Anthropogenic sources can also be a major problem. In our example a highway creates an artificial low, which without satellite imagery, could be misinterpreted as a geologic feature such as a fault. In other cases, such as if a power line was present it is unlikely any susceptibility could be solved because the technique fundamentally suffers the same issues EM systems experience in developed regions. Another major problem is conductive earth sources. Essentially wherever conductive anomalies exist the inversion fails to provide a meaningful susceptibility and consequently no real magnetic anomaly can be modeled. This finding is however unsurprising and has long been recognized (Huang and Fraser, 2000) because the effects of conductive currents overshadow any effect of susceptibility in the in-phase component.

Conclusion

Herein we have presented a method of forward modeling magnetic field anomalies using apparent susceptibility data derived from frequency domain electromagnetic data and discussed its application to regional / residual separation of magnetic data and the detection of remanently magnetized source bodies. In-phase coplanar frequency domain electromagnetic data is inverted for susceptibility based on the principles described by Huang and Fraser (2000), Huang and Fraser (2001). A calculated TMI signal is then modeled as a series of right sided vertical prisms with homogenous EM based susceptibility which is subjected to a synthetic magnetic field. The resultant magnetic anomalies are recorded into the database for gridding. All flight characteristics and sampling rates are ubiquitous across datasets.

Overall there is excellent correlation between the recorded and modeled magnetic anomalies. Most of the large high amplitude anomalies are recorded in both datasets, with the modeled data locally having a sharper resolution than the measured set. Cross examination between a number of different wavelength based residual magnetic grids and the modeled magnetics residual grid shows that the proposed method produces results comparable to those generated by the NLF approach recently proposed by Keating and Pinet (2011). An obvious advantage of this HFEM based approach is that it automatically permits the wavelength of the source signal to vary across the study area. To achieve the same outcome with the NLF approach one would need to compute multiple passes of the filter with differing filter pass wavelengths. Where long wavelength anomalies persist in a residual magnetic grid but are absent from the forward modeled residual solution, it is likely an improper residual was achieved. An additional benefit of the HFEM approach is that the computed MS_{HFEM} values could be used as an input constraint in a modeling exercise which attempted to resolve local geological dips using discrete object modeling approach (Jessell, 2001).

A comparison of MS_{HFEM} and MS_{TMI} provides a method for rapidly locating the presence of remanently magnetised source bodies. The magnitude of MS_{TMI} to the MS_{HFEM} provides a direct indication of the polarity of the remanent magnetic signal: a positively inclined remanence will produce an increased apparent susceptibility; a negatively inclined remanence will produce a reduced apparent susceptibility. Knowing the EM susceptibility of a remanently magnetised source body will help when attempting to constrain the geometry of the remanence vector through inversion modeling.

Problems which affect EM recording systems, such as anthropogenic sources, can influence the inverted susceptibility and intern modeled magnetics. As well, conductive bodies impair the susceptibility inversion from deriving any meaningful results also prevent any meaningful magnetic anomaly from being modeled. Currently the methodology invokes vertical right sided prisms at a number of points in the computation. No attempt is made to derive any structural dip information. In this study we assumed a uniform effective source depth for all modeled bodies though it is possible that the depth extent might vary across a project area. This would produce minor fluctuations in the computed susceptibility values.

References

de Roo, J., A. and van Staal, C. R., 1994. Transpression and extensional collapse: Steep belts and flat belts in the Appalachian Central Mobile Belt, northern New Brunswick, Canada. Geological Society of America Bulletin, **106**, 541 - 552

Fedi, F. and Quarta, T., 1998. Wavelet analysis for the regional-residual and local separation of potential field anomalies. Geophysical Prospecting, **46**, 507 – 525.

Fraser, D.C., 1981. Magnetite mapping with a multi-coil airborne electromagnetic system. Geophysics, **46**, 1579 – 1593.

Gupta, V.K., Grant, F.S., and Card, K.D., 1984. Gravity and magnetic characteristics of the Sudbury Structure. p.381-410. *In* The geology and Ore deposits of the Sudbury Structure, edited by E.G. Pye, A.J. Naldrett, and P.E., Giblin, Ontario Geological Survey, Special Volume 1, 606 pp.

Hearst, R.B., and Morris, W.A., 2001. Regional gravity setting of the Sudbury Structure. Geophysics, **66**, 1680-1690.

Hodges, G., 2004. Mapping conductivity, magnetic susceptibility, and dielectric permittivity with helicopter electromagnetic data 74th Annual Meeting, SEG, Extended Abstract, 660 - 663.

Huang, H. and Fraser, D.C., 2000. Airborne resistivity and susceptibility mapping in magnetically polarizable areas. Geophysics, **65**, 502 – 511.

Huang, H. and Fraser, D.C., 2001. Mapping of resistivity, susceptibility, and permittivity of the earth using a helicopter-borne electromagnetic system. Geophysics, **66**, 148 – 157.

Jessell, M., 2001. Three-dimensional geological modelling of potential field data. Computers & Geosciences, **27**, 455-465.

Keating, P., Kiss, F.G., Katsube, J., Best, M.E., 1998. Airborne conductivity mapping of the Bathurst mining camp. Exploration Geophysics, **29**, 211 – 217.

Keating, P., Thomas, M.D., and Kiss, F.G., 2003. Significance of a high resolution magnetic and electromagnetic survey for exploration and geologic investigation, Bathurst Mining Camp, *In* Massive Sulfide Deposits of the Bathurst Mining Camp, New Brunswick, and Northern Maine. *Edited by* W.D., Goodfellow, S.R., McCutcheon, and J.M., Peter. Economic Geology Monograph 11, 783-798.

Keating, P., and Pinet, N., 2011. Use of non-linear filtering for the regional–residual separation of potential field data. Journal of Applied Geophysics, **73**, 315 – 322.

Keating, P., Pinet, N., and Pilkington, M., 2011, Comparison of some commonly used regional residual separation techniques. Proceedings of International Workshop on Gravity, Electrical & Magnetic Methods and their Application, 73–76.

Li, Y., and Oldenburg, D. W., 1998. Separation of regional and residual magnetic field data. Geophysics, **63**, 431 – 439.

McCutcheon, S.R., Luff, W.M., Boyle, R.W., 2003. The Bathurst Mining Camp, New Brunswick, Canada: History of Discovery and Evolution of Geologic Models. *In* Massive Sulfide Deposits of the Bathurst Mining Camp, New Brunswick, and Northern Maine. *Edited by* W.D., Goodfellow, S.R., McCutcheon, and J.M., Peter. Economic Geology Monograph 11, 17 - 35.

McGrath, P.H., and Broome, H.J., 1994. A gravity model for the Sudbury Structure along the Lithoprobe seismic line. Geophysical Research Letters, **21**, 955-958.

Morris, W.A., Ugalde, H., Mwenifumbo, J., 2008. Borehole magnetics navigation. An example from the Stratmat Deposit, Bathurst, New Brunswick. The Leading Edge, **27**, 1106 – 111.

Mwenifumbo, C.J., Elliot, B.E., and Street, P., 2003. Borehole geophysical characteristics of massive sulfide deposits in the Bathurst Mining Camp. *In* Massive Sulfide Deposits of the Bathurst Mining Camp, New Brunswick, and Northern Maine. *Edited by* W.D., Goodfellow, S.R., McCutcheon, and J.M., Peter. Economic Geology Monograph 11, 841-860.

Nettleton, L.L., 1954. Regionals, residual, and structures. Geophysics, **19**, 1 – 22.

Roach, M.J., Leaman, D.E., Richardson, R.G., 1993. A comparison of regional – residual separation techniques for gravity surveys. Exploration Geophysics, **24**, 779 – 784.

Spector, A. and Grant, F.S., 1970. Statistical models for interpreting aeromagnetic data. Geophysics, **35**, 293 – 302.

Thomas, M.D., Walker, J.A., Keating, P., Shives, R., Kiss, F., and Goodfellow, W.D., 2000. Geophysical atlas of massive sulphide signatures, Bathurst mining camp, New Brunswick. Geological Survey of Canada, Open File 3887; and New Brunswick Department of Natural Resources and Energy; Minerals and Energy Division, Open File 2000-4, 105 p.

Tschirhart, P., 2013. Geophysical processing and interpretation with geologic controls: Examples from the Bathurst Mining Camp, New Brunswick. Unpublished M.Sc Thesis. McMaster University, Hamilton ON.

van Staal, C.R., Wilson, R.A., Rogers, N., Fyffe, L.R., Langton, J.P., McCutcheon, S.R., McNicoll, V., and Ravenhurst, C.E., 2003. Geologic and tectonic history of the Bathurst Supergroup, Bathurst Mining Camp, and its relationship to coeval rocks in Southwestern New Brunswick and adjacent

Maine - A synthesis. *In* Massive Sulfide Deposits of the Bathurst Mining Camp, New Brunswick, and Northern Maine. *Edited by* W.D., Goodfellow, S.R., McCutcheon, and J.M., Peter. Economic Geology Monograph 11, 37-60.

Zhang, Z., and Oldenburg, D., 1997. Recovering magnetic susceptibility from electromagnetic data over a 1-D earth. Geophys. J. Internat., **130**, 422-434..

Zhang, Z., and Oldenburg, D., 1999. Simultaneous reconstruction of 1-D susceptibility and conductivity from electromagnetic data. Geophysics, **64**, 33-47.

Chapter Four: Applying laterally varying density corrections for ground gravity and airborne gradiometry data and comparison of frequency content. A case study from the Bathurst Mining Camp

[1]Peter Tschirhart, [1]Bill Morris, [2]John Mims

[1] *MAGGIC, SGES, McMaster University, Hamilton ON, L8S 4K1*
[2]*Bell Geospace, Houston TX*

Abstract

The influence of topography on gravity and gravity gradiometry measurements is profound and must be removed prior to interpretation. For gravity data the effect of topography is minimized through the computation of Bouguer and terrain corrections while for airborne gradiometry only the terrain correction is applied. In almost all cases an average density value is used in both correction algorithms. However, in geologic environments where there is a structural and/or stratigraphic control on the near surface mass distribution, using a single density value may introduce error into the reduced data. A regionally variable density correction is a means to compensate for this effect and though the concept has been around for over 50 years, there are few studies which implement this technique. In this paper we demonstrate how to apply a spatially variable density correction using ground gravity and airborne gravity gradiometry data for the geologically complex Bathurst Mining Camp, northern New Brunswick, Canada. Ground gravity and airborne full tensor gravity gradiometry (AGG) measurements are sub-divided into a series of separate zones based on the underlying tectono-stratigraphic group. Terrain and Bouguer corrections are calculated for each area using representative density values obtained from drill-core and surface sampling throughout the Camp. The new spatially variable density correction factor is applied and compared with previous maps. Overall, the differences are subtle, but the spatially variably density allows for isolated anomalies to be better resolved. Examining the relationship of topographic fluctuations to terrain related artifacts within the AGG data serves to validate the density values used in the terrain correction algorithm. The information content of the ground gravity and AGG transformed into vertical gravity is also compared for semblance. Spectral information is comparable especially at longer wavelengths. Differences in spectral content of the two data sets arise from the irregular sparse sampling of ground data which through minimum curvature gridding introduces false peaks uncorrelatable to the regularly sampled AGG data. The AGG is also systematically more sensitive to higher frequency content at wavelengths less than 6 km.

Introduction

In its most basic form the Bouguer anomaly is the difference between the observed gravity at a location and the complete earth model. That is, the Bouguer anomaly is the measured gravity at a location X, Y, Z on the earth's surface minus all non-geologic effects (Chapin, 1996, LaFehr, 1991). Accurate computation of a Bouguer anomaly map for an area should therefore provide a direct representation of geological variations manifesting in terms of lateral and vertical density variations.

To convert raw gravity observations to Bouguer data a series of corrections are required. There are, however, two quite distinct types of corrections. Tide, latitude and free air corrections are easily computed through the use of well-established formula and reference tables. Input for these corrections primarily requires only accurate location and elevation information. To complete the transformation from Free Air gravity to Bouguer gravity, the next set of corrections requires the operator to apply two additional adjustments, the Bouguer Slab and terrain corrections. Both of these corrections address the geometry and mass of the material between the location of the observation point and the geoid reference surface. Again both corrections necessitate detailed topographic and location data, but in addition these corrections require the operator to provide an average density value which is considered representative of the Bouguer slab. In many cases the average density value used in these corrections is 2.67 g/cm^3, a value believed to represent the average density of crystalline, continental crust of granitic composition (Hinze, 2003). Many areas favorable for mineral exploration are however, more commonly associated with either metamorphic or include amalgamated slabs of oceanic crust; both of these terrane types have densities higher than continental crust. In such situations it is inappropriate to correct the Bouguer slab using the lower 2.67 g/cm^3 value. Instead, the Bouguer slab and terrain corrections are reduced using a regional average density value estimated from a suite of field density measurements. Such an approach is appropriate for small scale surveys where the relative variation between units is low. Regional surveys, however, may encounter significant density differences associated with broad scale lithological composition variations. In many orogenic zones it is possible to witness the juxtaposition of terranes having average density values through some degree of tectonic or structural control or magmatism. Applying an average regional density value to the Bouguer slab corrections for the whole area will, depending on the density of the individual terrane, result in either over- or under-correcting the data, introducing some amount of error into the final solution (Singh et al., 2006, Vajk, 1956).

Vajk (1956) was the first to propose the idea of using laterally variable density values to correct the Bouguer slab. Fundamentally a variable density should be applied only to the lowest point in the topographic surface, and below that point down to sea level, a constant density value should be used in order to reduce error (Figure 4-1) (Vajk, 1956). This simple procedure avoids geologically dependent topographic features such as faults or fold belts where the near surface relief is controlled by different geologic formations. There are few examples of this methodology within the literature. In a more recent example, Singh et al. (2006) applies this methodology to ground gravity (GG) data acquired in the geologically complex Frontier Area of Pakistan. True density values from borehole and field sampling were used and a Bouguer correction to the lowest topographic point was applied. As suggested by the author, this methodology can improve the interpretation for local structures of exploration interest by eliminating errors on the order of several mGal which were introduced by using a regional average density rather than a rock unit specific value (Singh et al., 2006).

Airborne gravity gradiometry (AGG) systems have a Bouguer slab value of zero. However, critical to producing any AGG component anomaly map is developing an accurate terrain correction (Chen and Macnae, 1997). The dominant signal in any AGG system survey data set is the near surface density distribution. The air-ground interface presents the largest density contrast and is only after the terrain signal has been minimized that the anomalous gravity gradient field becomes apparent. It is well documented that using elevation data with incorrect spatial resolution and employing inappropriate density values for the near surface sources produces artifacts that directly reflect the topography in any resulting gravity gradient data set. This in turn, can impact the density models derived from subsequent inversion routines (Dransfield, 2007, Kass and Li, 2008, Fullagar and Pears, 2010, Li et al., 2010). In an oil exploration setting Houghton et al., (2007) show how traditional average density methods in terrain reductions will not properly accommodate variations in high resolution surveys. If the terrain correction is not properly applied then terrain related artifacts will be carried over into the final map where they can be mistaken for real geologic signal. In a mineral exploration setting especially for a large survey area with a wide variation in density and/or a structural control on the near surface lithological distribution it is possible for the terrain signal to corrupt the geological signal.

In this case study, based in the Bathurst Mining Camp (BMC), New Brunswick (Figure 4-2) we demonstrate how using a variable density approach to Bouguer slab and terrain corrections can produce an improved Bouguer anomaly map product which contains a significant reduction in the number of topography related artifacts in a mineral exploration setting. We describe a methodology for subdividing the region into a series of uniform density zones based on prior geological mapping. We compute variable density terrain images for both ground based gravity and airborne gravity gradiometry data using average density values based on drill core and surface sample measured density values. We demonstrate how with airborne gravity gradiometry and topographic data it is possible to independently verify the observed density values. Finally, through a comparison of the airborne gravity gradiometry and the

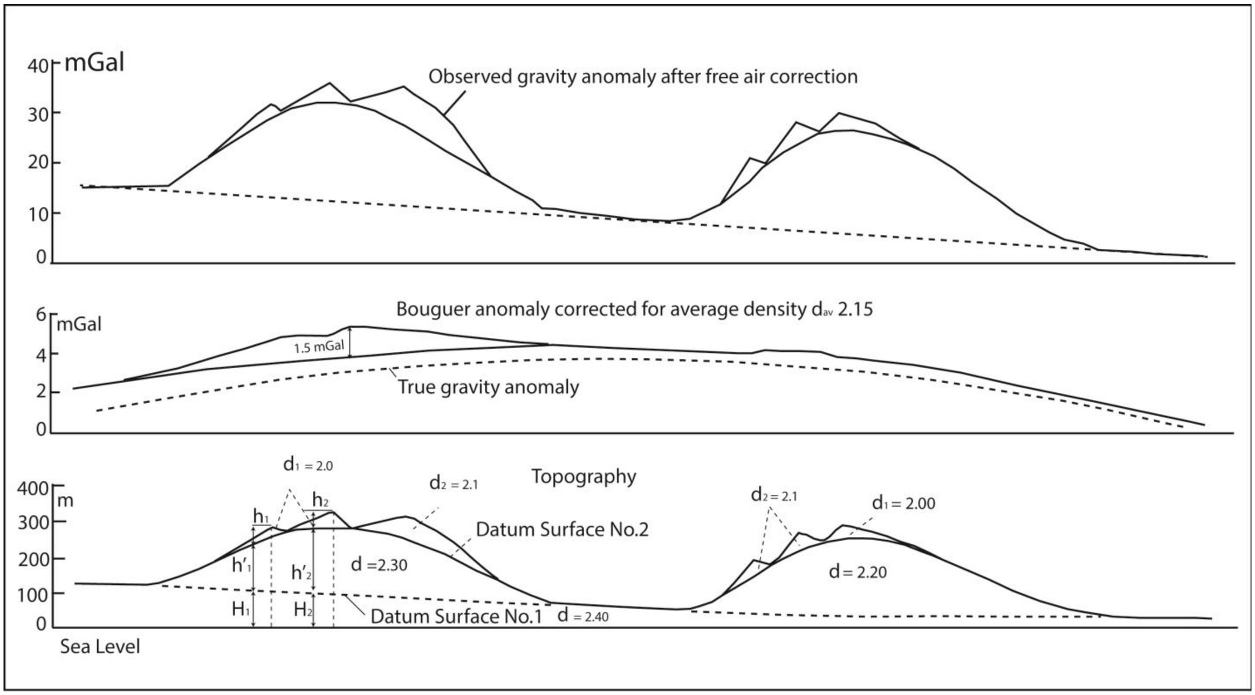

Figure 4-1: Errors induced by improperly correcting gravity data with an average value (from Vajk, 1956). When an average density is used instead of actually densities for topographic features, erroneous anomalies may be obtained. A constant density value should be applied to the primary datum (lowest elevation point down to sea level, H) while variable densities should be applied to topographic relief (secondary datum h') and individual topographic highs (h).

ground gravity data, we show the benefits afforded by the uniform station sampling provided by the airborne survey.

Study Area

The Bathurst Mining Camp, located in northern New Brunswick, Canada (Figure 4-2) represents a relatively well-preserved subduction complex which formed in response to the closure of the Tetagouche-Exploits back-arc basin, analogous to the modern Japan-Sea, through the mid to late Ordovician (van Staal et al., 2003a). Five major tectono - stratigraphic groups (California Lake, Tetagouche, Fournier, Sheephouse Brook and Miramichi Groups) present in the study area were structurally juxtaposed to each other by a series of imbricated thrust faults. Each group has unique sedimentary or volcano-stratigraphic successions which formed in widely separated ensialic to ensimatic back-arc basin environments prior to subduction. Facies developed from felsic to mafic volcanic rocks with concurrent sedimentary rock types (van Staal et al., 2003a). Multiple phases of felsic through mafic intrusions were emplaced throughout the BMC during Ordovician, Silurian and Devonian times. Sedimentary cover sequences including the Silurian Chaleur and Kingsclear Groups, Devonian Dalhousie Group and Carboniferous Clifton Formation occupy the edges of the BMC map region. Tectono- stratigraphic groups are listed in Table 4-1.

Survey Data

Effective exploration with ground gravity has cumulated with over 5000 stations through the BMC (Figure 4-2). Government surveys (Morris et al., 2007) and legacy data compilations (Thomas et al., 2008) have made all stations publically available at Natural Resources Canada's Geoscience Data Repository (http://gdr.agg.nrcan.gc.ca). Station spacing varies considerably through the Camp from less than 50 m along individual lines over deposits to just less than 3 km around the fringes of the camp. Camp wide nominal station separation is 477 m.

Full tensor airborne gravity gradiometry data comes from a 2004 Bell Geospace survey flown for Noranda (now Xstrata Zinc Canada), Slam Exploration, and the Government of New Brunswick (Figure 4-2). Survey specifications follow a gentle drape surface with minimum terrain clearance of 80 m. Flight lines and tie lines are 200 m and 2000 m respectively. Original 2004 survey data was reprocessed in 2008 and 2010 using new processing algorithms to minimize high levels of noise recorded in this very early FTG dataset. The 2010 algorithms use full tensor noise reduction (Mims et al., 2012) to remove non-systematic noise and enhance tensor components. Originally the data was corrected using incremental terrain corrections ranging from 2.40g/cm^3 to 3.00g/cm^3.

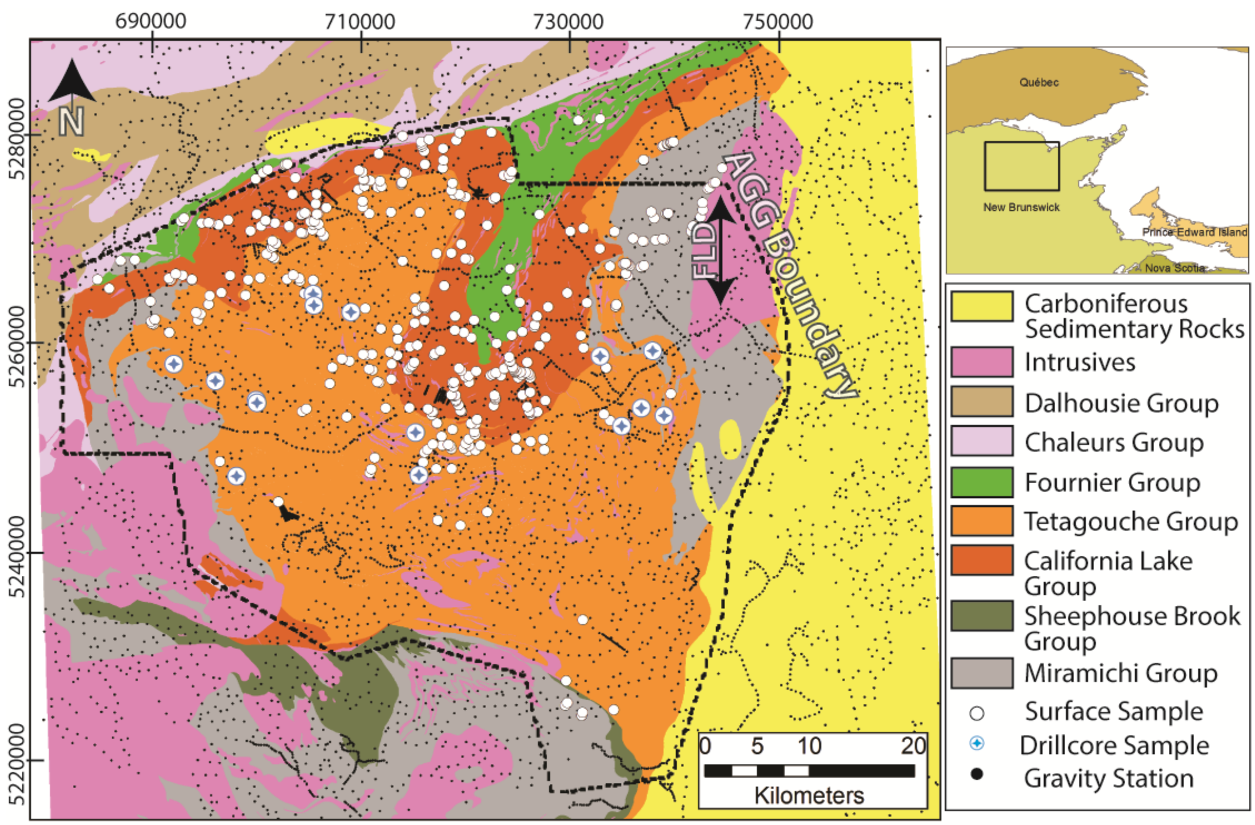

Figure 4-2: Geologic map of major stratigraphic groups in the Bathurst Mining Camp (edited from van Stall et al., 2003, Open File 4182). Locations of drillholes and surface samples used for the study are identified. Locations of ground gravity stations identified and Bell FTG survey limits delineated. FLD = Flight line direction, AGG = Airborne gravity gradiometry.

Method

Initially, a comprehensive rock property database is constructed from over 1,000 surface and drill core samples encompassing all geologic groups in the BMC (Figure 4-2). Density values are determined using the methodology prescribed in Smith et al., (2012). Average density values are then determined for each rock type: gabbro, rhyolite, siltstone etc., using information provided by geological logs. Most strata in Bathurst Mining Camp have a near vertical dip. A weighting scheme is devised based on the relative abundance of each rock type within a particular tectono-stratigraphic group as mapped by van Staal et al., (2003b) to compute an average density value that would be representative of each tectono-stratigraphic group.

Ground gravity stations are then windowed by the same geologic contacts as the major tectono-stratigraphic groups and reprocessed to the complete Bouguer anomaly (terrain corrected) using the new density values listed in Table 4-1. All of the processing parameters except the Bouguer and terrain corrections are identical to those used in the original dataset (Morris et al., 2007). Finally the separate databases are merged together and re-gridded to create the variable density (VD) complete Bouguer anomaly map (Figure 4-3).

AGG corrections require a grid of density variations to calculate the topographic response. For this study two variable density terrain correction grids were created to reprocess the AGG data using a similar methodology. An initial variable density terrain correction grid was generated by windowing the data to the tectono – stratigraphic contacts, assigning the correction density value listed in Table 4-1 to the appropriate region, merging the separate databases and gridding. One correction grid was produced using a minimum curvature algorithm with a 400 m low pass filter to emphasize a smooth correction between contacts (Figure 4-4). A second VD correction grid was also generated using the same data inputs but this one was developed employing a tinning algorithm for gridding in place of the minimum curvature routine. The tinning algorithm forces a sharp density contrast, and therefore correction factor, across group contacts. The terrain correction grids are then applied to the data and full tensor noise reduction (FTNR) is applied. FTNR enhances the tensor components by assuming an independent tensor response may be estimated from the remaining components to identify and remove non-Laplacian signal (Mims et al., 2012). After FTNR it was found that little difference exists in output between the different terrain correction grids and only the minimum curvature correction grid is used within the proceeding discussion.

Finally, reprocessed GG and AGG datasets are analyzed to compare the geologic content recorded in both. Several additional processing steps were required to affect this comparison. Firstly, AGG – Gzz component must be transformed to vertical gravity (Gz) by means of a

Table 4-1: Density correction values

Stratigraphic Group	**Density (g/cm^3)**
Miramichi	2.75
Sheephouse Brook	2.81
Tetagouche	2.72
California Lake	2.82
Fournier	2.83
Kingsclear	2.75
Chaleurs	2.73
Dalhousie	2.72
Carboniferous sedimentary rock	2.73
Intrusives	2.75

vertical integration filter. Secondly, wavelength content from the ground gravity dataset, longer than those recorded by the AGG system, is removed for semblance. By survey design the maximum wavelength recorded in the ground dataset is half that of the total width, approximately 45 km. However given that the maximum dimension of the AGG survey is 68 km, the maximum wavelength recorded by the AGG system is 34 km. High frequency information recorded by the AGG system also must be removed. AGG data underwent low pass filtering during reprocessing to 400 m, but the 477 m nominal station spacing recorded in the GG data limits the smallest comparable anomaly to just under 1 km. An 8^{th} order Butterworth bandpass filter applied to both datasets restricts their frequency content between 1 km and 30 km. Finally, the different observation levels recorded in both surveys need to be matched. Ground gravity observations are made at ground level while the AGG survey recorded at a minimum of 80 m above the topographic surface. Both data sets are adjusted to a constant observation level of 250 m above the topographic surface using the Compudrape upward, downward continuation method. Datasets are then compared for correlation (Figure 4-5).

Results and Discussion

As should be expected, the result of the variable density Bouguer correction to the ground gravity is very similar to the original constant density Bouguer correction (Figure 4-3). The overall shapes and trends of the major anomalies is essentially unchanged by the reprocessing. However their exact extents and amplitudes are slightly altered. The major central gravity high, caused by the ophiolitic Fournier Group and mafic volcanics of the California Lake Group, is extended slightly to the east on the order of tens of meters and is reduced in amplitude by a maximum of 2.1 mGal. Along the Tetagouche – California Lake contact, a small isolated body of Tetagouche, Flat Landing Brook (FLB) mafic volcanics (encircled in Figure 4-3) sits against less dense California Lake, Mount Brittan felsic volcanics. The variable density correction does a superior job at isolating this anomaly from the more northerly California Lake – Canoe Landing Lake (CLL) mafic volcanics. Using a uniform density the signal associated with the FLB body is merged with that of the CLL sequence at a constant density. The improved imaging of this body is caused by a lower correction being applied to the Tetagouche Group block relative to the denser Fournier and California Lake Groups. As a result, isolated dense bodies in the Tetagouche Group block have a higher relative contrast while those in the Fournier and California Lake Groups are subdued in total amplitude by the higher correction value. A number of other subtle, but important differences can be seen in Figure 4-3 but for brevity will not be individually discussed here.

The simplest way to compare the two outputs is a difference computation (variable - constant) (Figure 4-3C). Cooler colours represent a higher correction and warmer lower. As evident, the primary difference is, of course, the varying Bouguer correction values applied to

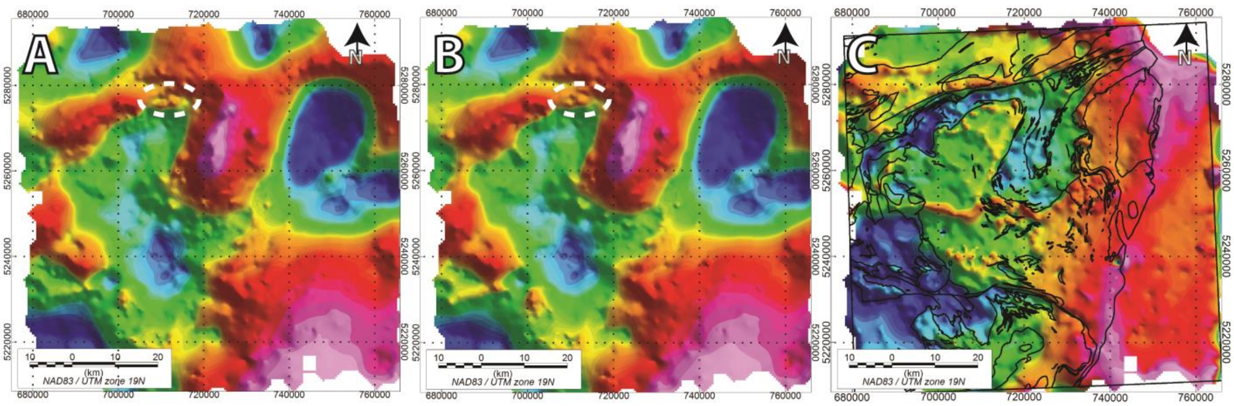

Figure 4--3: (A) Variable density complete Bouguer anomaly map of the Bathurst Mining Camp. **(B)** Constant density 2.67 g/cm^3 **(C)** Difference between constant density correction and variable density correction. Area encircled in A and B discussed in text. All three grids are gridded using a minimum curvature algorithm, cell size of 500m, and sunshaded from 45°.

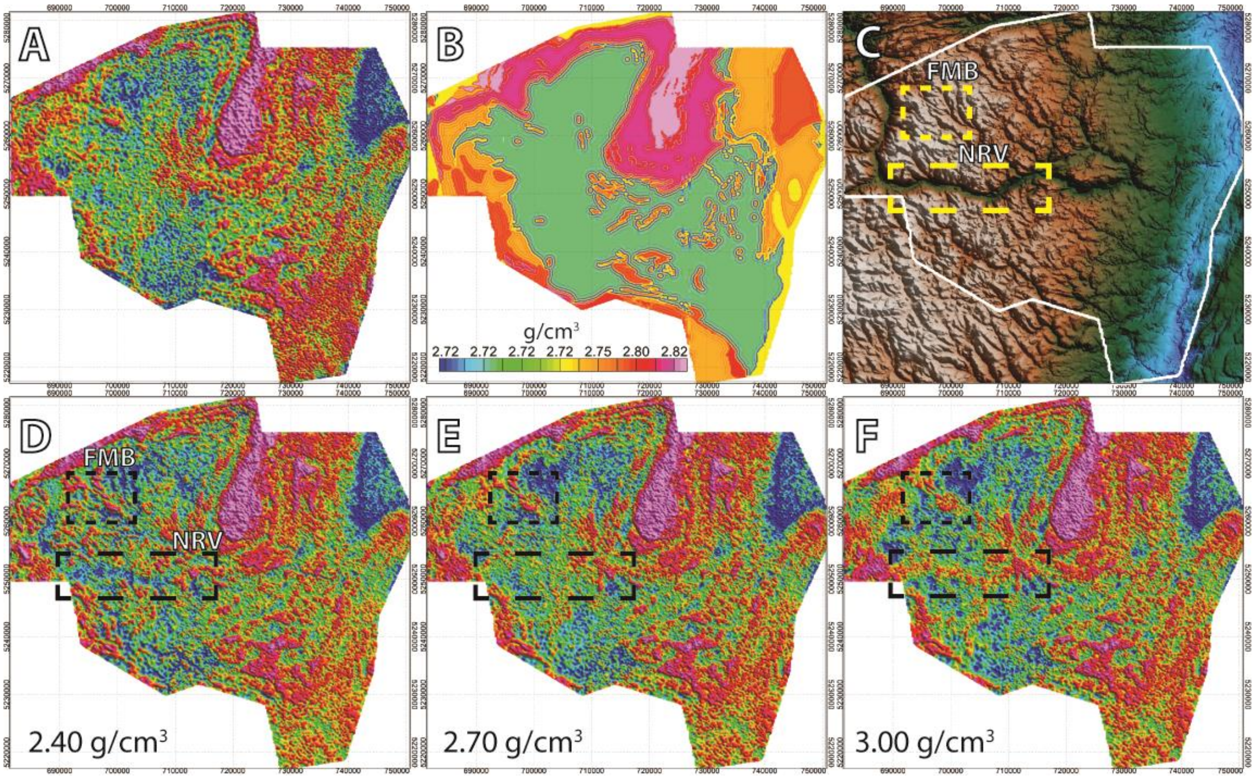

Figure 4-4: (A) Terrain corrected, variable density Gzz component. Corrected for using minimum terrain correction grid and FTNR, 400 m cutoff was applied to remove high frequency noise. **(B)** Terrain correction grid using the minimum curvature algorithm. 400 m low pass filter applied to reduce ringing and smooth transition between contacts. **(C)** Canadian digital elevation database of survey and surrounding area. **(D, E, F)** Terrain corrected, constant density Gzz component using values listed in image. Boxes identify areas of considerable difference between grids. Grids A, B, D, E, F are gridded to 50 m using a minimum curvature algorithm. Grids A, C, D, E, F are sun shaded at 45° inclination and 45° declination. FMB = Forty Mile Brook. NRV = Nepisiguit River Valley.

each of the tectono-stratigraphic groups. These differences match the geologic contacts used for windowing the original data and are first order, being the largest with how the data is altered. The second order difference, superimposed on top of the tectono-stratigraphic difference, reflects topographic effects. Since the correction uses varying densities, the influence of a topographic feature is corrected differently across the study area. The most prominent example of this is caused by the deep Nepisiguit River Valley (NRV, area identified in Figure 4-4C) running roughly east-west through the study area. Where the terrain is more rugged and the channel cut deeper, the variable density grid imposes a lower correction resulting in a greater Bouguer value at that point. Assuming that the topography is comprised of a single tectono-stratigraphic unit, the true Bouguer anomaly should have little to no correlation with topography (Nettleton, 1939). The new variable density terrain correction does indeed result in a lower association between Bouguer gravity and topography than when a camp-wide average is applied. This relationship exists through the study area and is fundamental when topography is geologically controlled (Vajk, 1956).

The difference between the AGG variable density and constant density terrain corrected grid is also subtle. This result applies to all tensor components but for brevity is only shown for Gzz (Figure 4-4). In the original AGG grids, globally constant terrain correction values were applied ranging for 2.40 g/cm^3 to 3.00 g/cm^3 at 0.10 g/cm^3 increments. It can be seen in Figure 4-4 that this may interfere with the true gradiometry anomaly by introducing topographic error. Where locally the geologic density matches the correction value this incremental method may be appropriate. Across larger areas, where near surface densities have structural - stratigraphic controls, such as in the BMC, this introduces considerable error. The influence of the NRV (Figure 4-4D) for example, appears to interfere with the true Gzz anomaly producing false positives and negatives but is minimized within the variable density grid implying a correct reduction value.

Using two examples where there are marked differences in the gradient anomaly when different terrain correction values are used (NRV and part of the Forty Mile Brook drainage basin, FMB) it is possible to determine the relationship of topography to the Gzz anomaly using a plot of covariance between Gzz and the topography against different density correction values (FitzGerald, 2011, Figure 4-6). The slope of the line of best fit relates to the importance of topography with a steeper slope indicating greater importance. At the x-intercept, where covariance is zero, the Gzz anomaly should have no correlation with topography and an optimum density correction value can be found. As seen in Table 4-2, the density correction values used in the variable density correction grid turn out to be very close to the ‘optimum’ correction density values derived from the best-fit slope computation (Figure 4-6A, B). However, instead of having to cross reference several grids, as in the case of the incremental terrain correction, all the information is presented in a single image. It is important to note that this method works better in areas of high relief. Of the two example areas, both are rugged/ hilly but the NRV has a greater dynamic range than the FMB, 168 - 620 m.a.s.l. versus 280 – 642 m.a.s.l. respectively. Also, the NRV area has a tighter grouping of low elevation points relative to the FMB (Figure 4-6C) and therefore a sharper contrast with topography. When there is only limited elevation variation across an area then the slope of the density - covariance line is reduced; when the slope is shallow the optimum density value is poorly constrained.

Previously Lane (2004) has shown when comparing GG and AGG data sets that GG data, as might be expected, records longer wavelength signal not detected by the flight line length limitation imposed by the airborne survey. Lane (2004) also showed that more the regularly sampled flight and tie lines associated with AGG surveys detects finer scale structure that is beyond the resolution of most GG data collections. The Bathurst Mining Camp provides an additional opportunity for also comparing ground and airborne data sets that is a little different. Many of the original mineral deposits in the Bathurst area had significant concentrations of dense sulphidic minerals and hence ground gravity surveys were used as a mineral deposit prospecting tool. This has produced a significant number of areas with very dense sampling. At the same time regional scale surveys supported by the Federal and Provincial government research programs (TGI3 and TGI4) have resulted in broad regional coverage. As noted above, locally individual station spacing varies from 50 m to over 3 km with a nominal spacing of 477m. This means that there are areas for which the ground gravity sampling is finer and other areas where it is coarser than the airborne surveys. Visually, the GG and the AGG datasets appear quite similar and correlate well with the mapped geology when all parameters (observation level, grid cell size, etc.) are equal (Figure 4-5A, B). Areas with large volumes of mafic rocks associate with gravity highs while dominantly rhyolitic or sedimentary areas correlate with gravity lows. The dynamic ranges of both systems is also very similar (-9.84 to 13.25 mGal and -9.72 to 13.65 mGal for GG and AGG grids respectively) indicating comparable amplitudes in the reduced data. Primary differences arise in the geometry of the bodies. The level of detail recorded by the AGG system is much higher than the GG approach, recording information along regularly spaced lines at a high frequency as opposed to limited ground access and varying station spacing.

Directly comparing the two data types via subtraction (AGG – GG, Figure 4-5C) reveals a spatial pattern in the difference. The mean and standard deviation of the difference is -0.03 mGal and 1.45 mGal respectively. Within the difference image, 1 mGal on either side of the mean has been blanked; 1 mGal corresponds to the maximum uncertainty contained in the legacy GG data (Thomas et al., 2008). The largest differences between the two grids exist along the AGG survey edges. The vertical integration filter applied to the AGG data involves roll-off which extends the data some distance beyond the grid edges in order to satisfy the Fourier transformation. The GG data on the other hand is not transformed and contains real

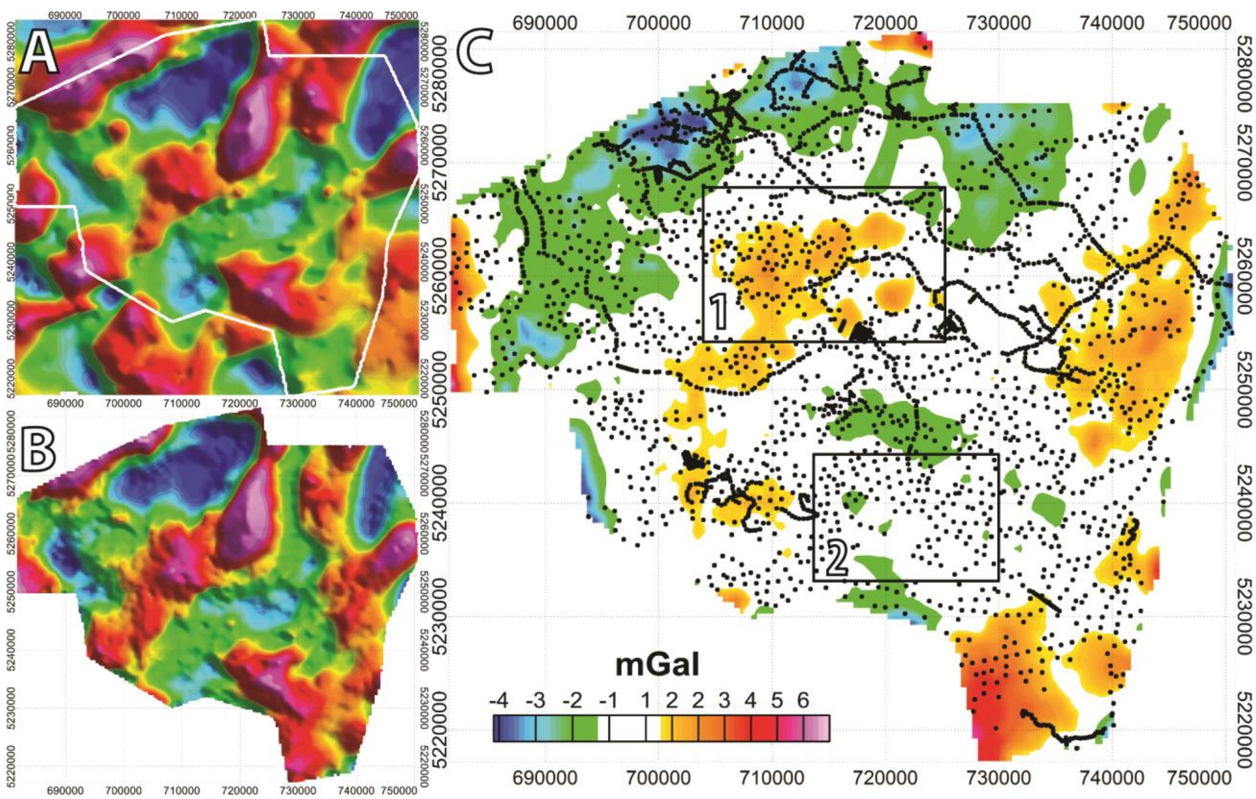

Figure 4-5: (A) Variable density ground gravity dataset as viewed from 250 m constant terrain clearance. **(B)** Variable density AGG data observed from a 250 m constant terrain clearance. Both GG and AGG data have undergone bandpass filtering to restrict frequency content to greater than 1 km and less than 30 km. **(C)** Difference between AGG and GG datasets with ground locations overlain. Linearly equalized colouring with 1 mGal on either side of the mean coloured white. Box 1: area of poor correlation; box 2: area of good correlation.

information content throughout since data was collected beyond the limit of the AGG survey. Integration of the AGG is therefore creating inaccuracies which must be considered. Some areas appear to exhibit a small DC shift between the two data sets. In these areas the data from one survey appears to be systematically higher or lower than the other data set. The variation does not seem to correlate with the underlying geology or local topography. To investigate this issue we compare the radial energy spectral properties of data for two areas, one where there is poor correlation between the two surveys (Box 1, Figure 4-5C) and one where there is good correlation (Box 2, Figure 4-5C). First, we compute the difference in radial energy spectrum between the two areas for a single survey methodology. This spectral difference reflects the geological differences between two areas: it should be the same for each data set since each grid uses the same grid cell size and was filtered identically. Second, we compute a radial energy spectral difference between the response from the two observation methods (AGG vs. GG (Figure 4-7). If there is no difference in frequency content recorded by the two surveys then the difference in spectral content for the two areas should be similar. The spectral contrast for the two areas is, however, not identical. The AGG is recording a higher variation in signal amplitude below 6 km wavelength in these areas. Above 6 km the spectral information of both images converges to 30 km, the lowest frequency content imposed by high pass filtering. The higher amplitude variation for shorter wavelengths found in the AGG data implies it is more sensitive to the near surface relative to GG. At wavelengths less than 1.5 km the GG is more variable than the AGG. We believe this to be due to the sporadic data distribution and the effect of minimum curvature gridding. A common gridding artifact arising from minimum curvature interpolation of sporadic GG data is the generation of significant signal peak or trough for an area of low station density lying between other areas which have a much higher station density. Evidence of this effect is clearly present in the anomaly difference grid where a number of bulls-eye anomalies, absent of any information on the anomaly, but surrounded by ground observations (Figure 4-5C).

Conclusion

Though the idea of variable density correction has been around for over half a century, there have been few examples of its application in the literature. The Bathurst Mining Camp, northern New Brunswick, Canada, represents are area where such a correction is necessary as tectonic thrusting has resulted in the juxtaposition of very different types of lithological terranes with each of the terranes having different average density values. Density measurements acquired on drill core and from field sites collected throughout the Camp were averaged to produce real world correction values for the tectono – stratigraphic groups and overlaying sequences. These optimal density values are then applied to Bouguer and terrain corrections for ground gravity stations acquired in the respective underlying units. A variable density Bouguer anomaly map was created as the final product. A similar methodology was also

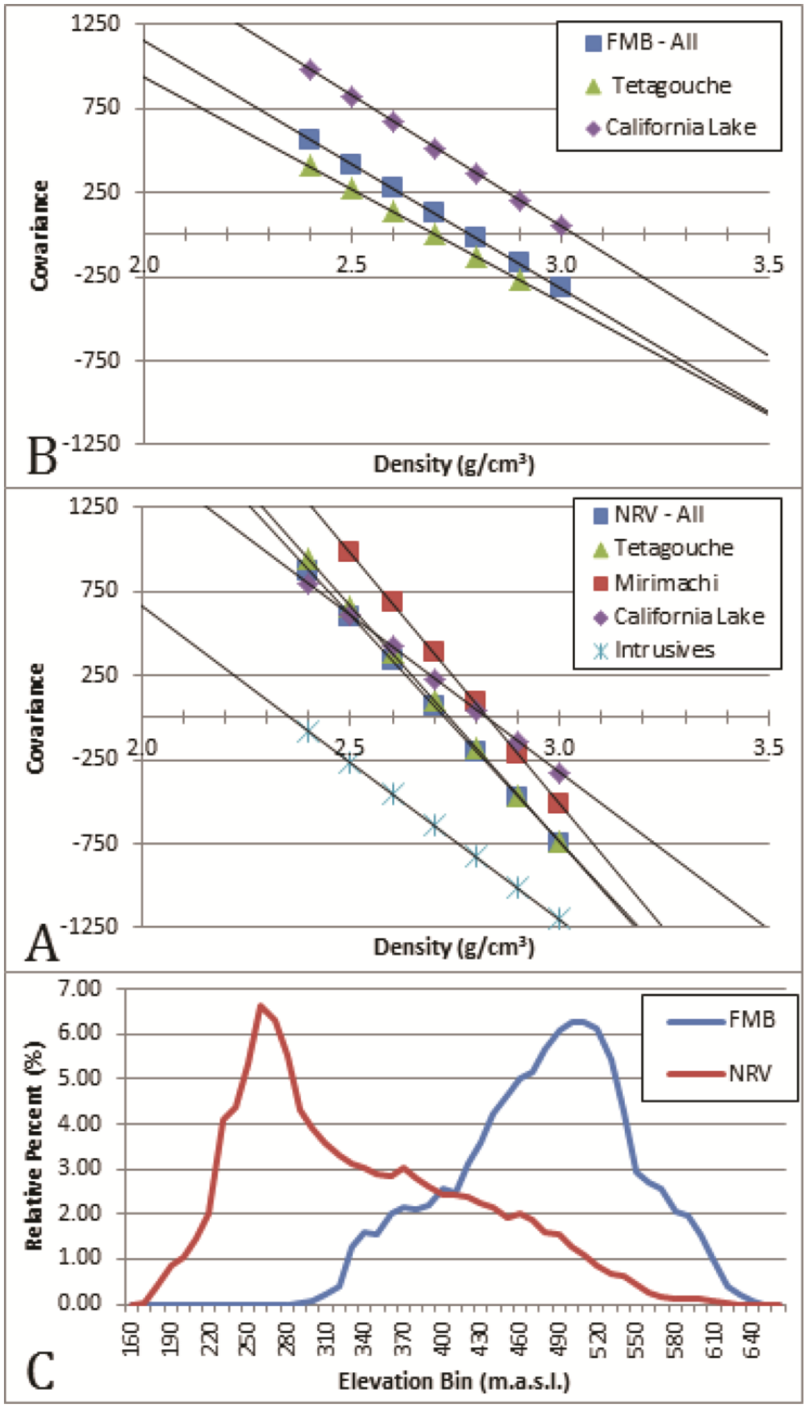

Figure 4-6: (A) Gzz – DEM covariance against topographic density correction value for the Nepisiguit River Valley (NRV). **(B)** Gzz – DEM covariance against topographic density correction value for the Forty Mile Brook area (FMB). The locations of both areas is identified in Fig. 4C. **(C)** Ruggedness of both areas defined by the relative percentage of elevation values from the DEM.

Table 4-2: Result from covariance plots and densities used in the VD correction

Tectonic Block	Slope	X - intercept	VD correction value (g/cm^3)
Nepisiguit River Valley			
Miramichi	-2987.6x	2.83	2.75
California Lake	-1870.6x	2.82	2.82
Tetagouche	-2807.7x	2.73	2.72
Intrusive	-1870.3x	2.40	2.75
Forty Mile Brook			
California Lake	-1548.6x	3.03	2.82
Tetagouche	-1338.6x	2.70	2.72

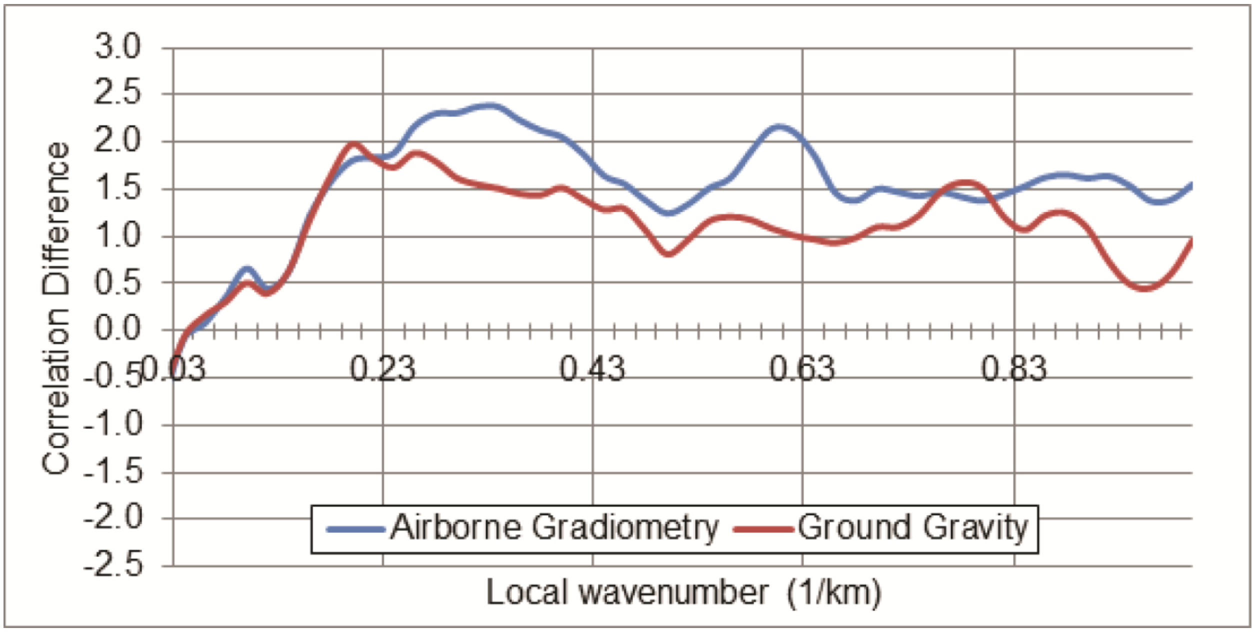

Figure 4-7: Correlation difference comparing the spectral difference between boxes 1 and 2 from figure 5C for airborne gravity gradiometry and ground gravity.

applied to AGG data where terrain correction density values can have a significant impact on the resultant tensor components. In both cases the isolated anomalies are better resolved and the impact of topography on the final gravity image is significantly reduced. The GG product closely resembles the mapped geology which was based largely on airborne magnetic and electromagnetic data sets and better resolves isolated dense bodies juxtaposed against larger dense packages. Within the AGG data it is evident there is an issue with finding a proper terrain correction value to use across the Camp. Depending on the density value used for terrain correction, artifacts of the topography can be carried through into the final gradient anomaly map. We suggest that if a systematic density data base is available it is possible to employ a variable density correction which will minimize the effects associated with assuming a constant density in cases where there is high variation and a spatial control on the density distribution within a given area. Primarily these variable density maps may be used as a template for outlining geological lithologies and structures. It is fundamentally a mapping product; it is not the product that would most commonly be used in geophysical model development.

An additional step would be to further subdivide the tectono – stratigraphic packages into individual formations preferable on the basis of a quantitative type lithology. With increasing rock property information (Tschirhart, 2013) this is becoming ever more possible to do, but in this instance, gravity stations are simply too dispersed and such a division level would limit the number of GG observations within a formation. Many may be completely missed. An airborne survey, however, may benefit from this level of detail on par with the formations as there is much more regularity in the sample spacing and frequency. This level of discrimination is also dependent on the accuracy of the geologic map. At a tectono – stratigraphic division, the tectonic blocks are well defined. At a lithologic scale partition, error may be introduced by incorrectly assigning a density where the geology is poorly understood.

References

Chapin, D., 1996. The theory of the Bouguer gravity anomaly: A tutorial. The Leading Edge, **15**, 361-363.

Chen, J., and Macnae, J.C., 1997. Terrain corrections are critical for airborne gravity gradiometer data. Exploration Geophysics, **28**, 21-25.

Dransfield, M., 2007. Airborne gravity gradiometry in the search for mineral deposits, *In* Proceedings of Exploration 07: Fifth Decennial International Conference on Mineral Exploration. *Edited by* B. Milkereit, 341-354.

FitzGerald, D., 2011. Gravity gradient terrain correction challenges, Intrepid Geophysics.

Fullagar, P., and Pears, G., 2010, From gravity gradients to density gradients, *In* Airborne Gravity 2010 - Abstracts from the ASEG-PESA Airborne Gravity 2010 Workshop. *Edited by* R. J. L. Lane, 79 – 86.

Hinze, W.J., 2003. Bouguer reduction density, why 2.67?: Geophysics, **68**, 1559-1560.

Houghton, P., Bate, D., Davies, M., Lumley, J., 2007. Using gravity gradiometry as a blueprint for exploration in thrust and fold belts, First Break, **25**, 105-112.

Kass, M.A., and Li, Y., 2008. Practical aspects of terrain correction in airborne gravity gradiometry surveys, Exploration Geophysics, **39**, 198-203.

Lane, R., 2004. Integrating ground and airborne data into regional gravity compilations. *In* 2004, Airborne Gravity 2004 – Abstracts from the ASEG – PESA Airborne Gravity 2004 Workshop. *Edited by* Lane, R.J.L., Geoscience Australia Record 2004/18, 81-99

LaFehr, T.R., 1991. Standardization in gravity reduction, Geophysics, **56**, 1170-1178

Li, Y., Kass, M.A., Davis, K., Braga, M., and Martinez, C., 2010. Terrain correction and its effect on 3D inversion of airborne gravity gradiometry data. *In* Airborne Gravity 2010 - Abstracts from the ASEG-PESA Airborne Gravity 2010 Workshop. *Edited by* R. J. L. Lane, 131 -141.

Mims, J., Cuma, M., Wilson, G., Mataragio, J., Zhdanov, M.S., 2012. Recent advances in airborne gravity gradiometry: A case study from the Bathurst Mining Camp. *In* KEGS-DMEC Exploration '07 plus 5: A half-decade of mineral exploration developments.

Morris, R., Jobin, D.M., Thomas, M.D., Rogers, N., McCutcheon, S.R., 2007. New Gravity Data for the Bathurst Mining Camp, Northeastern New Brunswick: A colour-shaded Bouguer gravity anomaly map (linear colour contour interval) with gravity station locations and posted Bouguer anomaly values, Geologic Survey of Canada, Open File 5542, New Brunswick Department of Natural Resources, Minerals, Policy and Planning Division, Plate 2007-13A.

Nettleton, L.L., 1939. Determination of density for reduction of gravimeter observations. Geophysics, **4**, 176-183.

Singh, P., Pandey, R.S., Gupta, S.K., Nainwal, N.C., Asthana, M., 2006. Bouguer reduction with lateral variable surface densities – A model based case study in geologically complex Frontier Area *In* 6th International Conference & Exposition on Petroleum Geophysics, 72-77.

Smith, R., Shore, M., and Rainsford, D., 2012. How to make better use of physical properties in mineral exploration: The exploration site measurement. The Leading Edge, **31**, 300-337.

Thomas M.D., Jobin, D.M, and Roger, N., 2008. Updated Gravity Maps of the Bathurst Mining Camp, Northeastern New Brunswick. Geological Survey of Canada Map, Open File 5875, Sheet 1: Colour-Shaded Bouguer Gravity Anomaly. New Brunswick Department of Natural Resources, Mineral, Policy and Planning Division, Plate 2008-1A. Scale 1:150,000.

Tschirhart, P., 2013. Geophysical processing and interpretation with geologic controls: Examples from the Bathurst Mining Camp, New Brunswick. Unpublished M.Sc Thesis. McMaster University, Hamilton, ON.

van Staal, C.R., Wilson, R.A., Rogers, N., Fyffe, L.R., Langton, J.P., McCutcheon, S.R., McNicoll, V., and Ravenhurst, C.E, 2003a. Geologic and tectonic history of the Bathurst Supergroup, Bathurst Mining Camp, and its relationship to coeval rocks in Southwestern New Brunswick and adjacent Maine - A synthesis. *In* Massive Sulfide Deposits of the Bathurst Mining Camp, New Brunswick, and Northern Maine. *Edited by* W.D., Goodfellow, S.R., McCutcheon, and J.M., Peter. Economic Geology Monograph 11, 37-60.

van Staal, C.R., Wilson, R.A., Rogers, N., Fyffe, L.R., Gower, S.J., Langton, J.P., McCutcheon, S.R., and Walker, J.A., 2003b. A new geologic map of the Bathurst mining camp and surrounding areas—A product of integrated geological, geochemical, and geophysical data. *In* Massive Sulfide Deposits of the Bathurst Mining Camp, New Brunswick, and Northern Maine. *Edited by* W.D., Goodfellow, S.R., McCutcheon, and J.M., Peter. Economic Geology Monograph 11, 61-64.

Vajk, R., 1956. Bouguer corrections with varying surface density. Geophysics, **21**, 1004-1020.

Chapter Five: Improved edge detection mapping through stacking and integration: A case study in the Bathurst Mining Camp

Peter Tschirhart and Bill Morris

MAGGIC, SGES, McMaster University, Hamilton ON, L8S 4K1

Abstract

Airborne geophysical surveys provide spatially continuous regional data coverage which directly reflects subsurface petrophysical differences and thus the underlying geology. A modern geologic mapping exercise requires the fusion of this information to compliment what is typically limited regional outcrop. Often interpretation of the geophysical data in a geological context is done qualitatively using total field and derivative maps. With a qualitative approach, the resulting map product may reflect the interpreter's bias. Source edge detection (SED) provides a quantitative means to map lateral physical property changes in potential and non-potential field data. There are a number of SED algorithms, all of which apply a transformation to convert local signal inflections associated with sources edges into local maxima. As a consequence of differences in their computation, the various algorithms generate slightly different results for any given source depth, geometry, contrast and noise levels. To enhance the viability of any detected edge it is recommended that one combine the output of several SED algorithms. Here we introduce a simple data compilation method, deemed edge stacking, which through direct gridding, grid addition and amplitude thresholding improves the interpretable product of SED. In two examples, a synthetic example and real world example from the Bathurst Mining Camp, New Brunswick, Canada, a number of transformation algorithms are applied to gridded geophysical datasets and the resulting SED solutions combined. Edge Stacking combines the benefits and nuances of each SED algorithm; coincident, or overlapping solutions are considered more indicative of a true edge, while isolated points are taken as being indicative of random noise or false solutions. When additional data types are available, as in our example, they may also be integrated to create a more complete geologic model. The effectiveness of this method is limited only by the resolution of the survey data and the necessity of lateral physical property contrasts. The end product aims at creating a petrophysical contact map which when integrated with known lithological outcrop information can be lead to an improved geological map.

Introduction

Geophysical datasets are fundamental to geologic mapping and interpretation, especially in areas of limited or no outcrop. Patterns in the geophysical data may outline the orientation and continuity of boundaries between regions with uniform petrophysical properties. In a map these boundaries can help define fault offsets and outline fold structures. When used in conjunction with what is often limited outcrop information it is possible to use the geophysical data to develop a significantly improved geologic interpretation. Central to this approach of geophysical mapping is the use of quantitative methods to locate the edges, or lateral changes of source bodies. Source edge detection (SED) provides a means of quantitatively mapping lateral changes in magnetization or mass density where there is sufficient physical property contrast in magnetic and gravity data respectively (Blakely and Simpson, 1986). Prior to computing SED the field data must be transformed, or 'enhanced' to convert local signal inflections associated with source edges into local maxima (peaks). There are number of algorithms that are capable of locating a source edge. Horizontal gradient of total field (TF-hgm, Cordell, 1979), tilt derivative (TI, Miller and Singh, 1994), horizontal gradient of pseudogravity (PSG-hgm, Cordell and Grauch, 1985), and 3D analytic signal (AS, Roest et al., 1992) are among the older and more established methods. Newer methods such as the Theta map (TH, Wijns et al., 2005) have been developed to overcome some of the perceived shortfalls of previous routines.

Typically source edge detection algorithms are applied only to potential field datasets that satisfy Laplace's equation. However, as shown by Beamish (2012) and Tschirhart et al., (2013), some of these techniques may also be practical for non-potential field data. Beamish (2012) investigated the usefulness of spatial derivatives for interpreting conductivity data, noting that "as long as it is recognized that the same transformed non-potential field data cannot be 'treated' in the same manner then the inherent filtering aspect of the transformation can still be successfully applied to non-potential field data." When applying these techniques to helicopter-borne frequency domain EM (HFEM) data it is necessary to understand how the source-signal response for this technique differs from that associated with potential fields. For example, the depth of penetration of an EM signal is dependent on the transmitter frequency which in most situations limits source detection to the near surface. EM data is also more compact than potential field data; the rate of signal decay off-source is much sharper. Perhaps most important is the recognition that EM is primarily detecting lateral variations in resistivity and is therefore sensitive to the presence of significant overburden thickness changes. Nonetheless, Tschirhart et al., (2013) has shown how SED on multi-component HFEM apparent resistivity data can significantly improve the geologic interpretation. SED mapped lateral changes of a conductive schist in contact above with a resistive quartzite and a below with a resistive arkosic metawacke.

Pilkington and Keating (2004, 2009) showed that when one compares the output from five SED algorithms the results are highly variable depending on the method chosen. Some methods perform an automatic gain control (AGC) normalizing the dynamic range of the field, and allow for more subtle expressions to be detected. AGC's may also amplify noise and thereby create false peaks, or SED solutions. Conversely, other routines tend to select only prominent high amplitude features, ignoring more subtle expressions. Cascone et al (2012) specifically identified an issue with the Tilt derivative SED method. As they note this approach will always form "a closed loop which are not related to real geological features along their whole length." A second issue recognised by Cascone et al., (2012) is that the location of an edge associated with a broad, low amplitude signal is spatially less well constrained than for more sharply defined anomalies. Pilkington and Keating (2004, 2009) conclude that no one routine works best and suggest each method be used in conjunction, though they do not provide any routines for combining response signals. Cascone et al., (2012) addressed this issue through a procedure called ACLAS which combines the response of the Total Horizontal Derivative (THD) and the Tilt zero contour through a signal coherency approach.

In this paper we seek to continue this discussion on methods to improve the interpretable product of edge detection solutions by introducing an edge stacking approach which involves solution stacking and direct gridding. We expand on this to demonstrate how quantitative addition of multiple edge solutions serves to enhance true edges while minimizing false peaks. Finally, we show how introducing stacked solutions from additional geophysical data (magnetics, gravity gradiometry, and electromagnetics) can result in a more complete geologic picture.

Methods

The first step in the source edge detection process is to transform the data into a format appropriate for edge computation. For all data types this involves interpolating flight line data into an image grid format; the choice of gridding algorithm and grid cell parameters can influence the final edge detection computation. Magnetic surveys also require all data to be transformed using a Reduction to the Pole filter. For gravity surveys it is common practice to work with first vertical derivative data. This transform has the advantage of enhancing the commonly smooth edge transitions found in gravity data sets. The second step of SED involves transformation of the gridded datasets into a format where source edges are defined as positive anomaly peaks. Reviews on various algorithms can be found in Pilkington and Keating, (2004), Cooper and Cowan, (2006) and Pilkington and Keating (2009). The final step of source edge detection procedure involves isolating the apex location of the anomalous peaks (Blakely and Simpson, 1986). Criteria (peak amplitude cut off value and peak geometry) employed in separating geologically meaningful peaks from those caused by signal acquisition and processing artefacts vary according to each enhancement method and are a subjective choice of the operator. In all cases noise must be hedged against the number of solutions.

Having computed a database of source edge solutions using a number of different SED algorithms, our next step is to combine these results into a single edge solution map. In this study we propose a procedure based on a simple data stacking approach. Increased confidence in the validity of a source edge location can be assigned to an edge that is found at the same location by a number of different signal processing algorithms. We achieve this data stacking approach through application of the following steps. Peak solutions for a specific data set and processing algorithm are gridded to the cell size of the original gridded data, such that if a solution exists at a particular XY location, the grid cell is assigned a value = 1, else 0 or null. Using a direct gridding algorithm accomplishes this without any extrapolation of the data. The same procedure is then applied to the output of all the different SED algorithms. All gridded solutions are then sampled into a master database and because all have uniform grid cell size and identical locations, XY values match and it is possible to compute a sum of spatially coherent solutions for each pixel location. If for example two of four image enhancements have SED solutions at the same XY location, the pixel location sums to 2, if all procedures generated solutions at this location, values would sum 4 and so forth. In this paper we have chosen an approach where we assign equal weighting to all SED solutions. In the future it is possible that one might develop a variable weighting approach which takes into consideration aspects of the geometry of the original observed data signal. Central to our hypothesis is that where multiple solutions locate, there is greater confidence of a true contact, while lower values more likely represent noise. After the solutions are stacked, the data may be regridded or plotted as coloured polygons. Regridding the data allows for additional, different source datasets to be included into the final solution. Electromagnetic, or gravity, data for example may be included here to help further the geologic model by allowing additional physical property constraints on source location. Leblanc et al., (2012) employed a similar simple data stacking approach to generate a data fusion product from individually normalised radiometric, aeromagnetic and VLF data. Another added benefit of gridded data is it may be subjected to amplitude thresholding and line thinning (Lam et al., 1992) to create polylines for geologic mapping.

Synthetic Model

A synthetic model is used to demonstrate the methodology and effectiveness of edge stacking (Figure 5-1). The model includes four bodies of varying geometry, susceptibility, density and depth (Table 1) exposed to a magnetic field of 60,000 nT at an inclination of 90° and declination of 0°. Background density and susceptibility are 2.67 g/cm^3 and 0 SI respectively. Gaussian noise is added to each model at 5% the standard deviation for magnetic and gravity gradient grids. The resultant magnetic and vertical derivative of gravity grids with source body outline overlain are shown in Figure 5-1A, A'.

Four SED algorithms (TF-hgm, PSG-hgm, TI, TH) are applied to the magnetic data, and three (TF-hgm, TI, TH) are applied to the gravity gradient data (Figure 5-1B, B'). Noise in the magnetic grid makes it especially prone to false peaks. In the gravity gradient data where the anomalies are more pronounced noise is less influential, and few false peaks are detected. Algorithms that use an AGC and normalize the field accentuate local features within the signal and are particularly vulnerable to noise enhancement (ex. tilt and theta). In contrast algorithms based on gradient transforms tend to ignore the subtle signal fluctuations and only detect peaks over the most prominent gradients. Discrepancies in the source edge locations computed for the various source bodies arise both within a specific signal parameter (TH versus TI on magnetics), as well as between sensor signals (gravity versus magnetics). TI and TH methods tend to resolve a wider body than that of TF-hgm and PSG-hgm, especially in the case of the sphere. Gravity gradient derived edges also tend to be further off the body than magnetic edges due to the broader, more smoothly varying gravitation field attributed to the different source signal versus distance variation (r^3 for magnetics versus $2/r^3$ for gravity gradiometry).

Traditional SED interpretation would stop here and continue in either a qualitative way to map the bodies from point solutions in conjunction with the geology, or in a semi-quantitative way by essentially connecting the dots. We take this one step further by combining the edges from the magnetics and gravity into a single entity (Figure. 5-1C). When combined, the source edge detection solutions increase the confidence of a given edge by combining multi-parameter information about source location. A prominent density contrast may be able to better resolve a body if only a subtle magnetic susceptibility contrast exists. This is true especially for interfering fields, such as is present in our synthetic model between the thin dyke and the thin sill. Where the gravity gradient SED solutions fail to resolve the south western corner, the magnetic SED solutions atone and when combined all corners are mapped. Information such as body dip direction may also be extracted from the combined edges. For the dipping slab, the magnetic SED solutions effectively maps the body's top surface, while the down-dip skew of the gravitation field cause gravity gradient SED solutions to locate more easterly. Combining the two solutions, the western edge is very well defined, while the eastern side is broadly distributed indicating an eastwardly dipping body.

Finally, gridding and limiting the minimum value in the histogram effectively cleans the resultant image (Figure 5-1D). Many of the solutions occurring individually as an isolated point are false peaks caused by noise. Disregarding these values simplifies interpretation and better resolves the source geometry by enhancing continuity. Though some noise is still present resulting from the similarities in the TH and TI solutions, it is minimal compared to when left in.

Table 5-1: Geometries of synthetic shapes

Body Geometry	Dip	Depth to top (m)	Width / Radius (m)	Depth Extent (m)	Susceptibility (SI)	Density Contrast (g/cm^3)
Sphere	90	300	200	-	0.015	+ 0.3
Thin dyke	90	100	1000	500	0.005	+ 0.6
Thin Sheet	0	300	50	50	0.01	+ 0.8
Dipping Prism	65	150	250	500	0.01	+ 0.2

Background Susceptibility 0 SI, field strength 60,000 nT, Inclination 90°, declination 0°

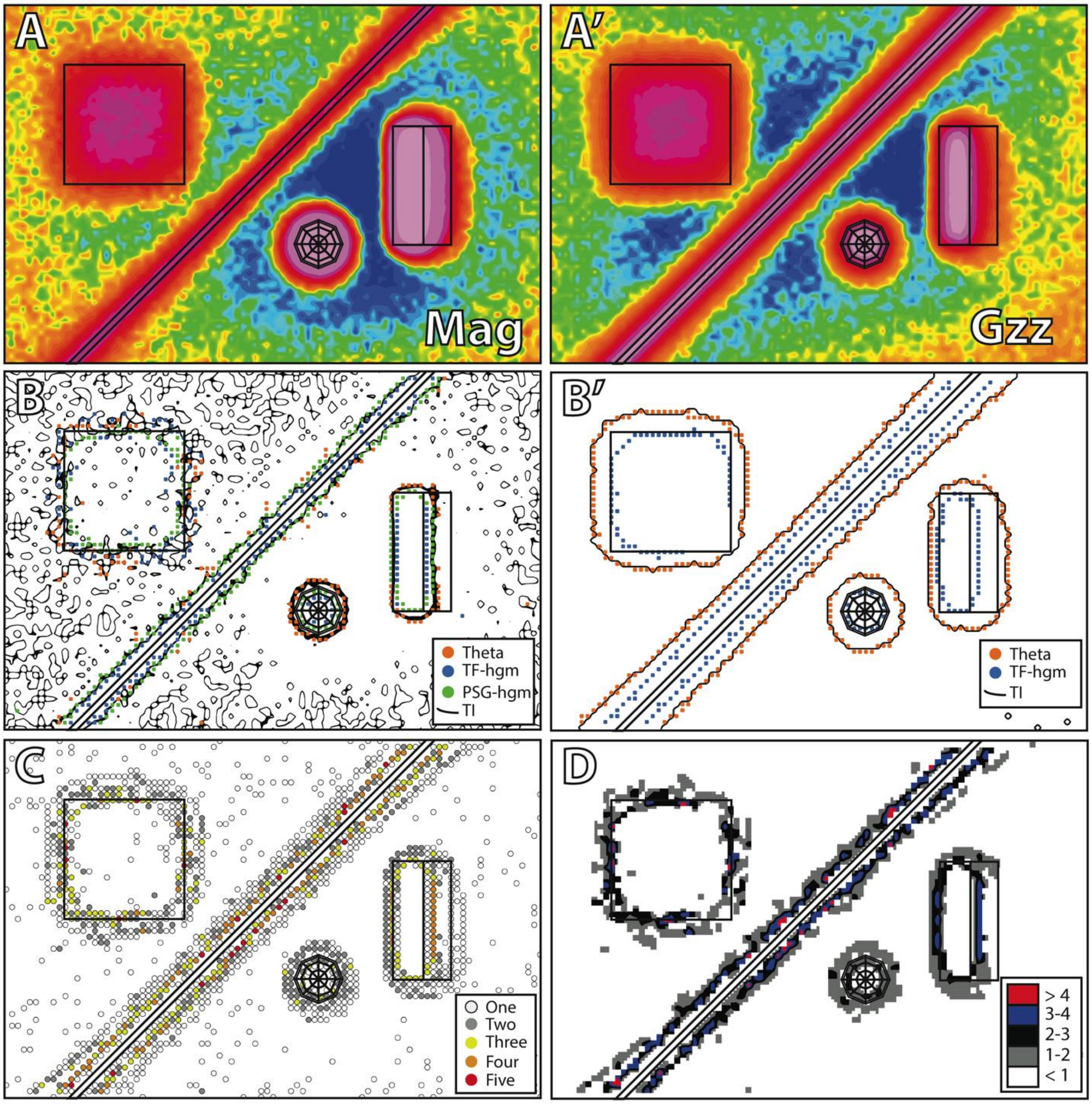

Figure 5-1: A synthetic example demonstrating the usefulness of stacking multiple edge solution from difference datasets to improve confidence. **(A)** Synthetic magnetic example with 5% random noise. **(A')** Synthetic gzz gravity gradiometry component with 5% random noise. **(B, B')** Edge solutions from different image enhancement techniques. **(C)** Stacked edges displayed as dot. **(D)** Stacked edges gridded using direct gridding. Values 1 and below have been rejected.

In this synthetic example the combined gravity gradiometry and magnetic data yielded a total of seven possible solution sets. Pixels with an edge detection sum of 1 or less were considered invalid and rejected in Figure 5-1D. With the SED solutions gridded, line thinning may also be effectively applied to automate polyline contacts of the source bodies.

Test Area and Survey Data

To demonstrate the usefulness of this approach, we apply it to various geophysical surveys collected across the Nine Mile Synform (NMS), New Brunswick, Canada (Figure 5-2). The north westerly plunging NMS, a central feature of the Bathurst Mining Camp (BMC), was formed by juxtaposition and imbrication of tectonic blocks of the Fournier, California Lake, and Tetagouche Groups. Initially these blocks formed diachronously as individual sub-basin within the Tetagouche – Exploits back arc basin along the Laurentia coast during the Early to Middle Ordovician. Each block is characterized by unique volcanic and sedimentary stratigraphy. Successive incorporation of the blocks into the Brunswick subduction complex during the Late Ordovician to Early Silurian produced long lived, polyphase deformation (van Staal et al., 2003). The NMS is an expression of a late stage D_4 ductile- brittle, dextral transpression which caused tectonic uplift of the BMC.

A number of distinct horizons with unique geophysical signatures are apparent in the various geophysical datasets through the study area. Magnetic anomalies in the NMS predominantly emanate from mafic volcanic and mafic intrusive rocks, which have shown from laboratory magnetic susceptibility measurements to locally be highly susceptible (Thomas et al., 2000, Tschirhart, 2013). Conductivity anomalies are locally caused by black shale beds, argillite, and chloritic formations (Keating et al., 1998). Gravity and consequentially gradiometry anomalies primarily stem from increases in mafic rock volume, which are on average 0.05 – 0.2 g/cm^3 denser than felsic and sedimentary equivalents (Thomas et al., 2000, Thomas et al., 2003, Tschirhart, 2013). Starting geophysical datasets are shown in Figure 5-3.

Extensive and successful application of airborne geophysics for volcanogenic massive sulphide exploration in the BMC has resulted in numerous datasets available in the public domain through Natural Resource Canada's data repository (http://gdr.agg.nrcan.gc.ca). Two airborne magnetic - electromagnetic surveys (Aerodat and MegaTEM II) and an airborne full tensor gravity gradiometry (AGG) survey (Bell Geospace) are used in this study. Survey specifications for the Aerodat frequency domain EM survey (HFEM), flown in 1995, follow a gentle drape surface at 60 m clearance with magnetometer and EM bird towed at 15 m and 30 m, respectively, below the helicopter. Flight and tie lines were 200 m and 2000 m respectively. Deliverables from the Aerodat survey included a total field magnetic map and apparent conductivity maps for the 32k Hz and 4433 Hz EM frequencies. The MegaTEM II time domain EM survey (TDEM), flown in 2003, followed a nominal terrain clearance of 120 m with 200 m

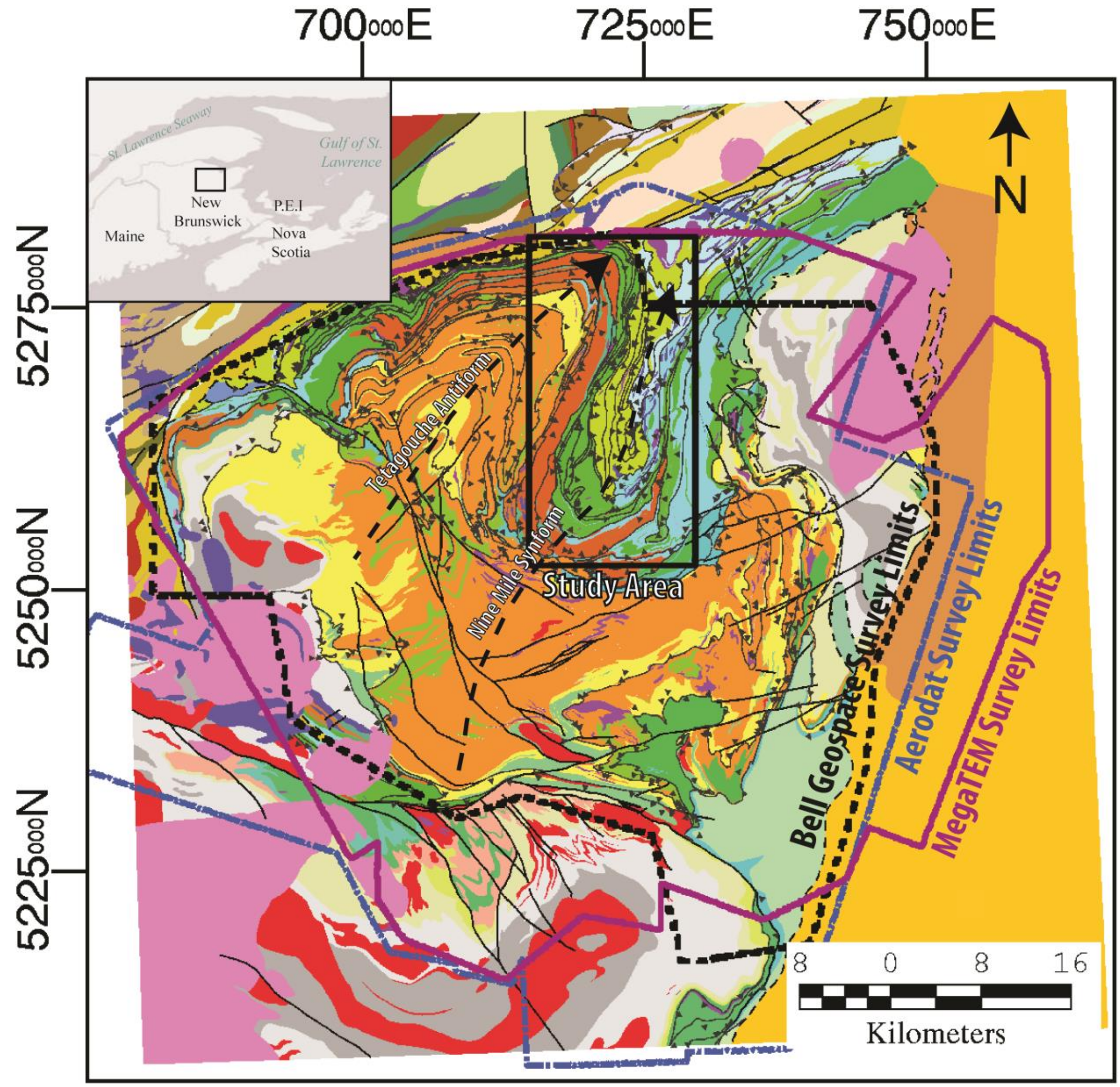

Figure 5-2: Geology of the Bathurst Mining Camp, New Brunswick from van Staal et al., 2003. Spatial extents of the airborne geophysical survey delineated.

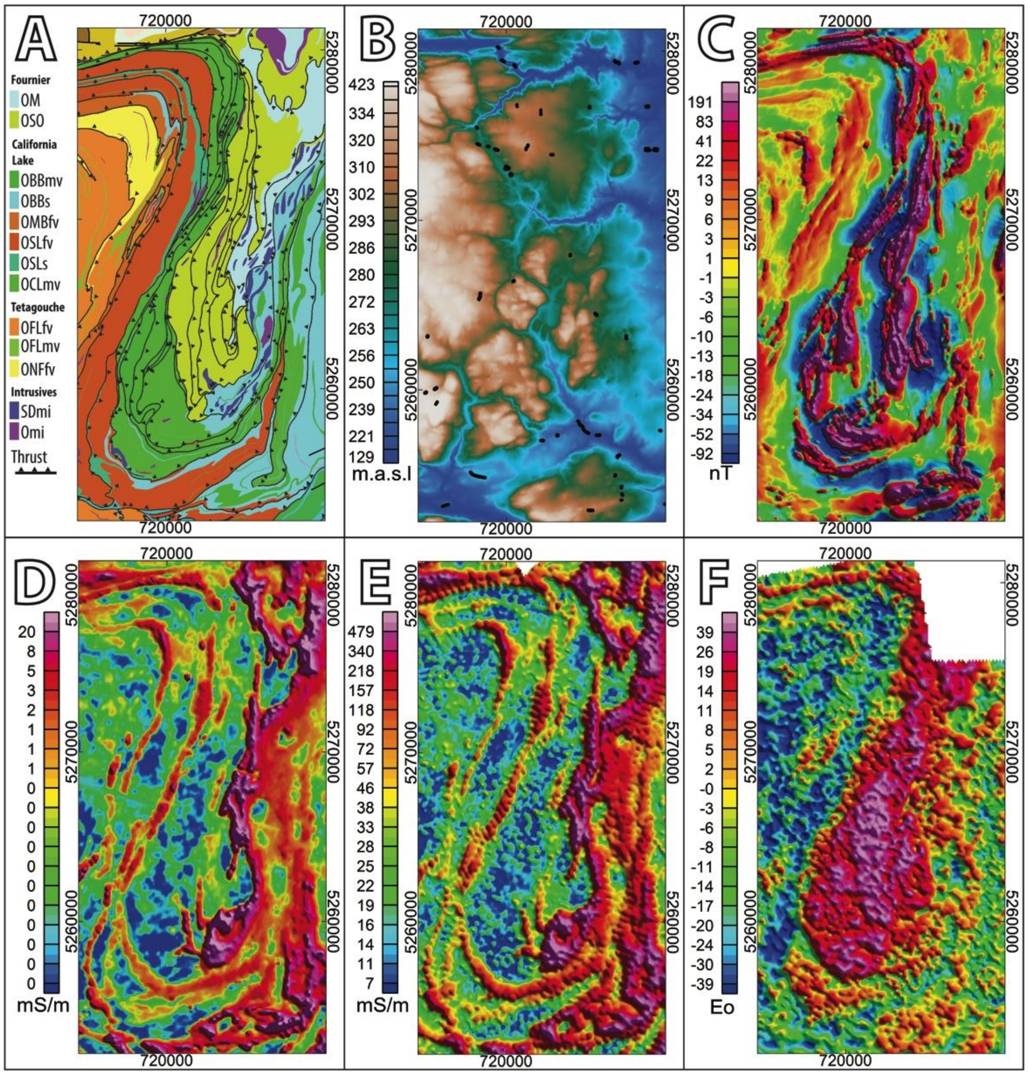

Figure 5-3: Individual datasets used for mapping purposes. Geologic contacts from Open file 4128 overlay the geophysical data. **(A)** Geologic map of the study area from Open File 4128 (van Staal et al., 2003) **(B)** DEM overlain with outcrop locations from Open File 3839 (van Staal and Rogers, 1999); *note*: size of outcrop has been exaggerated for display. **(C)** Aerodat residual magnetic dataset. **(D)** Apparent conductivity map at a frequency of 4433 Hz, HFEM system. **(E)** Apparent conductance, TEM system. **(F).** Vertical gravity gradient (Gzz). For brevity addition datasets including Aerodat 32k Hz apparent conductivity, MegaTEM residual total field magnetics, and tensor components Txx, Txz, Tyy, Tyz, Txy are not shown.

and 2000 m flight and tie lines. Deliverables included total field magnetics and apparent conductance. For both the Aerodat and MegaTEM magnetic datasets regional residual separation was achieved using an 800m non-linear filter to remove the contributions of deep and broad anomalies (Keating and Pinet, 2011). Residual anomalies were compared against HFEM apparent susceptibility calculated for the area to determine an optimum residual (Tschirhart, 2013). Bell Geospace gravity gradiometry survey specifications followed 200 m flight lines and 2000 m tie lines at a minimum terrain clearance of 80 m. Deliverables included six tensor components (Txx, Txz, Tyy, Tyx, Tyz, Tzz) terrain corrected incrementally from 2.40 g/cm^3 to 3.00 g/cm^3. Only grids with a terrain correction of 2.70 g/cm^3 are used herein.

Results and Discussion

As the very first step in this routine involves applying several data transforms, one may ask which routines are best or most appropriate? In part this has been answered by Pilkington and Keating (2009) who comparing the results from 12 SED routines asked “are some enhancements redundant, useless, confusing?” Tilt (TI), vertical gradient (VG), balanced horizontal gradient magnitude (TDX) and theta (TH) are shown in their example to be redundant. Pseudogravity (PSG-hgm) and magnitude transform (MT) are also shown, in their example, to give comparable solutions. Inclusively, none are considered useless and only tilt horizontal gradient magnitude (THDR) is considered confusion. Thus the answer inevitably depends. In some respects it is limited by the data quality. Magnetic datasets in our example are of high quality having relatively low noise levels, thus of the four transforms chosen (TF-hgm, PSG-hgm, TH, and TI) all produced adequate solutions. If the data has a large amount of noise it would be advisable to not use routines which use higher order derivative or which employ an AGC filter since in these situations the ratio of signal to noise increases. In this study, TH and TI performed poorly when applied to the TDEM dataset and TI when applied to the gravity gradiometry dataset for this very reason. The type of data must also be considered. Using PGS-hgm would not be appropriate to either gravity or conductivity maps. In our example we found that TF-hgm was the most robust, albeit least sensitive method.

The sequence followed for edge stacking the magnetic datasets is displayed in Figure 5-4, and is identical for the EM and gradiometry products in Figure 5-5. Various image enhancement algorithms are applied to the dataset with corresponding transforms listed in Table 2. Once subsequent SED are solved for following image enhancement the edge solutions are combined into a single stacked display. In effect this increases the reliability of a true edge solution by combining the benefits and nuances for each routine. PSG – hgm and TF – hgm are less sensitive to subtle anomalies and noise than TH or TI which both detect deep and shallow sources or noise equally well. Therefore when combined, high amplitude anomalies are resolved with a greater confidence, implying more results along its edge and noise, which may

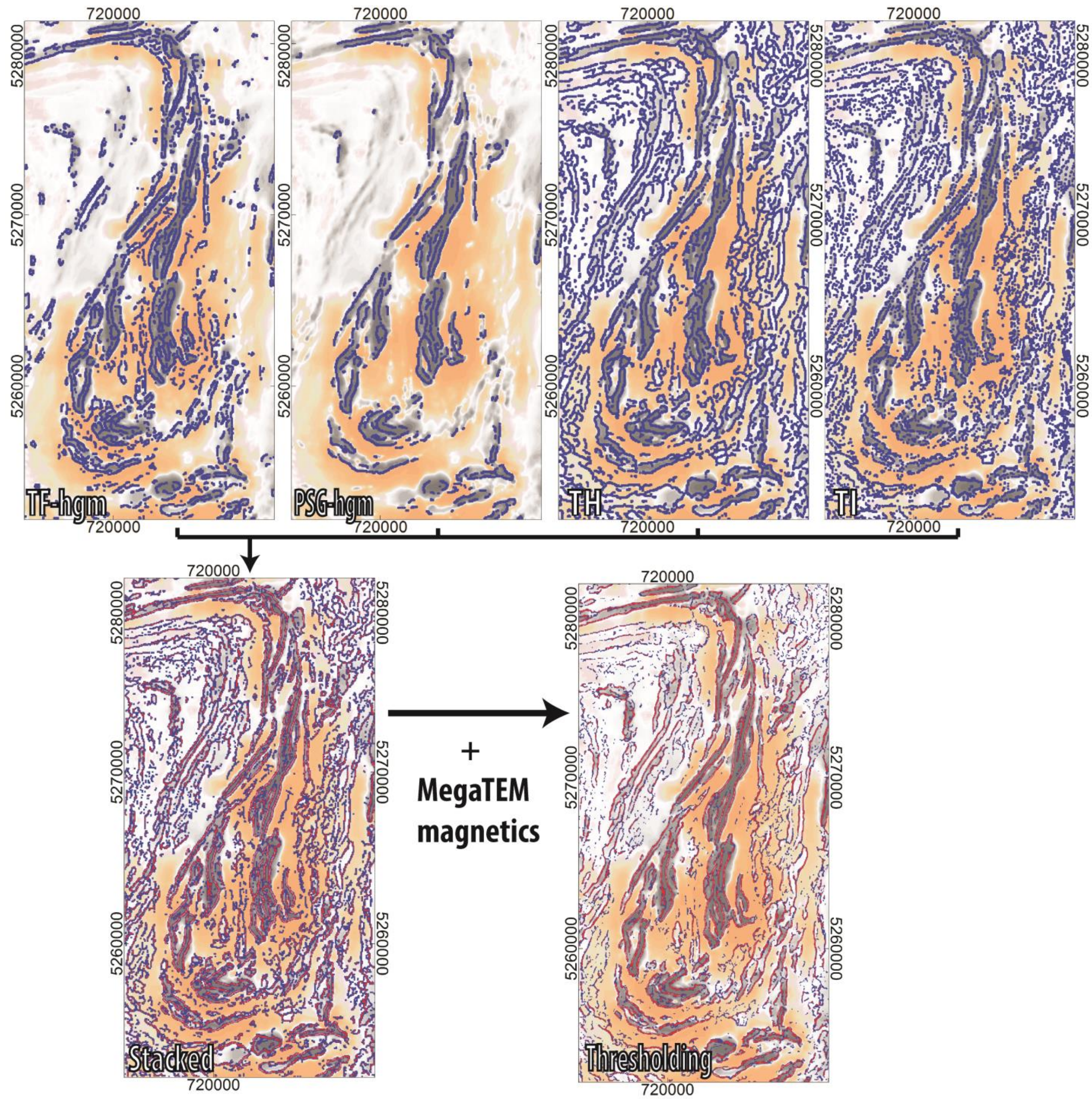

Figure 5-4: Sequence for edge stacking. A number of data transformation routines and subsequent edge detection is carried out on gridded geophysical data. These solutions are then combined into a single stacked solution. If additional data is available, i.e. another survey of the area, it may be brought in and both stacked solutions added. Finally, limiting the minimum value (amplitude threshold) remove spurious solutions leaving only locations were multiple edges have been detected. All SEDS are overlain on Aerodat residual magnetics.

Table 2: Image enhancement routines per dataset

Dataset	Transformation Algorithm
Residual Magnetics (Aerodat)	TF – hgm, PSG – hgm, TI, TH
Residual Magnetics (Megatem)	TF – hgm, PSG – hgm, TI, TH
Apparent conductivity (FDEM -32k Hz)	TF – hgm, TI, TH
Apparent conductivity (FDEM - 4433 Hz)	TF – hgm, TI, TH
Apparent conductance (TDEM)	TF – hgm
Gravity gradiometry	TF – hgm, TH

be picked up independently in any solution is reduced by rejecting values below a certain addition threshold.

Where additional surveys are available they may also be added together to further improve the reliability of SED solutions. Within this study area, two magnetic datasets are available and are combined in the final magnetic output (Fiure. 5-4). By combining the SED outputs from both magnetic datasets, false solutions from noise should be reduced since it is primarily a function of each individual survey. False solutions detected in the Aerodat survey may not necessarily correspond to false solutions recorded in the MegaTEM survey given the different recording instruments, flight characteristics and processing sequences. When values are removed below a certain threshold the interpretable product is improved by blanking these random solutions. Within our final output for Figure 5-4, a thresholding of 1 is applied removing all solutions below this point. As can be seen, this effectively cleans the stacked image by assuming that solutions found at a single point space are random noise and thus geologically non-significant.

When the stacked solutions are plotted on the geologic map there is excellent correlation between the three datasets and underlying geologic contacts (Fiure 5-5). As discussed previously, each geophysical method is recording a different physical property variation through the region. The magnetics is primarily mapping magnetically susceptible basaltic beds and mafic intrusions. All of the prominent magnetic anomalies are well resolved with many having a high number of solutions detected by SED. The subtle anomalies are also resolved though they tend to be less continuous around their source. In part this is caused by the thresholding which will likely be eliminating some true solutions, especially in the most subtle expressions where AGC is employed. An experienced interpreter can adequately infer continuity with edges overlain on a vertical derivative map, but it may also be that signal attenuation with depth is limiting the amplitude and thus it may not be appropriate to include these in a near surface geologic map.

Edges identified in the conductivity data are primarily defining the location of shale units through the study area. The Millstream Formation of the Fournier Group and Boucher Brook shale beds within the California Lake Group are well defined with a high number of overlapping solutions. There is little correlation between the geometry of source edge patterns and surficial Quaternary mapping (Parker and Doiron, 2003) suggesting the edges primarily represent bedrock response. Many of the low confidence solutions especially around the nose of the Tetagouche Antiform, are spotty and discontinuous in nature. These solutions are found mainly by transforms which normalize the field. Typically conductivity values range over several orders of magnitude, which if AGC is not applied, will carry through during the data transform.

Therefore in methods such as TF-hgm the edges of only the very large conductivity anomalies will be found, while TI and TH objectively solve for these subdued responses.

Data transformation and SED are poorest on the gravity gradiometry with only two routines (TF-hgm and TH) being successfully applied due to high frequency fluctuations in the original AGG data. As a result there is no thresholding (limiting of the minimum value) and all solutions are displayed in Figure 5-5. Because there is no thresholding and the data contains a high level of noise, there is the likelihood that false peaks are contained within the output and indeed a number of isolated SED solutions uncorrelated with the underlying geology are visible. The lack of many solutions also causes the gridded output to appear blocky and coarse relative to the magnetic and EM solutions. The solutions do however follow the general geologic trend quite well especially considering the data was acquired after the maps publication and the current processing routine which significantly improves the data quality (Mims et al., 2012) was not developed until 2010. Primarily mapped is the presence or absence of denser mafic rock volume. The thrust contact between California Lake felsic volcanics with California Lake mafic volcanics is well defined along the western hinge of the NMS. Along the eastern side, the Sormany-Millstream contact is partially resolved with the part of the Sormany hook also being resolved near the nose of the NMS. To the north-eastern edge of the image the solutions appear quite noisy. This area contains a number of small basaltic beds which are highly deformed and likely boudinaged. The area is also locally quite rugged, nearing the Tetagouche River valley, which if not properly corrected for will, as shown by Tschirhart (2013), introduce topographic artifacts into the tensor grids. It is possible that improved data quality and more data transforms will improve the SED stacking.

Though the overall trends match well with the presently accepted geology map, there are noticeable differences. In several locations only specific members of the basalt beds are magnetic. For example, within the Sormany Formation of the Fournier Group highly magnetic basaltic beds are in contact with non-magnetic beds. The aeromagnetic survey detects only the magnetic layer. Yet the geologic map of this area shows only one lithology while magnetically there appear to be multiple distinct units. This lithological detail, which is outlined by the SED mapping, has been detected in physical property measurements; bivariate analysis has revealed two distinct populations of basalt susceptibilities that may relate to tholeiitic versus calc-alkali magma series (Tschirhart, 2013). A similar effect has been documented for basalts within the California Lake Group; tholeiitic Canoe Landing Lake basalts lack magnetic response while transitional basalts of the Boucher Brook Formation are highly magnetic and are detectable through the SED. These observations raise an interesting question that a geophysical contact may not necessarily correspond to a geologic contact and vice versa. Our solutions for magnetics, conductivity, and gradiometry map the presence or absence of magnetic, conductive and dense lithologies which are linked to their mineralogical properties, but are not

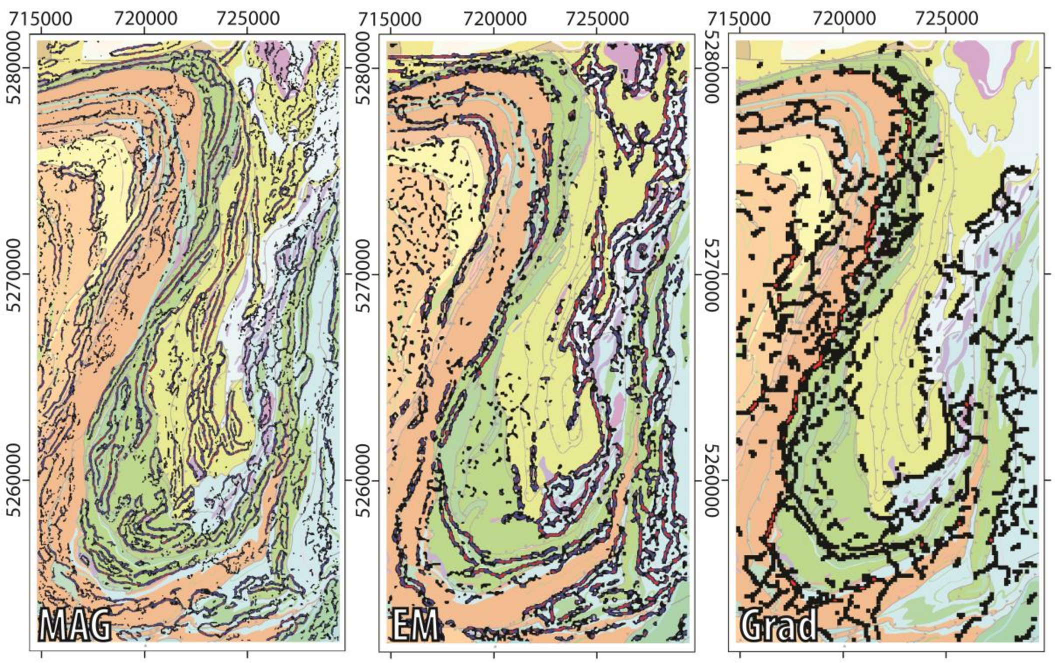

Figure 5-5: Results of edge stacking overlain on geology from Open File 3898 (van Staal et al., 2003). Mag = magnetics, EM = electromagnetics, Grad = gradiometry.

a direct indication of the geology. Using multi-parameter information, such as magnetic, electromagnetic and gravity gradiometry data collectively, however does improve the stratigraphic framework by outlining lithological features which have common physical property boundaries.

Fusion of the different datasets using a ternary display helps to highlight the relationship between all three parameters which unlike in the synthetic model are not directly related to the same single sources (Figure 5-6). The display uses a thresholding limit of 1 for magnetics (blue) and electromagnetics (red) while all gravity gradiometry (green) solutions are displayed. The histogram is linearly equalized and therefore brighter colours represent the summation of more SED solutions. A more complete geologic model may be developed using this display which, in our example shows contacts, fold, and truncations. For example, the gravity gradiometry SED coarsely outlines the NMS in conjunction with adjacent magnetic and conductive beds. Domains of primarily mafic magnetic beds within the Fournier Sormany Formation can be recognized to contact the overlaying Millstream Formation of primarily conductive sedimentary rock and show the complex, highly deformed relationship shared between the two. In the central to northeastern region of the map an interpretative thrust contact can be observed by predominately north-south magnetic beds contacting undulating conductive anomalies. Eventually, after combining and interpreting the different datasets all of these relationships would become apparent, however this ternary display allows for a rapid development and speculation of such relationship which may be tested further through more thorough analysis and modelling.

When working with potential field data a possible complication is introduced by the source depth, which we previously noted in the magnetic solutions. The observed signal of all potential field methods represents the summation of all underlying sources while a bedrock geology map represents the surficial distribution of lithologies. Therefore an effective regional-residual separation filter must be applied prior to applying SED algorithms. Failure to apply such a pre-processing step may result in buried source bodies being mapped as near surface sources. For this study regional-residual separation was performed using a non-linear filter with a cut-off wavelength of 800m. The 800m wavelength is derived from a study which compares regional-residual calculation from correlation between susceptibility information calculated from HFEM and non-linear filtered TMI (Tschirhart et al., 2013).

Unit continuity is also an issue. As mentioned previously, especially where an anomaly expression is subtle, the SED fails to effectively define the entire anomaly perimeter regardless of the algorithm used. After stacking and thresholding subtle expressions often appear spotty and discontinuous; any true geologic contact must be laterally continuous for some distance. The application of a spatial continuity (line tracing) filter may benefit this method by rejecting

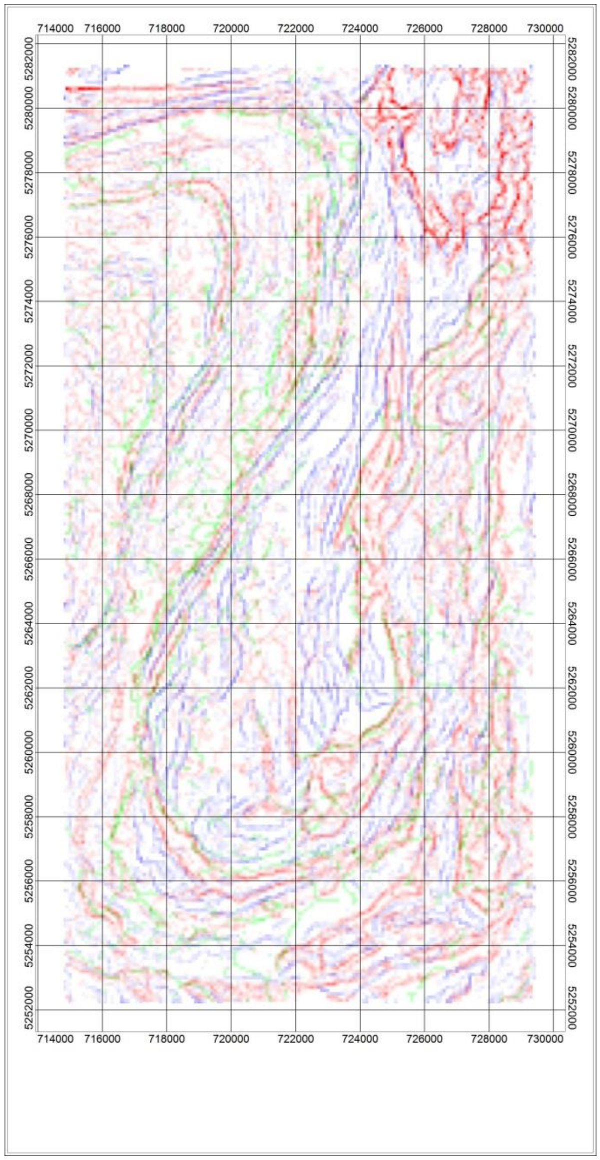

Figure 5-6: Ternary image combining the stacked edge solutions. Red = electromagnetics, green = gradiometry, blue = magnetics. Histogram is linearly equalized so brighter colours represent more solutions.

non-continuous sources. In our example the stacked magnetic solutions in the Tetagouche Antiform region appear to be spotty and discontinuous. Application of a minimum line length filter, or a morphological erosion filter would be able to reject the isolated point anomalies if their length or continuity does not meet a certain trend and distance requirement. Such a filter development is outside the scope of this project, but could be considered for future work.

Spatial resolution is a third issue that should be addressed and is reflected in terms of the lithological unit size being detected. With a coarse flightline spacing survey there is an obvious disadvantage to how detailed you can map. So-called high-resolution surveys used herein allow for a maximum spatial resolution 100 m in accordance with Nyquist sampling theorem. In complex environments, such as the BMC, the geology can change rapidly within a span of 100 m so a highly detailed geologic map is not possible given this dataset. The majority of magnetic beds in this area are relatively thin. As seen in the synthetic example, when a body is thin and of high susceptibility/ density, the SED solutions will often define it wider than it is in actuality. This is often the case within our stacked image where the basalt beds defined through SED are thicker than interpreted in the geologic map. Discussion on which is right however is circular since as evident in Figure 5-3 there is little outcrop to go by and the geologic map is based partially on the geophysical data.

Conclusion

Geophysical datasets are fundamental to any geologic mapping exercise. Source edge detection provides a means of quantitatively mapping contrasts within gridded geophysical datasets, but requires gradient inflections in the original datasets to be transformed into peaks. There are a number of ways in which to transform the data from classical techniques such as horizontal gradient of total field to modern methods such as the Theta map. Each algorithm is different and will produce a slightly different solution. Therefore it is always beneficial to compare the output of multiple routines. We have demonstrated the usefulness here of simple data stacking or adding solutions into a single output and applying direct gridding to the summation to help improve the final interpretable image. Stacking the transforms also allows thresholding, or limiting of the minimum value which as shown can be used to remove non-correlative signal; isolated single point solutions typical of noise. When multiple parameters are available, such as magnetics, gravity gradiometry and electromagnetics, they may be used and incorporated by means of a ternary display to further develop the stratigraphic framework by mapping different but complementary physical property variations in the local geology. A synthetic example using simple polyhedral and a real world example from the Bathurst Mining Camp, northern New Brunswick demonstrates the practicality of this methodology.

The results of our examples show that through stacking and direct gridding the resulting interpretation product can be improved. Actual edges indicative of geologic contacts are enhanced while random noise is removed through thresholding. Though generally successful caution must be used since an edge located within a geophysical dataset may not necessarily correspond to a geologic contact. Potential field methods also represent the summation of all underlying sources, which presents a depth issue when trying to isolation near surface source bodies. An improper regional / residual separation will result in deep contacts being miss interpreted as a near surface contact. As well, unit continuity may be an issue as subtle anomalies are generally resolved spotty and discontinuous. Finally, the resolution of the geophysical dataset will limit the resolution of the interpretable product. In highly complex geologic location, the resolution will be limited by the resolution of the geophysical survey.

References

Beamish, D., 2012. The application of spatial derivatives to non-potential field data interpretation. Geophysical Prospecting, **60**, 337-360.

Blakely, R. J., and Simpson, R. W., 1986. Approximating edges of source bodies from magnetic or gravity anomalies. Geophysics, **51**, 1494-1498.

Cascone, L., Campbell, S., Green, C., Salem, A., and Fairhead, D., 2012. ACLAS: A new automatic method of defining potential field lineaments using coherency analysis. SEG Technical Program Expanded Abstracts 2012: pp. 1-6. doi: 10.1190/segam2012-1254.1

Cooper, G. R. J., and Cowan, D. R., 2006. Enhancing potential field data using filters based on the local phase. Computers & Geosciences, **32**, 1585-1591.

Cordell, L., 1979. Gravimetric expression of graben faulting in Santa Fe County and the Espanola Basin, New Mexico. *In* Guidebook to Santa Fe County: 30th Field Conference. *Edited by* R. V. Ingersoll. New Mexico Geological Society, 59–64.

Cordell, L., and Grauch, V.J.S., 1985. Mapping basement magnetization zones from aeromagnetic data in the San Juan Basin New Mexico. *In* Utility of regional gravity and magnetic maps. *Edited by* W. J. Hinze. Society of Exploration Geophysicists, 181–197.

Keating, P. B., Kiss, F. G., Katsube, J., and Best, M. E., 1998. Airborne conductivity mapping of the Bathurst Mining Camp. Exploration Geophysics, **29**, 211-217.

Keating, P., and Pinet, N., 2011. Use of non-linear filtering for the regional–residual separation of potential field data: Journal of Applied Geophysics, **73**, 315 – 322.

Lam, L., Lee, SW., and Suen, C. Y., 1992. Thinning methodologies-a comprehensive survey. IEEE Transactions on pattern analysis and machine intelligence, **14**, 869-885.

Leblanc, G.E., Lee, M.D., and Morris, W.A., 2012. A simple adaptable fusion methodology for geophysical exploration. Exploration Geophysics, **43**, 190-197.

Miller, H. G., and Singh, V., 1994. Potential field tilt—a new concept for location of potential field sources. Journal of Applied Geophysics, **32**, 213-217.

Mims, J., Cuma, M., Wilson, G., Mataragio, J., Zhdanov, M.S., 2012. Recent advances in airborne gravity gradiometry: A case study from the Bathurst Mining Camp, In KEGS-DMEC Exploration ’07 plus 5: A half-decade of mineral exploration developments.

Parker, M.A., and Doiron A., 2003. Quaternary geology of the Bathurst Mining Camp and implications for base metal exploration using drift prospecting. *In* Massive Sulfide Deposits of the Bathurst Mining Camp, New Brunswick, and Northern Maine. *Edited by* W.D., Goodfellow, S.R., McCutcheon, and J.M., Peter. Economic Geology Monograph 11, pp. 631-660.

Pilkington, M., and Keating, P., 2004. Contact mapping from gridded magnetic data? a comparison of techniques. Exploration Geophysics, **35**, 306-311.

Pilkington, M., and Keating, P. B., 2009. The utility of potential field enhancements for remote predictive mapping. Canadian Journal of Remote Sensing, **35**, S1-S11.

Roest, W. R., Verhoef, J., & Pilkington, M., 1992. Magnetic interpretation using the 3-D analytic signal. Geophysics, **57**, 116-125.

Thomas, M.D., Walker, J.A., Keating, P., Shives, R., Kiss, F., and Goodfellow, W.D. 2000. Geophysical atlas of massive sulphide signatures, Bathurst mining camp, New Brunswick. Geological Survey of Canada, Open File 3887; and New Brunswick Department of Natural Resources and Energy; Minerals and Energy Division, Open File 2000-4, 105 pp.

Thomas, M.D. 2003. Gravity signatures of massive sulfide deposits, Bathurst Mining Camp, New Brunswick. *In* Massive Sulfide Deposits of the Bathurst Mining Camp, New Brunswick, and Northern Maine. *Edited by* W.D., Goodfellow, S.R., McCutcheon, and J.M., Peter. Economic Geology Monograph 11, 799-817.

Tschirhart, P., (2013) Geophysical processing and interpretation with geologic controls: examples from the Bathurst Mining Camp, New Brunswick. Unpublished M.Sc Thesis, McMaster University, Hamilton ON.

Tschirhart, P. A., Morris, W. A., and Jefferson, C. W., 2013. Geophysical modelling of the Neoarchean Woodburn Lake and Paleoproterozoic Ketyet River groups, and plutonic rocks in central Schultz Lake map area, Nunavut. Geologic Survey of Canada, Current Research no. 2013-2, 19 pp. doi: 10.4095/292116

van Staal, C.R., and Rogers, N., 1999. Northern half of the Bathurst Mining Camp, New Brunswick (pasts of NTS 21 O/7, 8, 9, 10; 21 P/5, 12). Geological Survey of Canada, Open File 3839, 8 colour maps, scale 1:20,000.

van Staal, C.R., Wilson, R.A., Rogers, N., Fyffe, L.R., Langton, J.P., McCutcheon, S.R., McNicoll, V., and Ravenhurst, C.E, 2003, Geologic and tectonic history of the Bathurst Supergroup, Bathurst Mining Camp, and its relationship to coeval rocks in Southwestern New Brunswick and adjacent Maine - A synthesis, *In* Massive Sulfide Deposits of the Bathurst Mining Camp, New Brunswick, and Northern Maine. *Edited by* W.D., Goodfellow, S.R., McCutcheon, and J.M., Peter. Economic Geology Monograph 11, 37-60.

Wijns, C., Perez, C., and Kowalczyk, P., 2005. Theta map: Edge detection in magnetic data. Geophysics, **70**, L39-L43.

Chapter Six: Conclusions

The primary objective of this thesis has been to develop new ways to process and interpret geophysical datasets. Any geophysical survey is a capital-intensive endeavor, but once a survey is complete the data is available from thereafter. New processing and interpreting procedures allow existing data to be rapidly re-examined and new insights gained. The abundance of modern, high-resolution, multi-parameter geophysical datasets and a well-developed geologic model has permitted the Bathurst Mining Camp, New Brunswick to being an excellent locale to develop and test these new techniques.

Chapter 1 presents an introduction to the primary goals of this thesis. A brief introduction to the Bathurst Mining Camp and its exploration history is also presented. Finally, the basic theory and processing techniques of the various geophysical data types used in this thesis is given.

Chapter 2 presents a statistical analysis of density and magnetic susceptibility samples collected through the camp. Descriptive statistics including mean, standard deviation, median 25th and 75th percentiles are performed on a variety of rock types. These statistics are supplied in tables and are useful for future geophysical modeling exercises in the Camp. Density- magnetic susceptibility bivariate plots are used to demonstrate the natural trends in the various lithologies and their relationship to depositional setting and metamorphism. Measurements on Felsic - Intermediate lithologies reveal broad overlap between their physical properties; as density increases so too does magnetic susceptibility. The relationship is independent of composition or bedding style. Sedimentary rocks yield two distinct population trends. We believe the trends are primarily governed by the degree of metamorphism which systematically reduces the magnetic susceptibility. Measurements on Iron formation samples plot as two clusters related to whether the sample is hematite or magnetite rich. Mafic volcanic samples also show two distinct clusters, a high magnetic susceptibility cluster and a low magnetic susceptibility cluster. Though the exact cause of this remains unknown we speculate it may be due to, compositional source differences, or bedding/ cooling rate differences. Finally the sulphides plot reflects a difference in bedding style. The massive samples and disseminated/ stringer are distinguishable on the basis of density. Magnetic susceptibility between all three types of sulphide concentrations are comparable though massive samples tend to typically have higher values. These plots and descriptive statistics are used to generate bivariate probabilistic representations of the various lithologies. This plot allows one to rapidly visualize the effectiveness of geophysical modeling and creates a realistic starting point to begin modeling. The petrophysical information is finally used to constrain two geophysical models within the Camp. A joint gravity-magnetic profile model is presented perpendicular to the hinge of the Nine Mile Synform. The structure across the NMS is primarily divided on the basis of near vertical nappes whose internal deformation is often independent of adjacent nappes. Globally all nappes are modeled to 5 km depths, though their total depth extent remains unknown. A constrained inversion of the magnetic anomaly associated with the Armstrong B deposit solved for a roughly south facing remanence vector inclined just below the horizon. The anomalies intensity is slightly stronger than the inducing field. By estimating the declination using the APWP we show the declination value closely matches what is expected if remanence were acquired during the metamorphism peak in the Salinic Orogeny (420 – 430 Ma). Though our inverted inclination value differs from our predicted, inclination is often inconsistently determined with inversion even when declination is accurate.

Chapter 3 of this thesis presents a method of forward modeling magnetic field anomalies using apparent susceptibility data derived from frequency domain electromagnetic data. The utility of this is demonstrated by selecting an optimum near surface magnetic residual from a suite of regional – residual separation techniques. Also, this method is capable of detecting remanently magnetized bodies and the polarity of the remanence by comparing the MS_{HFEM} to MS_{obs}. As a consequence of HFEM system design source detection is limited in depth to the first couple hundred meters from surface. This restricts magnetic bodies recovered through HFEM inversion to no deeper than approximately 200 m, effectively allowing for a depth constraint when compared to the observed magnetic field. In our example we choose an 800 m non-linear filter to be the most accurate residual magnetic anomaly map. The inverted MS_{HFEM} is independent of magnetic latitude and remanence, and therefore when modeled, the magnetic field is only the product of the inducing field. The standard apparent susceptibility filter assumes no remanence. A remanently magnetized body will either return a systematically higher or lower MS_{obs} depending on the direction of remanent magnetism. The MS_{HFEM} will calculate an approximate susceptibility regardless of remanence. By simply generating a cross plot of the two susceptibility estimates (MS_{obs} vs. MS_{HFEM}) it is possible to identify linear outlier trends. In our example we found a positive linear outlier trend which when plotted in map (plan) view outlines the region of a remanently magnetized body in the study area. The major limitation of this method is effects of conductivity. Where conductivity is dominant, susceptibility cannot be accurately determined. Furthermore, cultural artifacts that affect HFEM systems can be amplified in the inversion and subsequent forward modeling. Care must be taken so that these features are excluded from the geologic interpretation.

Chapter Four examines a variable density terrain model to correct ground gravity (GG) and airborne gravity gradiometry (AGG) datasets in the Bathurst Mining Camp. The spectral information recorded by both surveys is also compared for semblance. Density values from Chapter 2 are used to generate representative average densities for the various tectono-stratigraphic groups in the BMC. In the GG dataset these real world density values are applied to the Bouguer and terrain corrections, and solely to the terrain correction in the AGG dataset. In both cases isolated anomalies juxtaposing larger regional highs are better resolved. The higher correction value allows for a greater reduction in denser regions and a lower correction factor in the less dense regions, therefore isolated dense anomalies in a less dense package become more prominent. The effect of topography, particularly within the AGG dataset, is also reduced by applying the variable density correction. Terrain artifacts have shown to carry through where an inappropriate density correction is used; using real world density values representative of the underlying geology mitigates this. These values are also typically very close to the optimum terrain correction value that results in zero correlation between the signal and topography. Computing the first vertical derivative on the GG data and continuing both to the same observation levels allowed the two grid images to be compared. At wavelengths less than 6 km the AGG is systematically more sensitive to the higher frequency information; above this to 30 km where low a high pass filtering was applied, the spectral information content converges. Differences in the higher frequency spectral content can be primarily attributed to irregular sampling in the GG. The regularly sampled AGG allows for less gridding related error than the sporadically spaced GG. The practicality of this method is limited to mapping purposes; it would be inappropriate to use data corrected this way for geophysical modeling or inversion.

Chapter Five demonstrates a simple technique for improving the output of source edge detection results and allowing for multi-parameter information to be included into a single interpretable image. A number of data transformation methods are applied to gridded geophysical data and the solutions added together and then gridded. Thresholding below a certain point is then applied to the stacked solutions. In a synthetic model, stacking is able to image true edges better than any one method alone. Thresholding the stacked image effectively removes false solutions caused by noise and cleans the final product. When multicomponent data is combined the real edges may be further resolved and structural information, such as dip direction, deduced. In an example from the NMS, the method works well. Combining multi-component information allows for the detection and mapping of different source parameters and therefore a more complete geologic map is produced. The method combines the benefits and nuances of the various data transformation algorithms. It assumes that random solutions are the product of noise in the data and are independent between transformations. Often the resulting product is spotty and discontinuous. We advocate the development of a minimum line length filter or morphological erosion filter to compliment this technique.

Limitations

There will always be limitations on what can be extracted from the various geophysical datasets. These limitations may be fundamental to the geophysical method or be geologic in nature. They may be manifested in terms of instrument sensitivity or survey design. All of these limitations restrict what can and how well an area or target may be resolved.

Central to all geophysical methods is the simple requirement of contrast. Without a physical property contrast, adjacent or underlying geologic formations will not be imaged as separate entities. This is a fundamental limitation of all geophysical methods. Magnetic and gravity fields are non-unique and therefore may both be represented by an infinite series of possible solutions. This problem manifests itself in several ways. In terms of depth estimates or regional/ residual separations, short wavelengths may only be produced by near surface sources while long wavelengths may be produced irrespective of source depth. For geologic modeling purposes, an observed magnetic or gravity anomaly is non-unique and therefore may be modeled as something dissimilar to the true geologic solution. Magnetic remanence is another factor that must be considered though it is often ignored. The magnetic remanence vector will complement, (or diminish) the present inducing vector to produce the observed anomaly. Without knowing the proper vector orientation and Q-ratio, source body contacts or geometries may be incorrectly defined. Furthermore many magnetic filters and inversion routines operate under the assumption that no magnetic remanence is present, which if it is, the solutions will be wrong. Frequency domain electromagnetic data is fundamentally restricted in depth extent by the conductivity of the medium and frequency of the transmitting source. An interpreter must therefore be aware of the limited depth of penetration. The HFEM susceptibility inversion is also limited by the conductivity of the medium. In very conductive bodies the effect of susceptibility is negligible compared to that of conductivity regardless of frequency. The resulting susceptibility values after inversion of these bodies are meaningless.

Geologically, geophysical datasets are limited by two factors 1) the geophysical versus geological interpretation and 2) the accuracy of the geologic map/ model. A geophysical interpretation is not the same as a geologic interpretation. Magnetic, gravity, and conductivity maps are recording the spatial distribution of magnetic, dense and conductive units respectively, which are a function of the geology, but not a direct indication of it. For example, a basalt and gabbro formation may be expressed similarly in a magnetic or gravity dataset, but from a geologic standpoint they represent completely different lithologies formed under very different conditions. Thus, the geologic map/ model must be well developed in order to differentiate these geophysically identical units.

Instrument sensitivity may restrict the quality and resolution of the geophysical data. Older legacy ground gravity stations have an associated error several times higher than that of modern ground gravity simply because the uncertainty in determining proper elevation in a pre-GPS era was so much greater. Eotvos corrections applied to airborne gravity gradiometry data require highly accurate acceleration measurements of the measuring platform. Turbulence affecting these systems may be several times higher in amplitude than the geologic signal being investigated. These systematic errors will manifest as noise in the data. Noise effects all geophysical survey systems and must always be considered during interpretation.

Finally, survey design will limit the data resolution and ultimately what features can be resolved. All airborne datasets used herein were acquired with flight lines spaced 200 m apart. On a regional scale this is highly detailed, but at a deposit scale it is very coarse. With flight lines spaced this far apart, the majority of the deposits in the BMC were completely missed because a flight line did not pass directly overhead. Effectively this limits how detailed the geophysical interpretation can be.

Appendix A: Physical property logs measured at Madran, New Brunswick

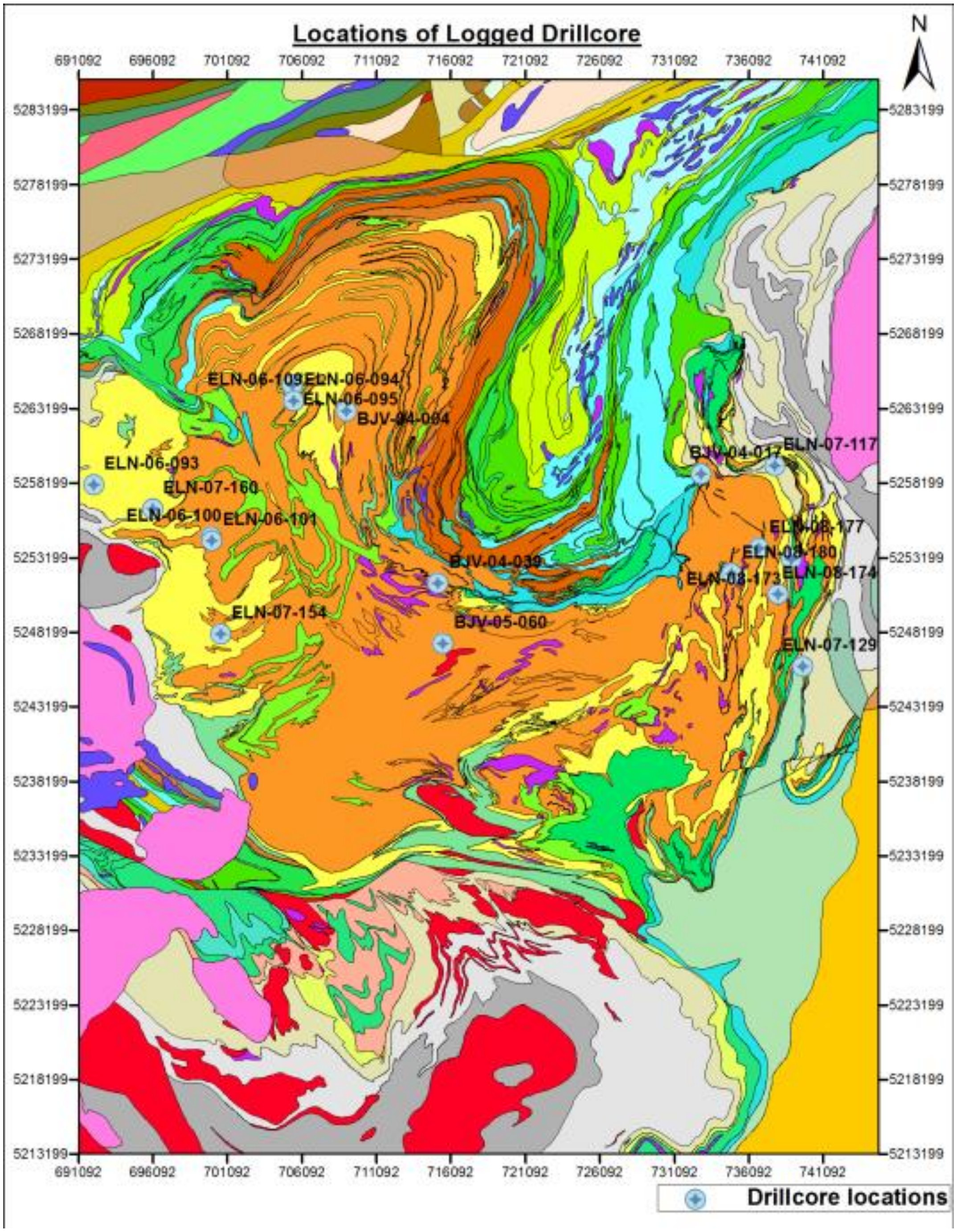

Figure A-1: Location of logged drillcore

Hole ID	Northing	Easting	Start (m)	End (m)	# of Samples	Comments
BJV-04-004	5263030	709060	6.8	223.5	45	Missing 147m - 194m
BJV-04-017	5258815	732888	8	362	11	Sporadic sampling
BJV-04-039	5251481	715219	3	274	60	Missing 247m - 272m
BJV-05-060	5247420	715560	10.6	531	96	Missing 207m – 285m
ELN-06-093	5258080	692121	15	129	27	
ELN-06-094	5263696	705527	15	160	35	
ELN-06-095	5264778	705446	3.5	164	44	
ELN-06-100	5254590	700001	85	394	21	Missing between 91m - 300m
ELN-06-101	5254338	700060	270	385	15	Missing between 313m - 330m, 334m - 385m
ELN-06-109	5263696	705527	35	135	5	Sporadic sampling
ELN-07-117	5259344	737873	9	946	155	
ELN-07-129	5245914	739715	164	167	3	Sporadic sampling
ELN-07-154	5248083	700656	9.5	334	77	
ELN-07-160	5256455	696090	142	157	6	Sporadic sampling
ELN-08-173	5253104	738977	8.5	753	145	
ELN-08-174	5250769	738076	233	241	4	Sporadic sampling
ELN-08-177	5253843	736788	6.5	548	120	
ELN-08-180	5252106	734936	707.5	1388.2	104	Missing between 708m - 907m
					N = 973	

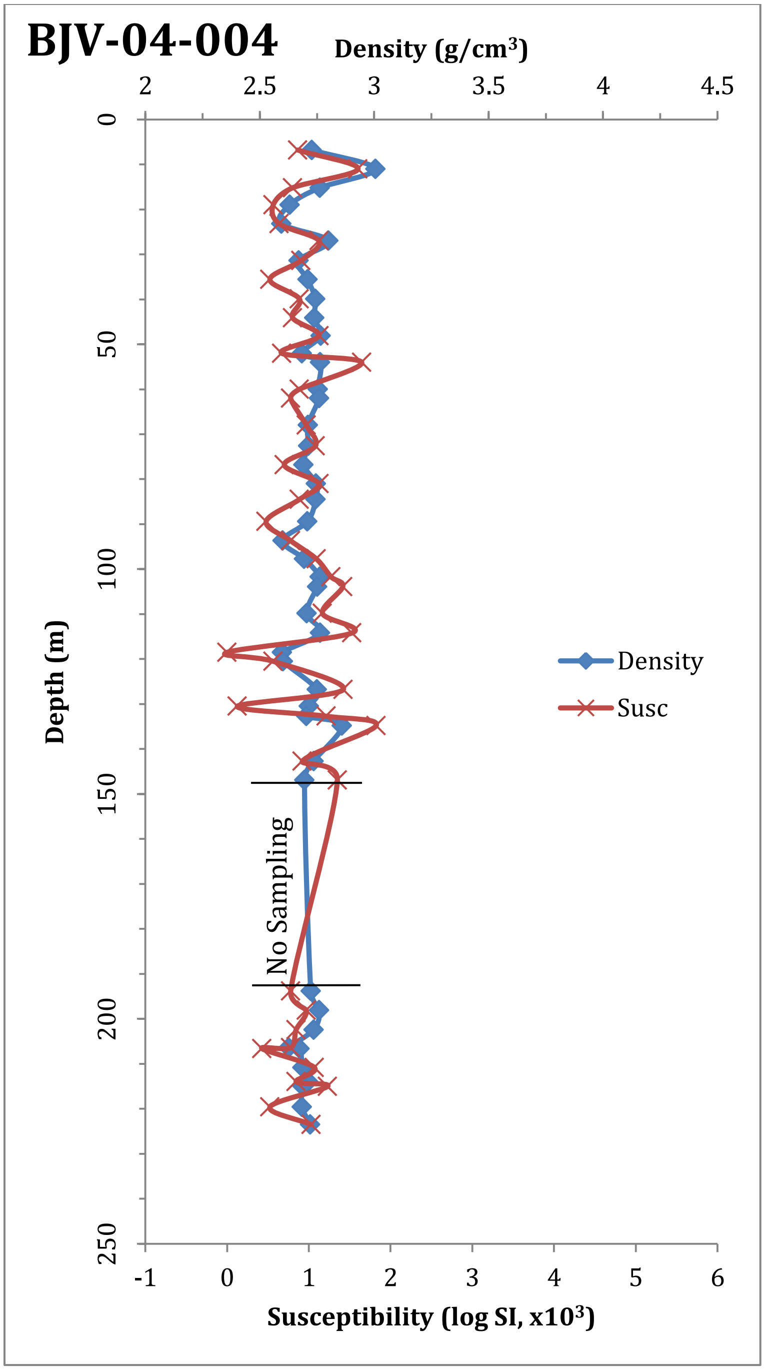
BJV-04-004
Density (g/cm³)
2
2.5
3
3.5
4
4.5
Depth (m)
0
50
100
150
200
250
No Sampling
Density
Susc
-1
0
1
2
3
4
5
6
Susceptibility (log SI, x10³)

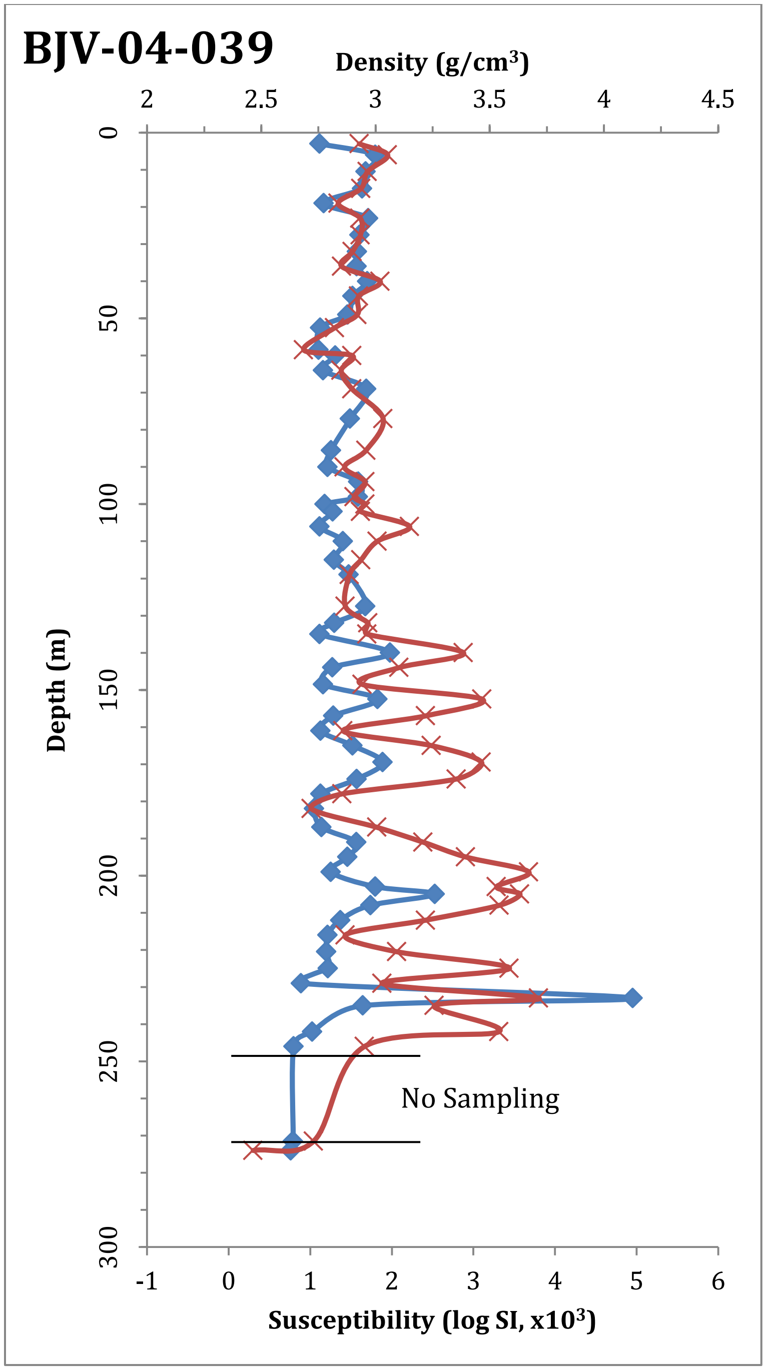
BJV-04-039
Density (g/cm³)
2
2.5
3
3.5
4
4.5
Depth (m)
0
50
100
150
200
250
300
No Sampling
-1
0
1
2
3
4
5
6
Susceptibility (log SI, x10³)

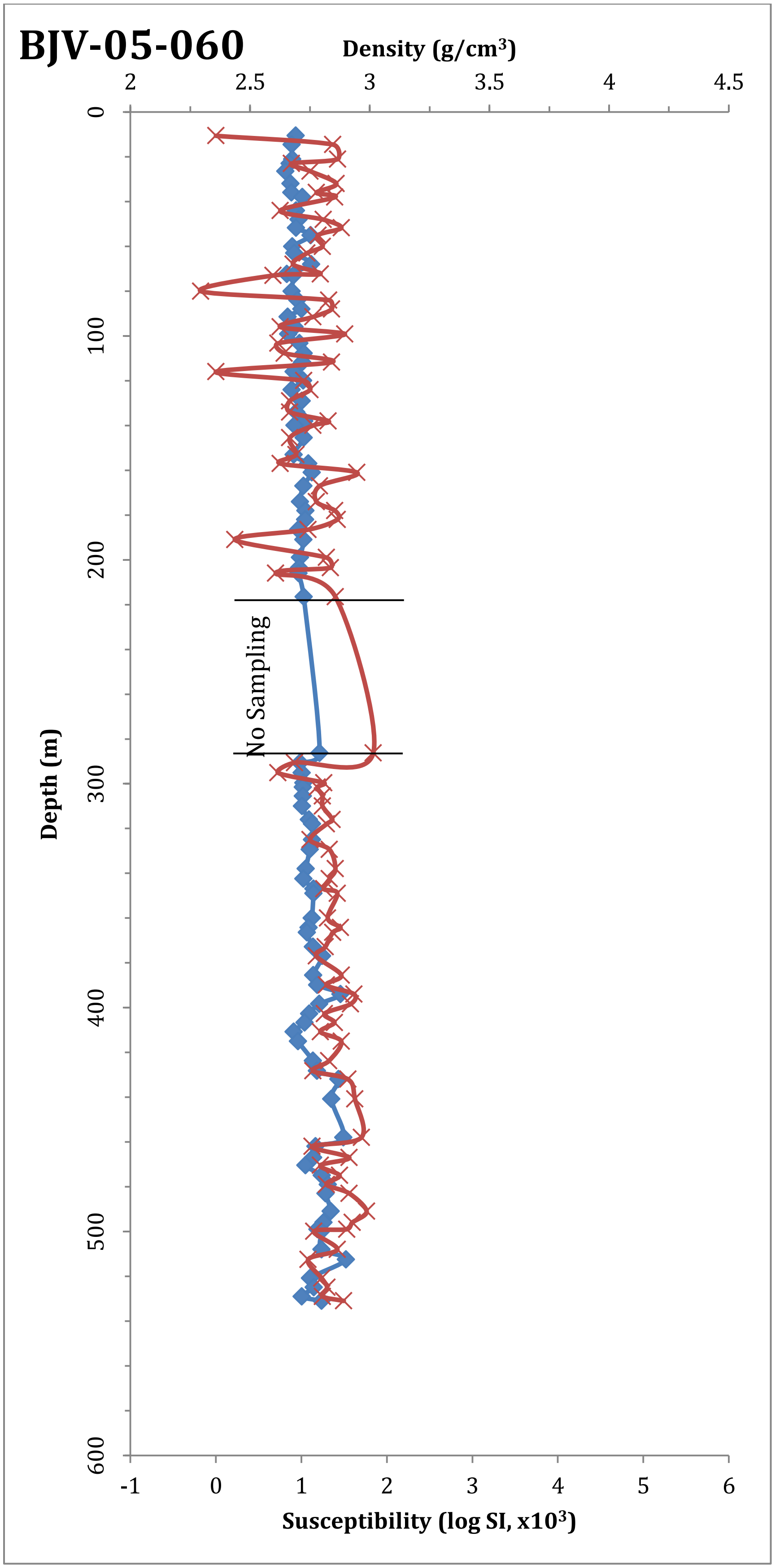
BJV-05-060
Density (g/cm³)
2
2.5
3
3.5
4
4.5
Depth (m)
0
100
200
300
400
500
600
No Sampling
-1
0
1
2
3
4
5
6
Susceptibility (log SI, x10³)

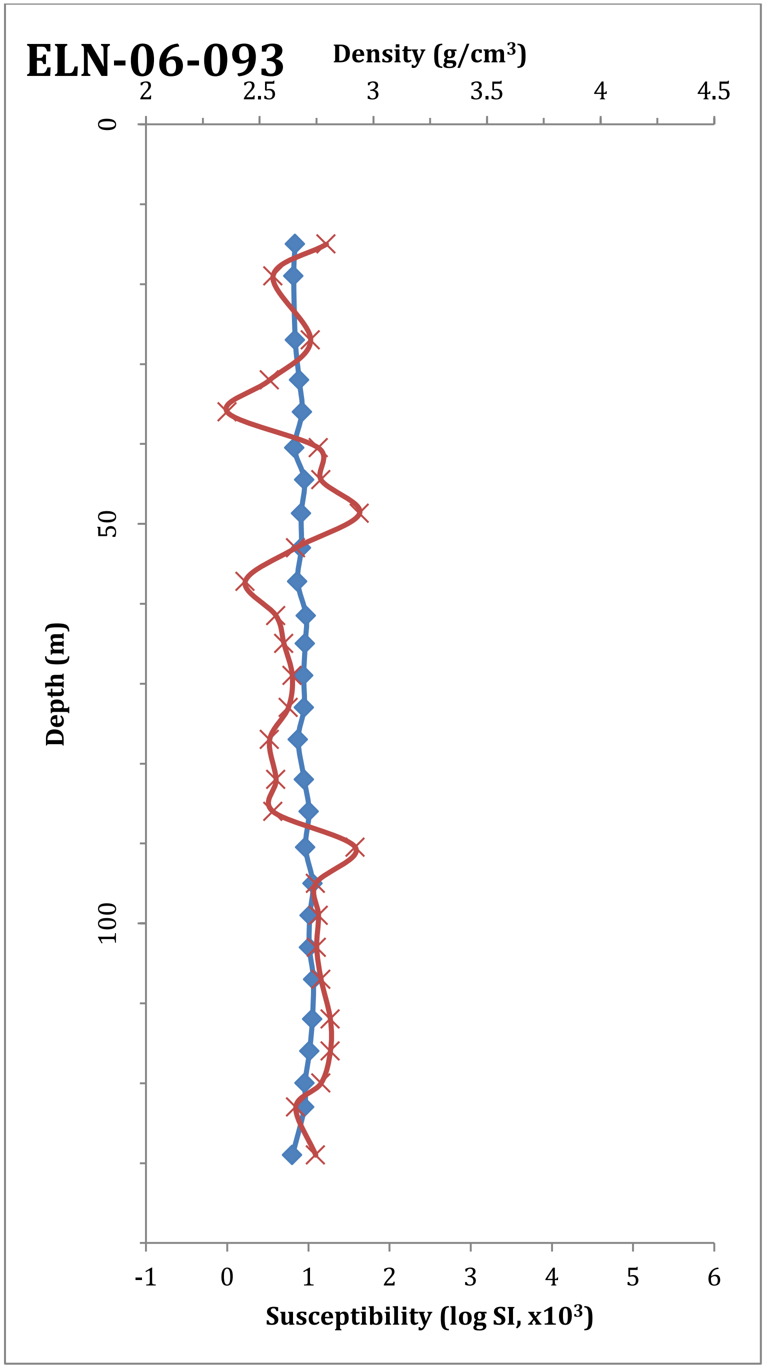
ELN-06-093
Density (g/cm³)
2
2.5
3
3.5
4
4.5
0
50
100
Depth (m)
-1
0
1
2
3
4
5
6
Susceptibility (log SI, x10³)

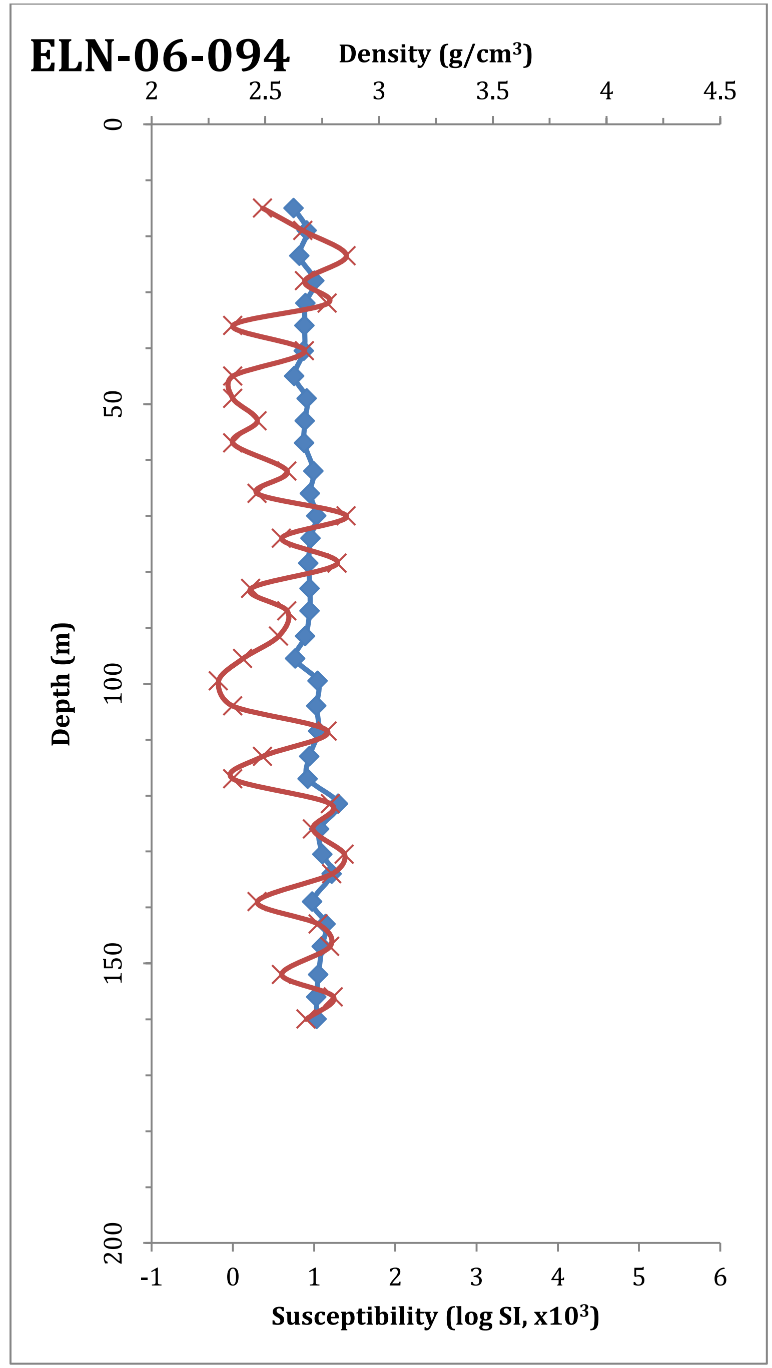
ELN-06-094
Density (g/cm³)
2
2.5
3
3.5
4
4.5
0
50
100
150
200
Depth (m)
-1
0
1
2
3
4
5
6
Susceptibility (log SI, x10³)

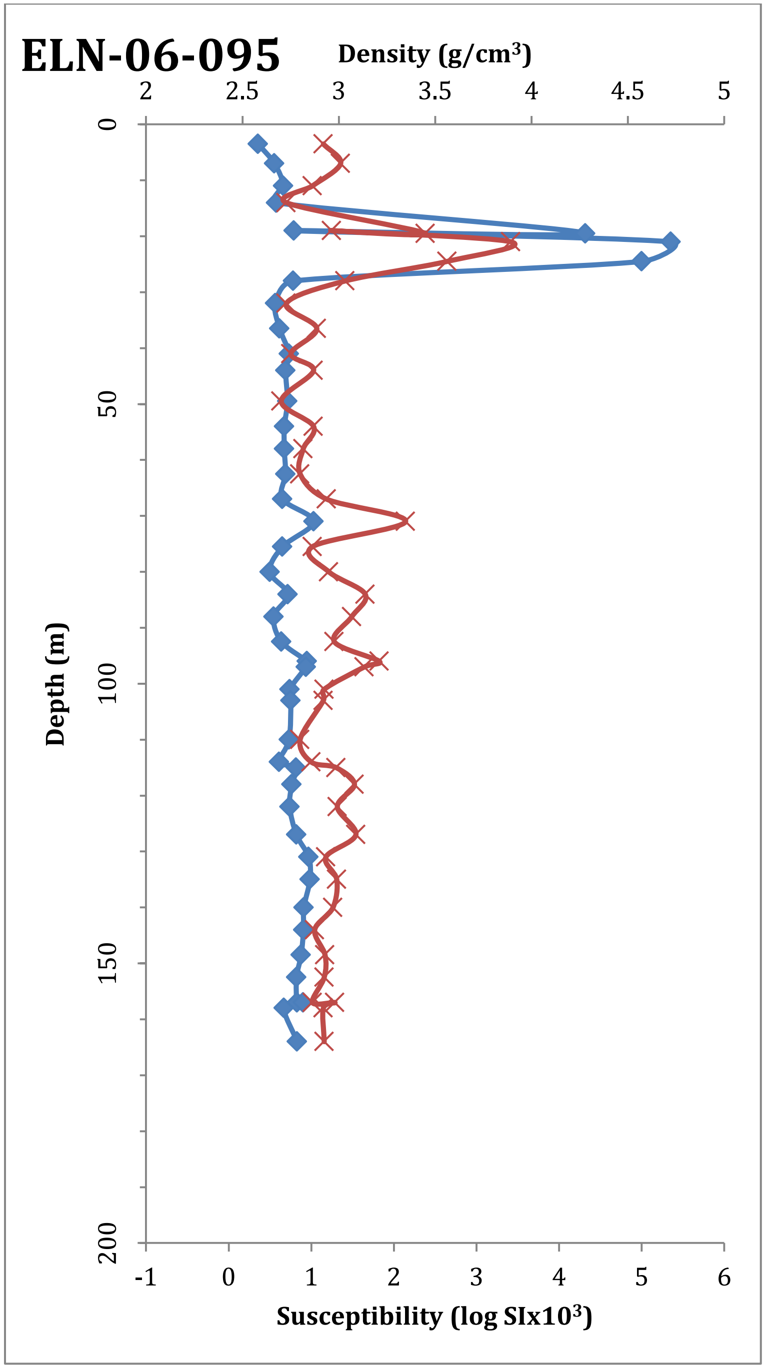
ELN-06-095
Density (g/cm³)
2
2.5
3
3.5
4
4.5
5
Depth (m)
0
50
100
150
200
-1
0
1
2
3
4
5
6
Susceptibility (log SIx10³)

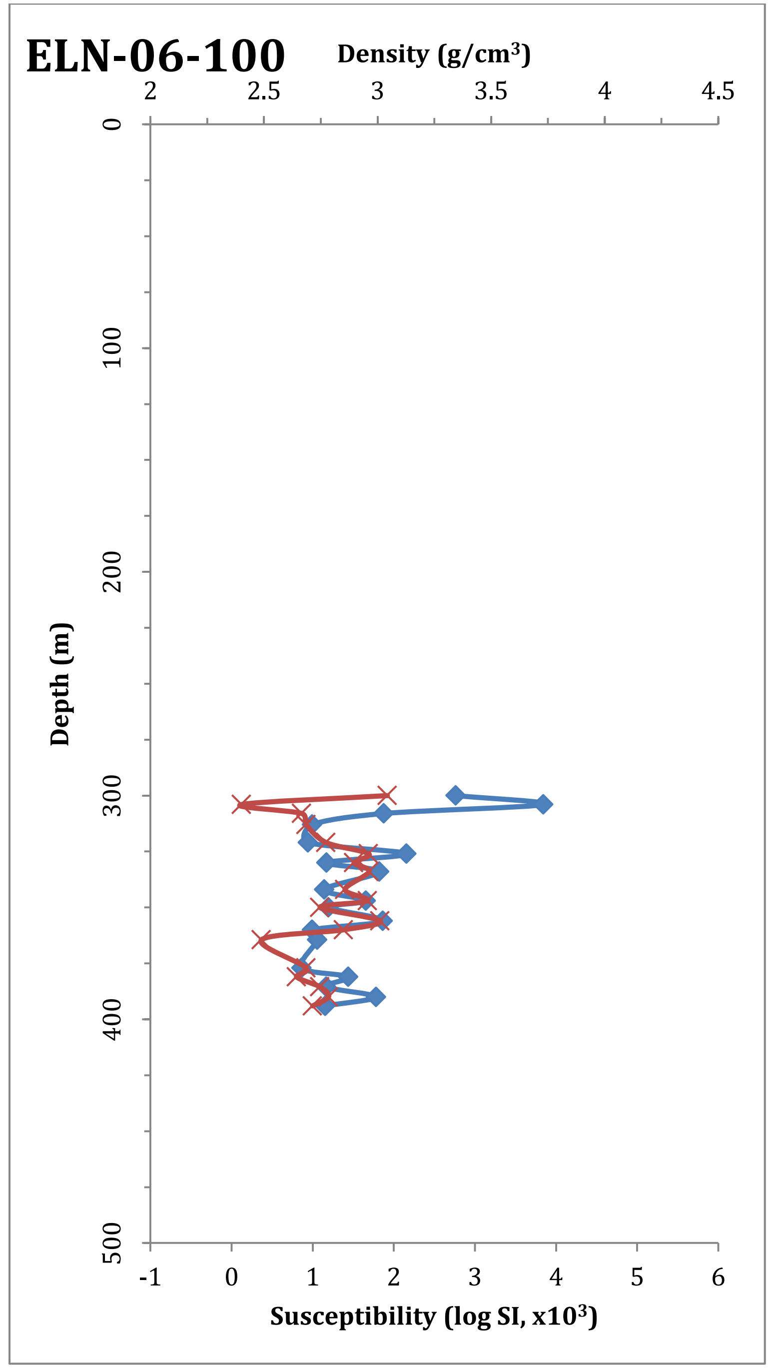
ELN-06-100
Density (g/cm³)
2
2.5
3
3.5
4
4.5
Depth (m)
0
100
200
300
400
500
-1
0
1
2
3
4
5
6
Susceptibility (log SI, x10³)

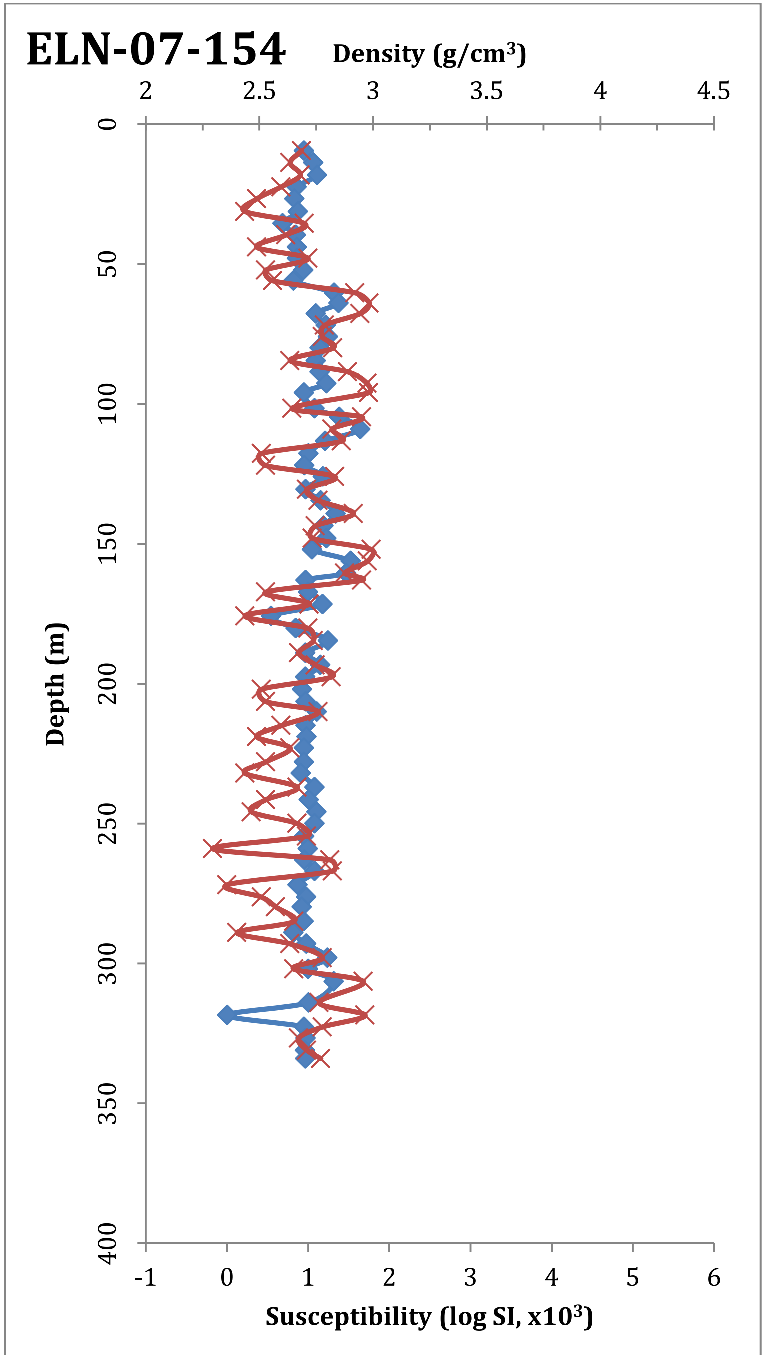

ELN-07-154
Density (g/cm³)
2
2.5
3
3.5
4
4.5
Depth (m)
0
50
100
150
200
250
300
350
400
-1
0
1
2
3
4
5
6
Susceptibility (log SI, x10³)

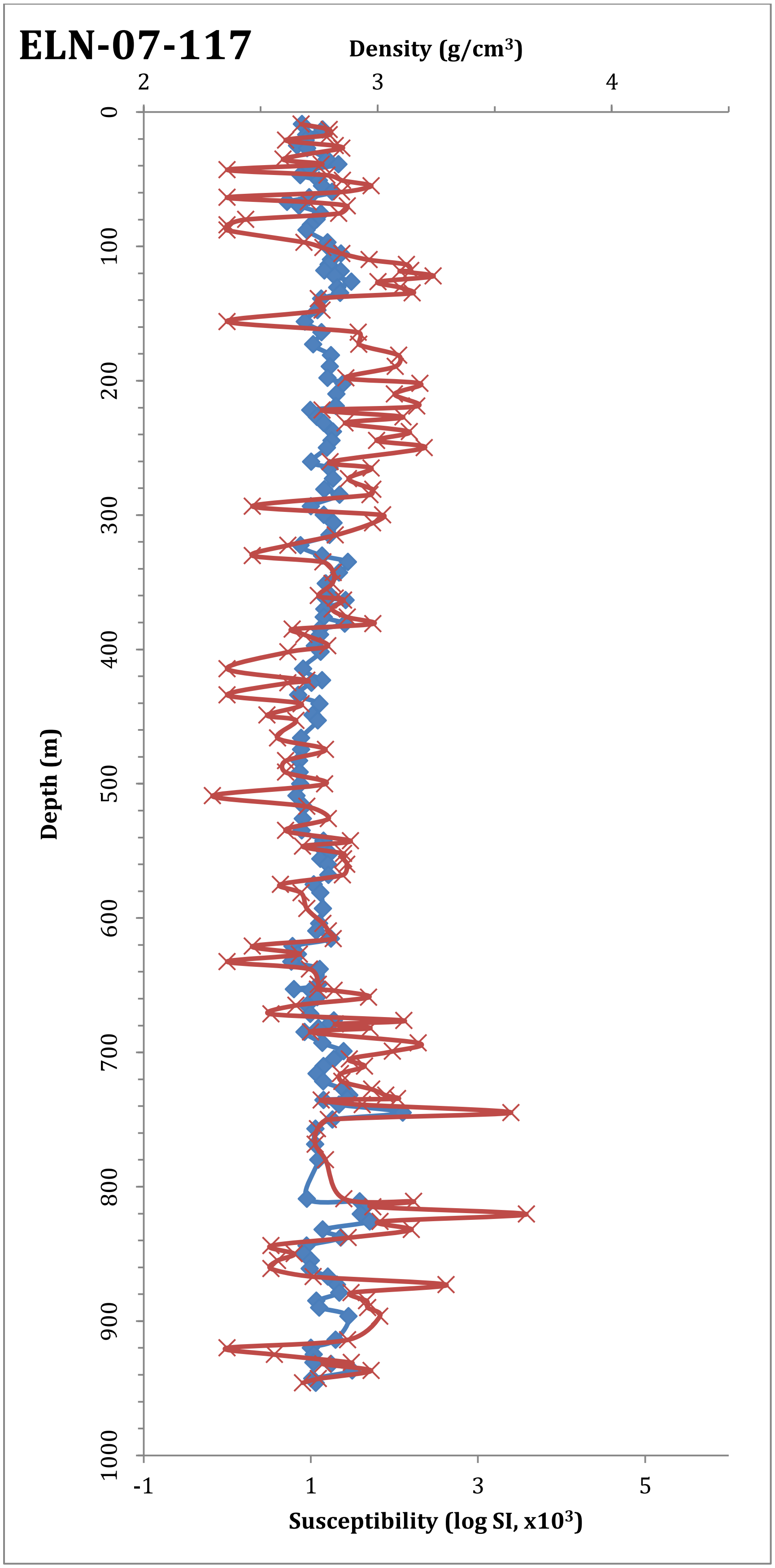
ELN-07-117
Density (g/cm³)
2
3
4
0
100
200
300
400
500
600
700
800
900
1000
Depth (m)
-1
1
3
5
Susceptibility (log SI, x10³)

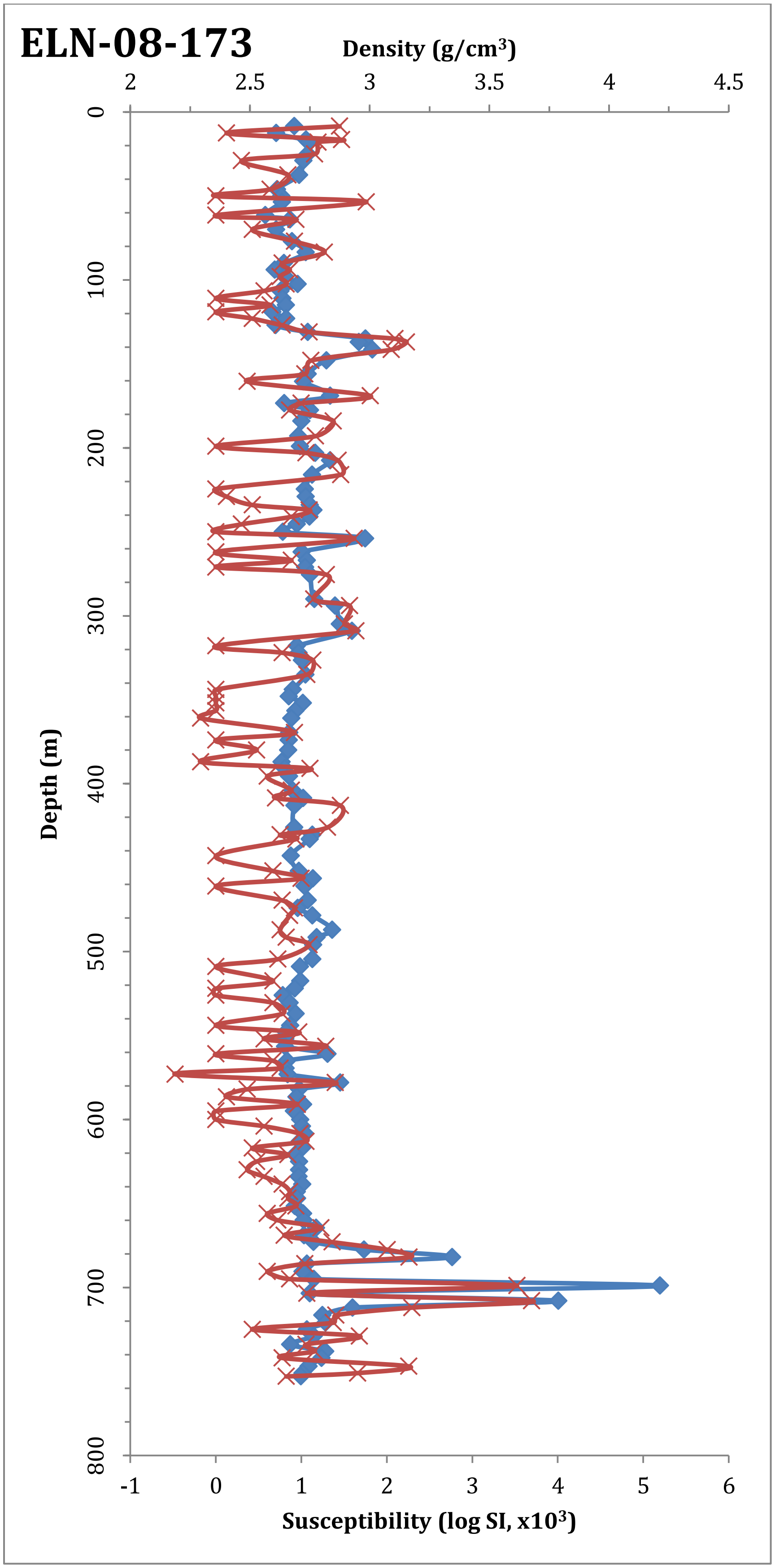
ELN-08-173
Density (g/cm3)
2
2.5
3
3.5
4
4.5
Depth (m)
0
100
200
300
400
500
600
700
800
-1
0
1
2
3
4
5
6
Susceptibility (log SI, x103)

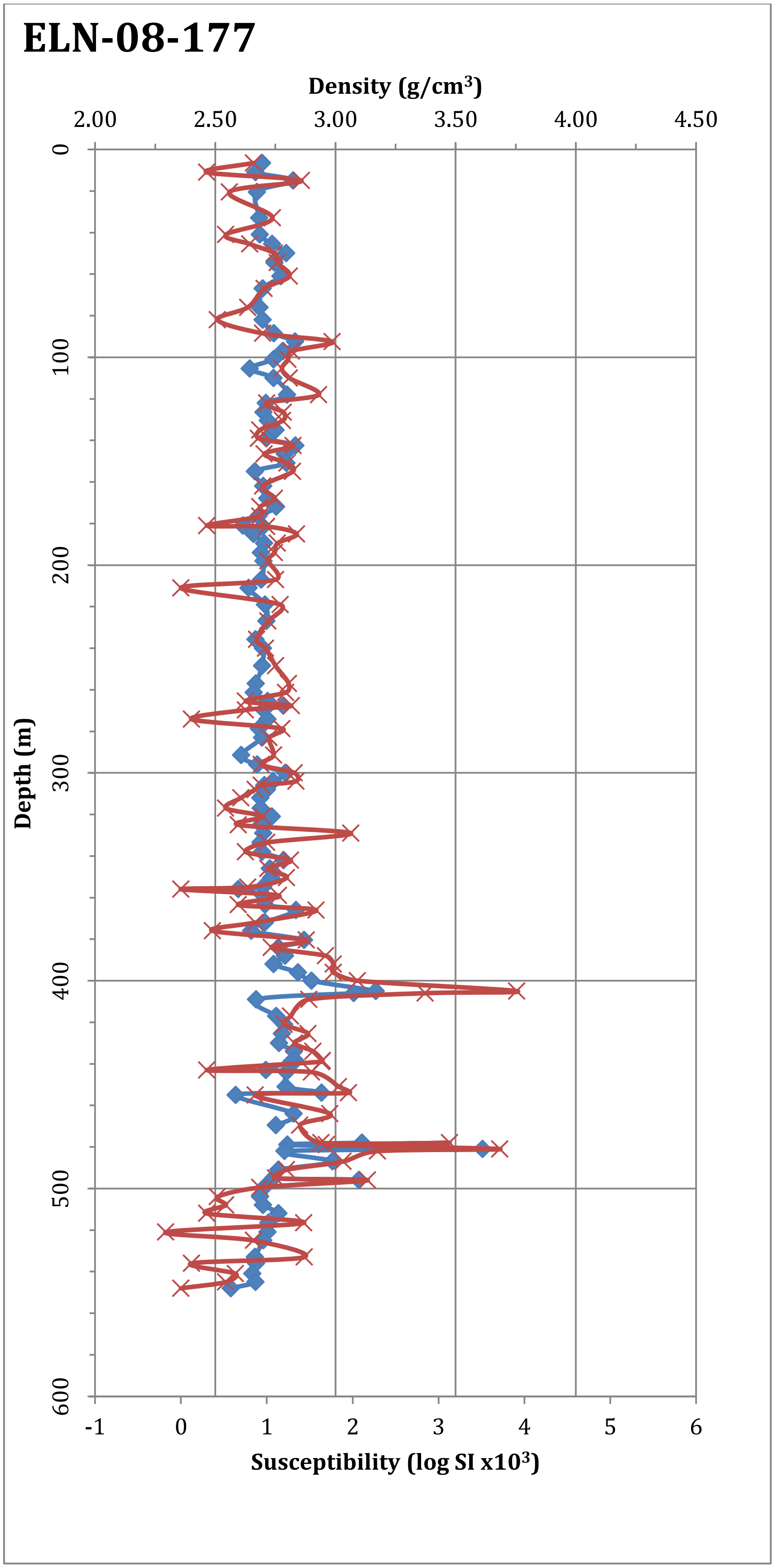
ELN-08-177
Density (g/cm^3)
2.00
2.50
3.00
3.50
4.00
4.50
Depth (m)
0
100
200
300
400
500
600
-1
0
1
2
3
4
5
6
Susceptibility (log SI x10^3)

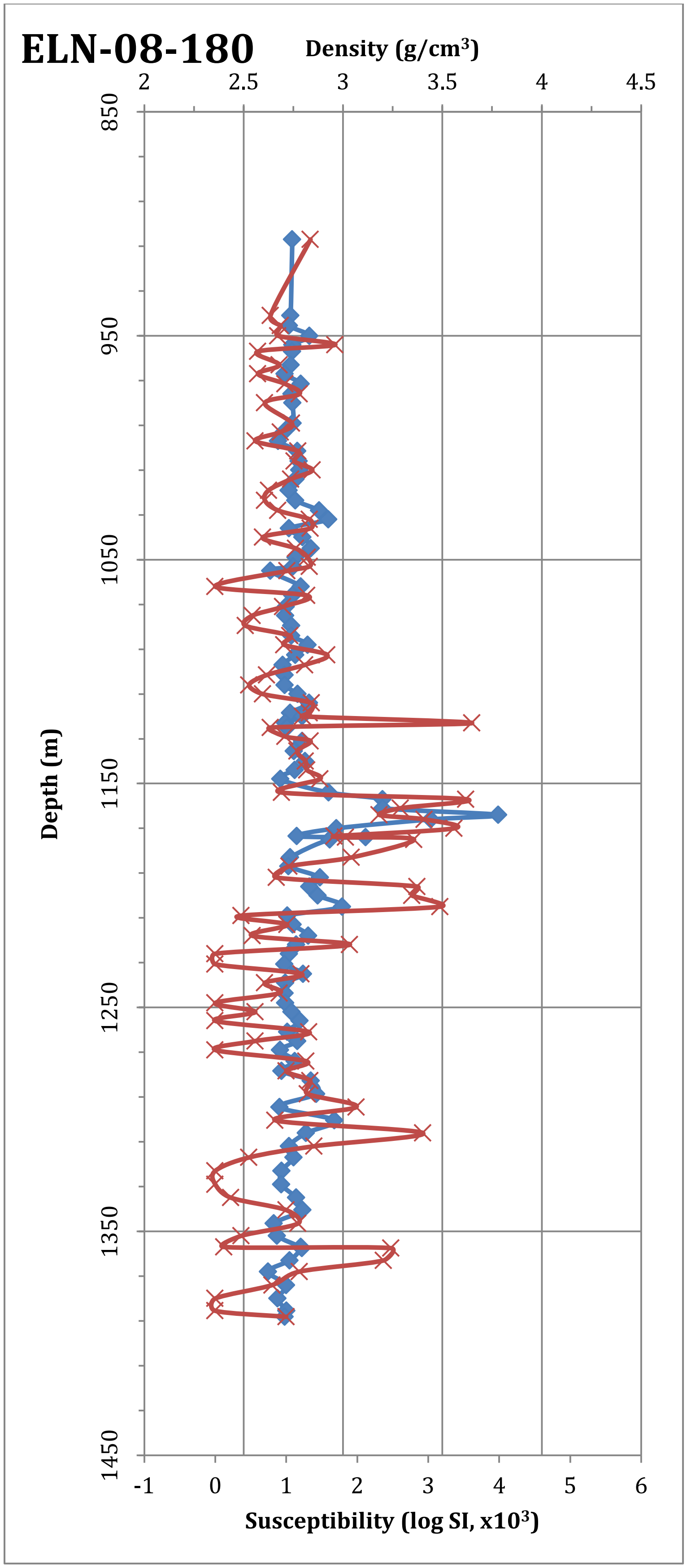
ELN-08-180
Density (g/cm^3)
2
2.5
3
3.5
4
4.5
850
950
1050
1150
1250
1350
1450
Depth (m)
-1
0
1
2
3
4
5
6
Susceptibility (log SI, x10^3)

APPENDIX B: List of Included Digital Files

All grids are projected using NAD83 UTM19N. Projection information is stored in the accompanying .grd.gi file of the same name.

C_Boug_270.grd	Complete Bouguer anomaly corrected at 2.70 g/cm^3.
C_Boug_var.grd	Complete Bouguer anomaly corrected using a variable density model.
Tzz_TCvar.grd	FTG Tzz component processed with a variable density terrain correction.
Txx_TCvar.grd	FTG Txx component processed with a variable density terrain correction.
Txy_TCvar.grd	FTG Txy component processed with a variable density terrain correction.
Txz_TCvar.grd	FTG Txz component processed with a variable density terrain correction.
Tyy_TCvar.grd	FTG Tyy component processed with a variable density terrain correction.
Tyz_TCvar.grd	FTG Tyz component processed with a variable density terrain correction.
TCvar_MinCur.grd	Variable density terrain correction model. Produced using a minimum curvature gridding algorithm.
HFEMsusc.grd	HFEM inverted magnetic susceptibility of the entire survey area stitched together from individual survey blocks.
HFEMsusc_BlockA.grd	HFEM inverted magnetic susceptibility for survey block A.
HFEMsusc_BlockB.grd	HFEM inverted magnetic susceptibility for survey block B.
HFEMsusc_BlockC.grd	HFEM inverted magnetic susceptibility for survey block C.
HFEMsusc_BlockD.grd	HFEM inverted magnetic susceptibility for survey block D.

HFEMmag.grd	Forward modeled magnetic field for the test area in Chapter 3.